Mathematical Modeling of the Bacterial Flagellar Motor System

Fan Bai

A thesis submitted in partial fulfillment of
the requirements for the degree of
Doctor of Philosophy at the University of Oxford

Wolfson College
University of Oxford
Trinity Term 2008

Mathematical Modeling of the Bacterial Flagellar Motor System

Fan Bai, Wolfson College.

Thesis submitted for the degree of Doctor of Philosophy
at the University of Oxford, Trinity Term 2008.

Abstract

This thesis describes the mathematical modeling of the Bacterial Flagellar Motor (BFM) system, for both the torque-generation and switching mechanisms. For the torque generation mechanism, a two-state Markov-Fokker-Planck model (also known as the Langevin dynamics formalism) was constructed. The model successfully explains the torque-speed relationship and stepping behaviour of the BFM. The model is not sensitive to the structural details of the BFM or model parameter variation. Thus, it can be used as a framework for future study of the BFM, when new experimental inputs become available.

On the switching mechanism, the Ising Allosteric model was reviewed and modified to fit the BFM system. A series of experiments were designed and performed to test the model and the results are consistent with the model's predictions. This work has established that the Ising model from condensed matter physics can also be applied to a complex multiprotein as an amplification mechanism.

The final chapter of the thesis investigates the free diffusion of fluorescently labelled stator complexes on the cell membrane and their exchange with functioning stators in the BFM with a simple diffusion-capture model.

The contents of this thesis represent a good example of intimate collaboration between theory and experiments: mathematical modeling helps us understand and direct future experiments; while experiments provide the foundations for accurate modeling.

ACKNOWLEDGEMENTS

There are many people I need to thank for making this thesis possible.

First of all, I am grateful to my supervisor Dr. Richard Berry for his guidance in all aspects of my study. His passion in scientific research is a good example for us all.

Special thanks to Prof. George Oster, Dr. Jianhua Xing. I have learned a lot from them during my stay in UC Berkeley.

This thesis could not have been completed without stimulating discussions with my colleagues, so I must thank:

Dr. Chien-Jung Lo for his invaluable comments on my research and countless help in my experiments.

Dr. Teuta Pilizota for building the cutting edge optical trapping system; without her outstanding work we could not have resolved the detail of BFM switching.

Richard Branch for helping me with the experiments and all kinds of support in the switching project.

Dr. Mark Leake for showing me a high standard of scientific writing; I am honoured to contribute to his work.

Dr. Yoshiyuki Sowa, Dr. Stuart Reid, and Dr. Tania Saxal.

I wish to express my gratitude to those who have supported me financially: the Clarendon Scholarship of the University of Oxford, the China Oxford Scholarship Fund, the NANOMOT research grant and the Wellcome Trust VIP awards.

Finally, special thanks to all my friends in Oxford.

Table of Contents

CHAPTER 1

Introduction to the Study of Molecular Motors

1.1 THE MOLECULAR MOTOR FAMILY

1.1.1 A General Introduction

Molecular motors are proteins which can perform mechanical work by consuming 'fuel'- the free energy of nucleotide hydrolysis or ion gradients. They are machines made by nature that take part in almost every important biological process, including DNA transcription, replication, cell division, muscle contraction, bacterial motility and ATP synthesis. At the moment, they are far superior to the machines made by humans at this scale. These machines share some common features with macroscopic manufactured machines, such as the use of repeating cycles and similar velocity-load output relationships. However, there are also significant differences. First, these motors are of nano-scale size and live in a wet environment (molecules, subcellular organelles, and cells are all immersed in an aqueous environment). At this length scale, the motion of protein motors is dominated by thermal fluctuations as the surrounding water molecules never stop buffeting the motors [1]. While Brownian motion blurs motor trajectories, it also provides driving force that allows molecules to pass over high energy barriers which is usually forbidden in the macroscopic world

[2]. Another distinct feature of this environment is described as 'the world of low Reynolds number'. When small things move through fluids slowly, viscous forces are important but inertial forces are not [2]. These small objects will stop immediately after the applied force/ torque is withdrawn. It is this unique living environment that gives molecular motors remarkable power. However, it also brings great challenges. Only by combining cutting edge single-molecule imaging, manipulation techniques with complicated stochastic simulation algorithms can we shed light on the fundamental working mechanism of molecular motors.

The molecular motors family mainly falls into two categories: linear motors, which run in a preferred direction on linear tracks, such as DNA strains and actin filament; and rotary motors, which rotate around a central axis, generating a torque. The main research target in my thesis is the bacterial flagellar motor, a member of the rotary motor family. Here I provide a brief review of other molecular motors, for a comparison of the similarities and differences.

1.1.2 Linear Motors

Myosin

Myosins are a large superfamily of motor proteins that move along actin filaments by using the energy released from ATP hydrolysis [3]. Most of the family members are non-processive. One such example is myosin II, which is abundant in muscle tissues and responsible for muscle contraction. The myosin motor is a dimer with two identical heads that act independently. Each myosin head contains a catalytic site and an actin binding site. A coiled-coil rod links the two heads together and attaches them to the thick filament. Each motor is composed of two heavy chains and four light chains. The two heavy chains form the head domain. Each heavy chain

begins with a globular head at the N-terminal and ends with an alpha-helix at the C-terminal [4-6]. Motor domains of most myosins move non-processively along actin filaments toward the plus ends of the filaments. A few exceptions (eg. myosin V and myosin VI) move processively on actin filaments [7] (with myosin VI moving towards the minus end of the actin filament [8]).

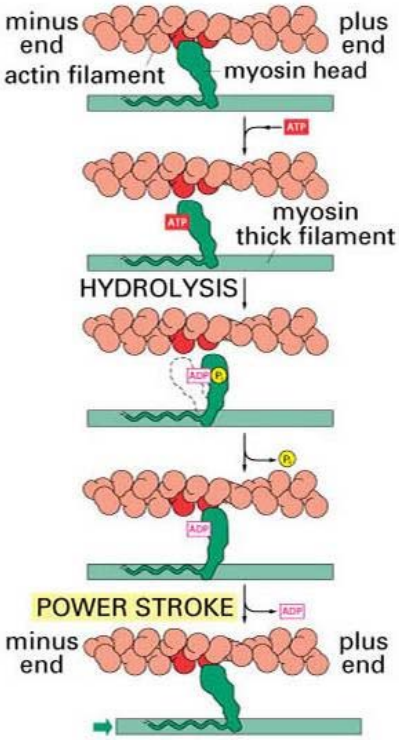

Figure 1.1.1 Schematic plot shows how muscle myosin works. Muscle contraction is caused by the sliding between actin and myosin filaments. After each power stroke, muscle myosin detaches from the filament. (adapted from reference[9]).

Extensive research has revealed the working mechanism of myosin motors [10-13]. At the beginning of a motor cycle, the myosin head containing bound ADP and phosphate has medium affinity to the actin filament. Once it attaches properly to the actin filament, phosphate is released. This tightens the binding of the myosin head to actin and also triggers the power stroke that pushes the actin filament. At the end of the power stroke, ADP is dissociated and a new ATP molecule binds to the catalytic binding site, causing the myosin head to be detached from the actin filament.

Subsequent hydrolysis of the ATP molecule resets the motor head to its pre- stroke position and thus completes a motor cycle. The sliding movement between myosin and actin filament triggered by ATP hydrolyzing in the head domain leads to fast and powerful muscle contraction when a large number of such motors work together.

Kinesin & Dynein

Kinesin is an important member of the superfamily of microtubule-based motors that perform force-generating tasks such as organelle transport and chromosome segregation [14]. Similar to myosin in structure, the kinesin motor is also a dimer with two identical motor heads. Each head consists of a catalytic site and a neck linker. In a cell, the major function of kinesin motors is to transport organelles along microtubules. Therefore, kinesin moves processively along a microtubule while the organelle is attached to the tail domain of the motor. Extensive research work has focused on the stepping behaviour of the motor [15-16] and its response to external load [17]. The working mechanism of kinesin motor is now well understood. At the beginning of the motor cycle, both kinesin heads contains bound ADP and move randomly in solution driven by Brownian motion. When one of the heads encounters a microtubule, it binds tightly. Microtubule binding causes the ADP to be released from the attached head and ATP rapidly enters the empty binding site on the head. This exchange triggers the ‘power stroke’, which throws the second head forward and brings it to the next binding site on the microtubule. During this action, the first head hydrolyzes the ATP and releases phosphate. Then the second head, which is now ahead, exchanges its bound ADP for an ATP from the solution and triggers the second ‘power stroke’. The first head is thrown forward to the next binding site, finishing the

cycle and resetting the system. As the motor repeats the cycle, the kinesin motor moves processively on the microtubule by a 'hand-over-hand' mechanism [18].

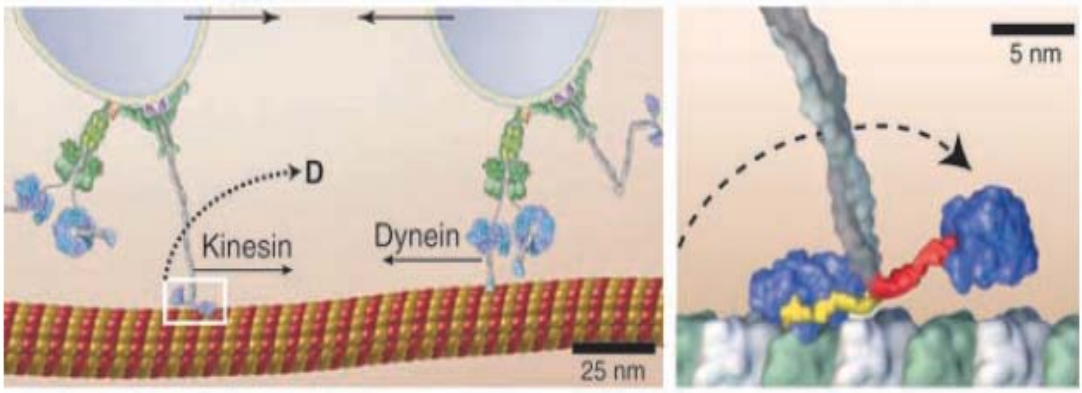

Figure 1.1.2 Schematic plot shows the working mechanism of kinesin and dynein motors. (adapted from reference [19]).

Dynein is another important member of the linear motor family. Dyneins have two major categories: axonemal dyneins and cytoplamic dyneins. Axonemal dynein works in a collaborative manner. They produce the bending motions that propagate along cilia and flagella by interacting between nine microtubule doublets arranged cylindrically around a pair of central microtubules [20-21]. During the 'power stroke', axonemal dynein undergoes a conformational change, which causes the microtubule-binding stalk to swing relative to the cargo-binding tail, pushing one microtubule forward. This sliding leads to bending movement of the cilia. Coordinated activation and inactivation of dynein molecules along different sides of the central microtubule enables a beating movement.

Similar to kinesin, cytoplasmic dyneins are also cellular transporters that drive a variety of fundamental cellular processes, including chromosome separation during mitosis and the positioning and function of many intracellular organelles [22-23]. Cytoplasmic dynein moves along cytoskeletal microtubules. However, they move towards the minus-end of the microtubule while kinesin moves to the plus-end. The

motor structure comprises between one and three heavy chains, each containing sites for ATP hydrolysis and microtubule binding [24]. Electron microscopy has revealed that the heavy chain folds to form a globular head with two elongated structures, the stalk and stem [25]. These two domains bind to the microtubule and cargo organelles, respectively [26]. At the beginning of a motor cycle, dynein binds tightly to a microtubule without any 'fuel' molecule. After ATP binds to the motor domain, dynein detaches from the microtubule. The detached dynein quickly hydrolyzes ATP and re-primes its conformation for a power stroke. Binding to the microtubule of the stalk domain promotes a concerted conformational change in the head ring, thereby releasing ADP and phosphate from the motor and generating a power stroke that pulls the cargo forward. This resets the system and completes one motor cycle [27-28].

1.1.3 Rotary Motors

F_1F_0 ATPase

F_1F_0 ATPase is considered to be the most important member of all molecular motors. It consists of two parts: the membrane embedded F_0 motor and the cytoplasmic F_1 motor (Figure 1.1.3 left). F_1F_0 ATPase uses the energy of transmembrane electrochemical gradient to synthesize ATP by a rotary mechanism.

The transmembrane F_0 motor is built from two different assemblies, conventionally called a 'stator' and 'rotor'. The rotor consists of a ring-shaped array of 10-14 double-helical *c*-subunits. The stator converts the ion motive force across the membrane into mechanical rotation of the rotor. The rotor connects to the γ-shaft which sits deep in the F_1 motor. Therefore mechanical torque is delivered to the F_1 motor through this connection. The F_1 motor consists of a hexamer of alternating α and β subunits whose interfaces harbor six nucleotide binding sites. Three of these

are used for ATP synthesis and the other three are used only as structural support. Due to the irregular shape of the coiled-coil γ-shaft, the rotation of the shaft interacts with the $\alpha_3\beta_3$ hexamer, which causes great conformational changes and catalyses ATP synthesis.

In the past decade, the progress of the F_1F_0 study has been rapid and we have learned much about its structure and function. More recently, steps in the motor's rotation were observed, supporting Boyer's hypothesis that one ATP molecules is generated per 120° of rotation [29-30]. Successful mathematical models have been constructed to illustrate the working mechanism at a molecular level [31-33]. Furthermore, the F_1 part can also operate in reverse by hydrolyzing ATP at a high ATP concentration and driving the F_0 motor in reverse as an ion pump. This property is regarded as highly promising for future bionanotechnology applications [34][19].

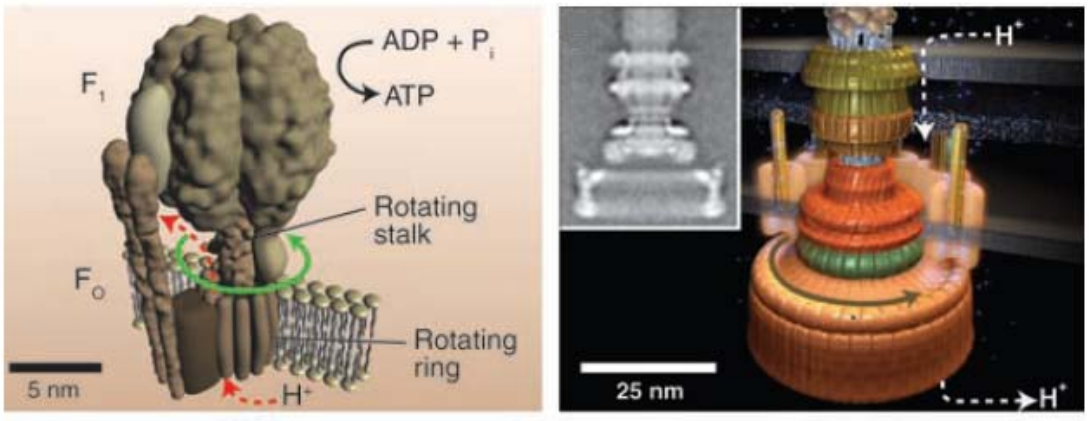

Figure 1.1.3 On the left: schematic plot of the F_1F_o ATPase. The F_1 hexamer contains three catalytic sites alternating with three noncatalytic sites. The rotation of the central shaft is driven by the F_o motor using the energy of transmembrane ion motive force. The shaft is eccentric, so that its rotation sequentially stresses the catalytic sites to release ATP. Details of the structure and Boyer's ''binding change'' model can be found in references [35-37]. Scale bar, 5 nm. On the right: schematic plot of the bacterial flagellar motor, which is reconstructed from images of the hook-basal bodies seen in an electron microscope [38-39]. The general morphological features are C-ring, MS-ring, P-ring, L-ring, hook, hook-associated proteins and filament. Scale bar, 25 nm. (adapted from reference [19]).

Bacterial Flagellar Motor

Flagellar rotation is the major means of bacterial motility. The bacterial flagellar motor is not only responsible for propulsion, but also plays an important part in chemotaxis. A thorough review of the BFM will be given in the following section.

1.1.4 Molecular Motor Applications

Given the wide variety of essential biological functions that motor proteins serve, it is not surprising that malfunction of many motor proteins is responsible for various diseases. Understanding their working mechanism provides guidance for developing drugs that recover or fix their normal function. Also promising is the engineering future of molecular motors to form nano-scale machines. At such small sizes, fluid transportation is dominated by low Reynolds number dynamics and becomes highly inefficient if driven by pressure gradient. Hence extensive efforts have been made to utilise molecular motors for the purpose of microscopic transportation and even preprogrammed medicine delivery.

1.2 BACTERIAL FLAGELLAR MOTOR

Flagellar rotation is one of the major means for bacterial motility. Using the transmembrane electrochemical H^+ (or Na^+) motive force to power rotation of the bacterial flagellar motor (BFM), free-swimming bacteria can propel their cell body at a speed of 15-100 μm/s, or up to 100 cell body lengths per second (reviewed in [40-41]).

The *Escherichia coli* (*E. coli*) BFM is the best understood among all BFMs. *E. coli* is a gram-negative bacterium. It is a rod-shaped cell, about 1 μm in diameter and 2 μm long. A cell contains about four extracellular helical flagellar filaments (on

average) each driven at its base by a rotary motor that is located at random positions on the cell surface. The major part of the BFM is embedded in the cell envelope and the rotor connects to the extracellular filament (Figure 1.2.1 a). A motor is about 50 nm in diameter and contains more than 20 different protein parts. In the following section, a thorough review of the BFM is given.

1.2.1 Structure

A schematic plot of the key components of the *E. coli* BFM is given in Figure 1.2.1 b, derived from collected research of electron microscopy, sequencing and mutational studies. More recently, crystal structures of some of the proteins have become available (reviewed in [42]). In Figure1.2.1 b, we see that in the extracellular part of the cell, a long flagellum (about 5 or 10 times the length of the cell body) is connected to the motor through the hook domain. The flagellum and the hook are formed by polymers of flagellin (FliC) and hook protein (FlgE), respectively. The mechanical packing structure of the flagellum and hook are completely different so that the flagellum is rigid but the hook is flexible [43-44]. Under the hook is the BFM basal body, which spans across the outer membrane, peptidoglycan and inner membrane into the cytoplasm of the cell. The basal body comprises a rod connecting four protein rings: the L-ring, P-ring, MS-ring and cytoplasmic C-ring (reviewed in [42]). Functionally, the basal body is the rotor of the BFM, which rotates the flagellum when torque is applied to it. Around the periphery of the MS-ring, there is a circular array of 10-12 stator complexes [45]. Each complex is made up of the proteins MotA and MotB in an A_4B_2 stoichiometry [46]. Both MotA and MotB span the cytoplasmic membrane, forming two ion channels in the centre of the A_4B_2 structure. The peptidoglycan-binding motif of MotB is a structural linker that anchors

the stator complex to the rigid framework of the peptidoglycan. MotA has four transmembrane α-helical loops [47]. Ion binding/unbinding to the channel in stator causes conformational changes in the stator complex, which later delivers torque to the rotor via rotor-stator interaction. Mutational studies that modify protein expression of individual components of the BFM found that there are critical charged residues on MotA cytoplasmic loops that interact electrostatically with charged residues on the C-terminus of FliG on the C-ring [48]. This interaction is believed to account for the torque generation mechanism in the BFM (the torque generation mechanism will be discussed further in Chapter 3).

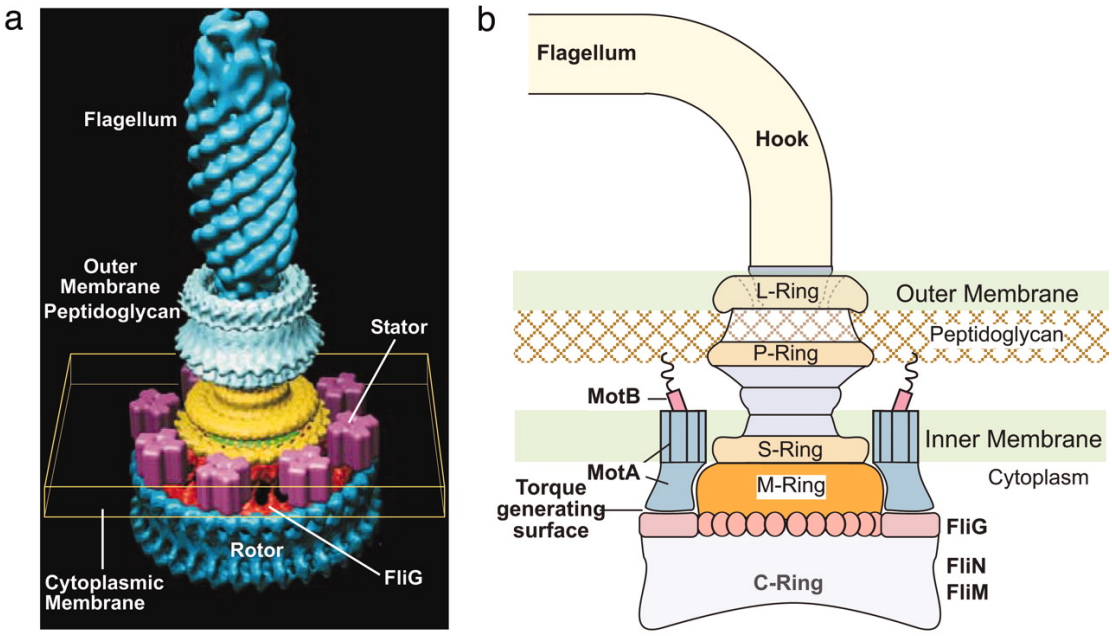

Figure 1.2.1 The BFM. (a) The overall structure of the BFM. Figure is courtesy of David DeRosier. (b) A cartoon plot of the key structural components involved in torque generation.

At the bottom of the basal body, FliG, FliM, and FliN constitute the C ring and are also referred to as the "switch complex," since mutations in this region often lead to defects in switching function. The chemotactic signaling protein, CheY-P, which is produced by the chemotactic network in the cell, binds to FliM. This binding event increases the probability that the motor rotates in the clockwise (CW) direction

by a not-yet-clear conformational change at the torque generating interface (more of this will be discussed in Chapter 5).

1.2.2 Power Input

The bacterial flagellar motor is powered by the flow of ions down an electrochemical gradient across the cytoplasmic membrane into the cell. The ions are typically H^+ (protons) in *Escherichia coli* and Na^+ in *alkalophiles* and marine *Vibrio* species. The protonmotive force (pmf) consists of two parts:

$$\Delta\tilde{\mu} \equiv pmf = \underbrace{\Delta\psi}_{\substack{\text{membrane}\\ \text{potential}}} + \underbrace{2.303\,\frac{k_B T}{e}\,\Delta pH}_{\substack{\text{Transmembrane ion}\\ \text{concentration gradient}}}.$$

formula (1.1)

The first contribution is from the transmembrane electrical potential gradient. The fluid inside and outside a cell is highly conductive, but a cell's plasma membrane is resistive. The membrane potential arises from the electronic filed generated by different concentrations of cations and anions across the membrane, which is maintained by ion transporters embedded in the membrane. The second part is due to the entropic effect of transmembrane pH difference. Here k_B is the Boltzmann constant, T the absolute temperature, and e the proton charge (reviewed in [40]).

At room temperature and *E. coli*'s normal growth conditions, the electrical potential contribution is about 120mV while the pH difference gives an extra 40mV, which in total equals 160mV. In the case of the chimera motor, which uses the *Vibrio* stator and *E. coli* rotor, the membrane potential is 140mV. With the external [Na^+] concentration at 85mM and internal [Na^+] concentration at 12mM, the total smf is approximately 190mV [49].

1.2.3 Power Output

To understand the mechanism of the flagellar motor we need to understand the mechanochemical cycle of torque generation and how it couples ion flux to motor rotation.

Like macroscopic machines, the torque-speed relationship gives a full picture of the power output of the BFM under external loads, and it also indicates the energy conversion efficiency. Moreover, the torque-speed curves, measured with increasing stators number, shed light on how individual torque-generating units cooperate and the duty ratio of the motor [50].

Experimentally, two different methods have been used to measure the torque-speed relationship of the BFM. The first method is by electrorotation, in which a cell is tethered to a glass coverslip by a single flagellar filament. External torque, τ_{ext}, is applied to the cell body with a high-frequency rotating electric field, and the rotation rate of the cell body, ω, is monitored optically [51]. A torque balance on the motor gives $\zeta\omega = \tau_M + \tau_{ext}$, where τ_M is the torque generated by the motor. The frictional drag coefficient is $\zeta = \zeta_M + \zeta_L$, where ζ_M is the drag coefficient due to internal friction in the motor and ζ_L is the external drag coefficient of the load, in this case, the cell body. The motor torque vs. speed curve is derived from the usual external load torque vs. speed curve as follows. The motor is broken by applying a large external torque to force rotation in the reverse direction. Next, the external torque, τ_{ext}, is applied to the broken motor, for which the force balance relation is $(\zeta_M + \zeta_{ext})\omega' = -\tau_{ext}$. Therefore, the motor torque is given by subtracting the broken motor speed from the motor speed: $\tau_M = (\zeta_M + \zeta_L)(\omega - \omega')$.

The second method is to tether a polystyrene bead to the stub of a flagellum, with the cell fixed to the surface of a glass coverslip (technical details will be given in the next section). The rotation speed of the bead is monitored in a weak optical trap while the viscosity of the external medium is rapidly changed by adding Ficoll [52] or while the drag coefficient of the bead is changed by varying the bead size [53]. In this case, the motor torque is calculated from $\tau_M = (\zeta_M + \zeta_L)\omega \approx \zeta_L \omega$, where the bead drag coefficient ζ_L can be calculated from the Stokes formula.

In the torque-speed curve of the *E. coli* BFM, the torque remains approximately constant up to ~ 170 Hz at 23ºC, and then drops abruptly to zero beyond a 'knee' velocity of ~ 300Hz. The sodium-driven flagellar motor exhibits a similar motor output relation with a higher 'knee' speed and zero load speed. Experiments that control the pmf show that the motor rotation speed depends linearly on the pmf in both low and high load regimes [54]. The unusual motor torque-speed relation and pmf dependence are crucial to understanding the underlying working mechanism of the BFM, and thus have been subject to extensive experimental and theoretical investigations.

1.2.4 Stepping

The BFM has long been suspected to be a stepping motor, but only recently was experimental evidence found. Steps in the F_1 ATPase were first seen in 1998 [29], and later, substeps were resolved [30]. However, observation of steps in the BFM is much more difficult in that several technical obstacles are hard to overcome. First, the step size in the BFM is very small. Stochastic analysis shows that the step number per revolution increases linearly with stator number and in a fully expressed (full stator) motor this number is about 400 steps per revolution [55-56]. One can estimate the

number of steps per revolution with a single stator by dividing this number by 11 (the stator number of a fully resurrected motor [57]). Or one can consider the 26-fold symmetry of FliG on the C-ring. The expected $2\pi/36$, or $2\pi/26$ stepsize calculated by the above two means are all very small compared to the $2\pi/3$ stepsize of the F_1 ATPase. Second, the wild type *E. coli* BFM runs very fast and its energetics are hard to control. Third, there is an intrinsic flexibility in the BFM system: the hook. When an indicator (latex bead or fluorescent bead) is attached to the flagellum, the elasticity in the hook smoothes the indicator movement. Even if the motor is making discrete steps, the indicator trajectory will be filtered into a continuous curve.

Only very recently have the technical problems outlined above been solved. Sowa *et al.* constructed a chimera motor, with sodium driven stators in an *E. coli* BFM background. With the new motor, they managed to express only one stator under low sodium concentration. This results in a very slow rotation rate, which leads to a relatively long dwelling time between steps, making step detection easier. An optical trapping system with high temporal and spatial resolution was used while a small indicator (a latex bead of diameter 0.2-0.5 microns) was attached to the flagellum. This reduced the relaxation time of the hook-bead system. Finally, 26 steps per revolution were confirmed [58] for the first time. Furthermore, with improved angular resolution and better control of the motor speed, information about key statistical quantities (such as step sizes with multiple stators, dwelling time distribution between steps) can be obtained. However, the detailed torque generation mechanism remains unclear.

1.2.5 Switching

In the low Reynolds number world, bacteria can not change their swimming direction by steering wheel. They depend on the thermal fluctuations from the surrounding environment to rectify their direction. The BFM has two rotation modes, counterclockwise (CCW) and clockwise (CW) (as viewed along a filament from its end toward the body). When the motor spins CCW, all of its flagellar filaments form a bundle that pushes the cell steadily forward. When one of the motors spins CW, these filaments fly apart and the cell tumbles. The BFM switches stochastically from CCW to CW direction and hence the cell repeats a 'run'-'tumble'-'run' pattern. This enables a chemotactic navigation in a low Reynolds number environment (reviewed in [40]). The probability of rotation direction is tuned by a chemotactic signaling protein, CheY. When the chemoreceptors sense attractant/repellent in the surroundings, less/more CheY will be phosphorylated. When the phosphorylated form of CheY, CheY-P, binds to the switch complex, the chance of CW rotation is enhanced, leading to more 'tumbling' and the opportunity for the cell to escape from the repellent.

1.3 EXPERIMENTAL TECHNIQUES

This is a review of the standard experimental techniques used in the study of the BFM. The results presented in Chapter 5 are from these experimental setups.

1.3.1 Optical Trapping System

Since their invention just over 20 years ago optical traps have been widely used for research purposes in both physics and biology, ranging from the cooling and trapping of neutral atoms to manipulating live cells and viruses [59-62]. Optical traps implement a highly focused laser beam to hold a dielectric particle. Because of the exchange of momentum between the trapped particle and the incident photons, a

potential well is created at the focus of the laser beam, which is able to attract the small particle to a fixed position in three dimensions. More recently, optical traps have been extensively employed in the experimental investigations of molecular motors (reviewed in [62]). Their ability to apply piconewton forces to micron-sized particles, while simultaneously measuring displacement with nanometer precision, makes them the best tool in practice. With the help of optical traps, the stepping behaviour of the linear motors myosin, kinesin and dynein has been resolved. The implementation of 'force clamps' and 'position clamps' combining optical traps with controllable feedback systems provides more information about the motors' mechanochemical cycles and working mechanisms [17]. In our case, the trap is specially designed to work with rotary motors. Figure 1.3.1 is a schematic plot of the optical trapping system we use (published in [63]).

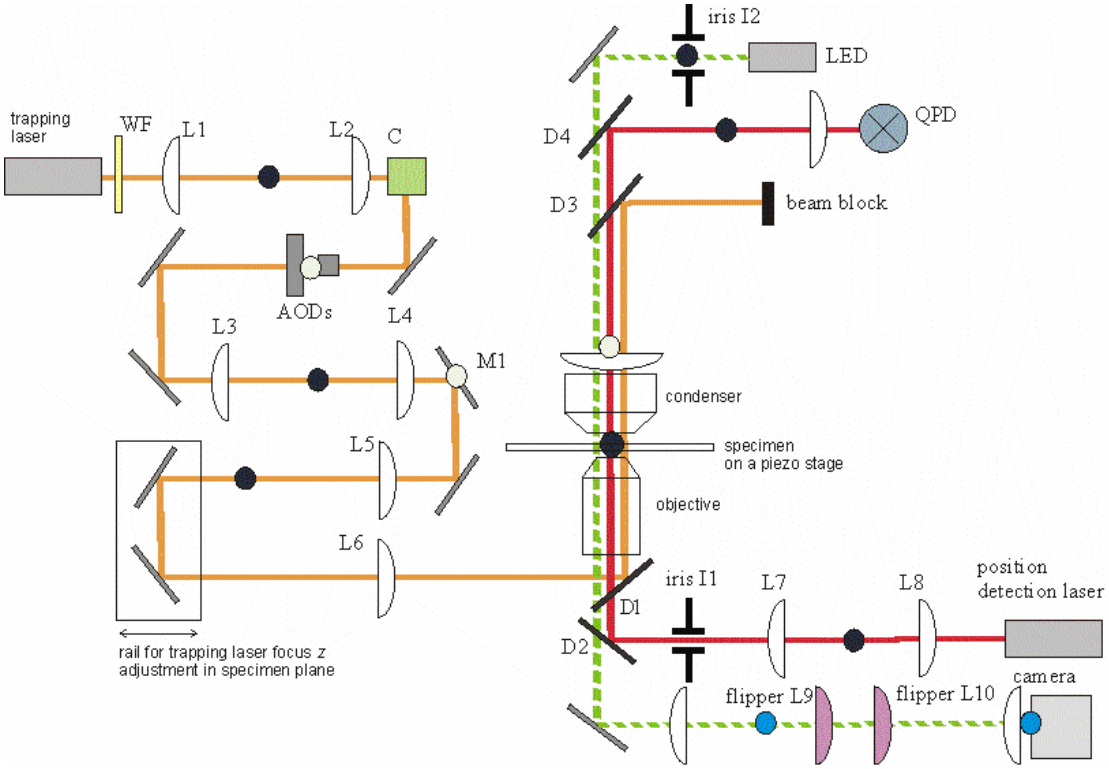

Figure 1.3.1 Anatomy of a laser trapping system. Figure is courtesy of Teuta Pilizota. Details of the building and calibration process can be found in our publication [63]. The system consists of two laser sources. The near-infra-red Ytterbium laser on the left is used to form the optical trap. The Helium-Neon laser on the right is used for position detection by back-focal-plane interferometry.

The system consists of an inverted microscope and two laser sources, which are used for detection and trapping, respectively. The basic setup is a bright-field imaging microscope comprising a light-emitting diode, high N.A. objective, light condenser and high-resolution CCD camera. Above the objective is the specimen slide holding position, which is mounted on a 3-axis piezo-electric stage. Position detection on the specimen plane is by back-focal-plane interferometry method using a Helium-Neon laser. The beam is first focused in the specimen plane by the objective lens and later collimated onto the face of a quadrant photodiode detector (QPD). The actual optical trap is formed by a separate light path on the left using a near-infra-red Ytterbium fiber laser. Acousto-optic deflectors in the light path are finely controlled by a digital signal processing board, which enables fast and precise movement of the trap focus in the specimen plane. Data acquisition, feedback calculations and control of the optical trap are all centrally managed by a host computer with Labview. With this system, we are able to accurately measure the rotation speed of an indicator attached to the flagellum of a BFM and apply fine manipulation of the indicator, through acceleration, deceleration, ‘angle clamp’ and ‘torque clamp’ techniques.

In Chapter 5 of this thesis, this optical trapping system is intensely used to investigate the switching dynamics of the BFM. In those experiments, the power level of the Helium-Neon laser was attenuated at the back aperture of the objective to minimize photo-damage of the motor with two neutral density (ND 1) filters. The beam was projected onto a quadrant photodiode to detect bead displacement. The photo-current signals outputted by the quadrants were amplified using a current-to-voltage amplifier and sampled by a computer at 10 kHz using National Instruments hardware inputs. For the purpose of studying the switching dynamics of the BFM, the optical trapping system we used was designed to provide the highest spatial and

temporal resolution achieved for monitoring motor activity. Custom LabView software allowed real-time monitoring of the spatial trajectory of the particular bead under examination and cells providing steady elliptical or circular trajectories were recorded for 30 seconds. This recording time avoided photo-damage concerns and limited cell behavioural variability, for the purposes of later categorising cells by bias. A method of fast attractant removal was used to provide cells with low and middle CW biases. The Labview software outputted bead X, Y position, angular position and radius against time, allowing the calculation of the instantaneous angular speed of the bead.

1.3.2 Tethered Cell Assay and Fast Bead Assay

Apart from the above experimental techniques in optics, we also need to establish robust procedures that maintain cells at good biological conditions for measurement.

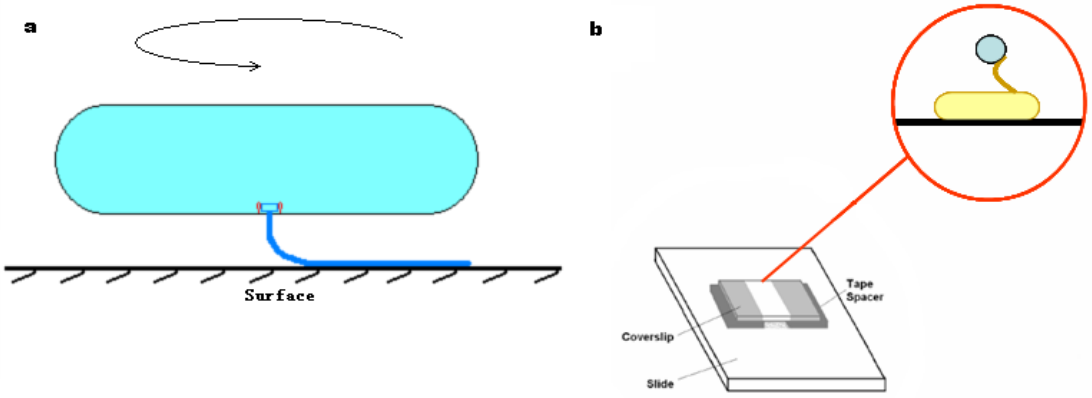

Figure 1.3.2 Schematic plot of the tethered cell assay and fast bead assay.

Bacteria preparation

During my study, the bacteria strains I have used are wild type *E. coli* KAF 84, non-switching *E. coli* KAF 95, and wild type stator inducible *E. coli* HCB 1271. Previous studies have found suitable growth conditions for these strains. Cell cultures

were prepared by adding 100 μl of strain stock taken from a $-80^{\circ}C$ freezer to 5 ml of tryptone-broth (1% tryptone, Difco, USA; 0.5% sodium chloride) and 5 μl of ampicillin (Sigma-Aldrich, UK). Cultures were grown for five hours in an incubator at $30^{\circ}C$, shaken at 200 r.p.m.

For the switching experiment described in Chapter 5, we collected data from about 3000 cell samples (*E. coli* wild type KAF84). *E. coli* non-switching cell (strain KAF95) and stator inducible cell (strain HCB1271) were used for comparison.

Tethered Cell Assay

The tethered cell assay was the dominant technique used in the early stage of BFM research. The *E. coli* cell (after incubation) is attached to a coverslip surface by its own flagellar filament and the BFM rotates the cell body in the reverse direction, as shown in Figure 1.3.2 a. The tethered cell assay is easy to make and since the cell body is relatively large, measurement of rotation rate is possible even with low resolution video records. However, in the tethered cell assay, as the external load of the BFM is the whole cell body, rotation rate is normally very slow, below 20Hz. This method only shows how the BFM operates in a low-speed, high-load regime. To explore the full torque-speed relationship of the BFM, we need a better controlled cell assay.

Fast Rotation Bead Assay

The bead assay method attaches small polystyrene bead to a truncated flagellum of the BFM (Figure 1.3.2 b). By monitoring the rotation of this indicator in the optical trapping system, we gain a better resolution.

Compared to the tethered cell method, in the bead assay, the viscous load on

the motor depends closely on the bead diameter and the eccentricity of rotation. By varying the size of the bead attached to the motor, we are able to investigate the dynamical properties of the BFM in a full load range.

To construct a bead assay, we follow a custom developed procedure: after the cell culture is harvested, flagellar filaments are sheared by passing 7ml of fresh culture through a shearing device [52] made of two syringes with narrow gauge needles connected by polyethene tubing. When the cells pass through the tube rapidly, the gradient of the turbulent flow shears the flagella off. Normally, we shear 70 times at moderately high speed to ensure that the majority of cells are left with short flagella.

Sheared cells are spun down in a centrifuge for two minutes and washed in 1 ml of motility buffer (10mM potassium phosphate; 0.1mM EDTA (Sigma-Aldrich, UK) at pH 7.0; 1mM L-methionine; 0.05% lactic acid) three times with the final suspension in 250 μl to provide the desired cell density. At the same time, a slide that holds the bead assay in the optical trapping system needs to be prepared. Double sided tape is used to attach a potassium hydroxide-cleaned glass coverslip to a microscope slide. A tunnel is cut in the middle of the tape, which later is used to flow the cells in. 10 μl of poly-L-lysine (Sigma-Aldrich, UK) is first injected into the tunnel and left for one minute before being flushed out with 200 μl of motility buffer, thus providing a surface on the coverslip which the cells can be immobilized on. An illustration of a tunnel slide is shown in Figure 1.3.2 b.

In the last step, 10 μl of the cells is injected into the tunnel and left in a humidifier for ten minutes, with the slide placed upside down to allow cells to settle on the poly-L-lysine monolayer. Loose cells are then flushed out with 100 μl of motility buffer before injecting 10 μl of small latex beads (Polysciences Inc., Eppelheim, Germany; size ranges from 0.2 micron meter to 2 micron meter depends

on experimental requirements) at 0.5% concentration in motility buffer. The slide is again placed in the humidifier for ten minutes to allow the beads to settle and attach to the flagella. Loose beads are flushed out with 100 μl of motility buffer before the ends of the tunnel are sealed with vacuum grease to prevent evaporation from the sample. At this stage, the slides are ready to take measurements from the optical trapping system.

1.3.3 Flow Chamber

On top of the bead assay slide setup described above, a few more components can be easily added, among which the 'flow chamber' setup is most useful.

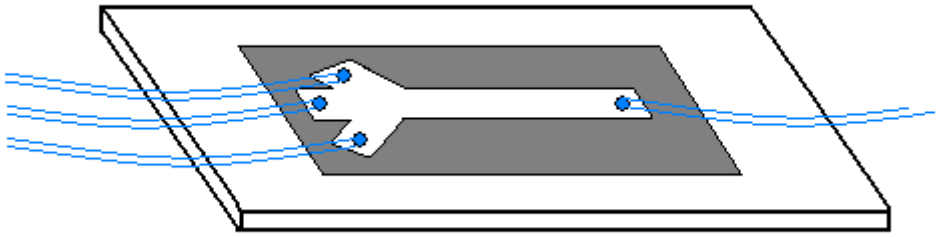

Figure 1.3.3 Custom built 'flow chamber' that allows the living environment of bacteria to be changed while taking measurements in the optical trapping system

In some experiments, it is often required that the rotation rate of the BFM be measured while its living environment is changed. For example, the switching behaviour of the BFM is controlled by the chemotaxis network and the cell can adapt to a new environment within minutes. Any research work which attempts to look at the switching dynamics will be restricted to a fixed chemotactic activity region if the cell sample is isolated. This problem can be solved with the 'flow chamber' setup. Before we stick together the slide and the coverslip, we drill holes on the bottom side of the slide at a size that thin polyethene tubes can just pass through (Figure 1.3.3). Later we glue the tubes to the slide and cut off the part above the top side of the slide.

Pre-designed double sided tape is used to stick the coverslip to the slide, which makes a tunnel in the middle with crossroads that connects the tube entrance points. With this new setup, injection and removal of solution is through the polyethene tubes. After we immobilize cells on the coverslip with beads attached, the inlet tubes are connected to large reservoirs of motility buffer with different attractant or repellent levels. While the slide remains firmly in the specimen plane of the microscope, we can gradually change the living environment of the bacteria by opening different inlet tubes without harming their activity. Therefore, this method allows a complete exploration of switching dynamics across a full bias range.

1.4 CONCLUSION

Molecular motors play indispensable roles in many fundamental biological processes. After a few decades' research endeavour, advanced experimental techniques have been developed for the study of molecular motors. The secrets of these remarkable machines are ready to be revealed.

CHAPTER 2

Mathematical Modeling of Molecular Motor Systems

2.1 THE PHYSICS OF MOLECULAR MOTORS

From a physicist's point of view, before we start modeling any particular molecular motor, it is wise to identify the general features of these 'tiny machines'. First, due to their small dimensions and aqueous living environment, molecular motors are subject to large thermal fluctuations and they have to develop an efficient strategy that generates directional movement out of the random environment. This strategy needs to make the most of their energy input, which is only slightly higher than that of the thermal bath (the free energy associated with hydrolysis of one ATP molecule is 12 k_BT; and that of proton motive force is 6 k_BT. The energy input is used in driving molecular transitions between key states in the motor's mechnochemical cycle, making the free energy source for each transition on the order of $\sim k_BT$). Second, the motors live in a world of low Reynolds number. They have no sense of inertia but a strong sense of viscous friction. A model needs an appropriate stochastic algorithm to describe the motor's movement in this damped and viscous environment. Third, similar to macroscopic motors, there is an accurate coupling between chemical

reaction and physical advancement in the molecular motor. Periodicity exists in both the reaction coordinate and the position coordinate.

Physical theories that aim to understand the fundamental working mechanism of molecular motors should be able to capture the above three features, especially the role of fluctuations in their operation, the nature of the mechanochemical coupling, and the efficiency and reversibility of energy conversion. The theory proposed by C. Bustamante, D. Keller, and G. Oster provides a good starting point for our understanding [64].

In their theory, the free energy landscape is used to model the driving force of both chemical reaction and physical movement. A system containing the motor molecule, the interacting filament track and surrounding molecules in solution possesses many degrees of freedom. Some are external variables and the others are internal, called the *system variables*. The same physical concept that has been widely used in statistical mechanics can also apply to the description of this system. The *system variables* of the molecular motor form an *n*-dimensional state space. Each point on the state space represents a unique configuration of the motor and has an associated free energy, the *potential of mean force*. The potential of mean force is primarily from three sources: (1) interaction energy within the motor (eg. rotor-stator interaction, arm-linker interaction), and between the motor and its track (if it has one) (2) chemical interactions between the motor and the fuel molecules (3) interactions of all of the above with the solvent environment. The motor moves in the state space from one point to another, forming a reaction pathway.

The basic role of molecular motors is to transfer chemical energy into mechanical movement. Therefore, among all the system variables, an important group measures the progress of chemical reactions. We call them the *chemical variable*. All

others will be called *mechanical variables,* which describe the relative movement of components within the motor or the progress of the motor along its track or, for rotary motors, the angle of rotation around its axis.

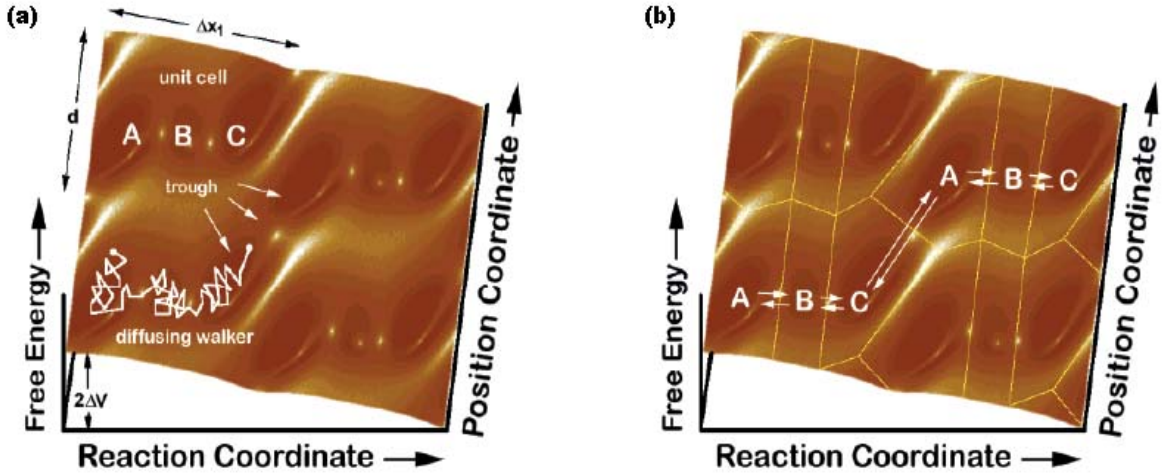

Figure 2.1.1 (a) Minimal potential energy surface that demonstrates molecular motor working mechanism. The surface is periodic in both the reaction coordinate and position coordinate, reflecting the cyclic nature of both enzymatic turnovers and motor cycles. The surface is tilted along the chemical axis, representing the driving force for the motor, i.e., the free energy of reaction. An externally applied load force would appear as a tilt of the surface along the position coordinate. The motor (system point) diffuses on this potential energy surface. The optimal reaction path way (the energy valley in the center connecting local minima) couples chemical energy to mechanical motion. (b) Correspondence between the potential energy surface and the kinetic representation of the motor. Diffusion between minima is equivalent to chemical transitions, which can be described by kinetic rate constants. (Figure is courtesy of reference [64])

In the simplest case, when the motor can be defined by only one chemical and one mechanical variable, an imaginary potential energy surface that demonstrates the principles of motor movement can be constructed (see Figure 2.1.1a). A motor that works in a higher dimension state space follows the same principle, but that is hard to visualize on paper.

In Figure 2.1.1a the periodicity in the reaction coordinate reflects the cyclic nature of biochemical turnover. During a chemical reaction, the motor undergoes a number of steps that correspond to changes in conformation and chemical state and

eventually resetting the system to the original state. For instance, the chemical steps typically involve catalysis of an ATP molecule (for example, as in myosin, kinesin, helicases, and F_1 ATPase), or translocation of an ion across an electrochemical gradient (for example, as in F_0 ATPase and the BFM). The periodicity in the position coordinate corresponds to the repeated steps in motor advancement along tracks or angular displacement (for example, steps in a linear motor, 120 degree steps in F_1 ATPase, and $2\pi/26$ steps in the BFM). On this free energy surface, thermal fluctuations are essential to motor movement in that they assist crossing of energy barriers. A cut through the free energy surface along the chemical coordinate gives a reaction free energy diagram. On this diagram, the relative position of each chemical state is shown as separate energy wells. A cut through the free energy surface along the position coordinate gives the potential of mean force which drives movement of the motor along its track or around its axis in a certain chemical state.

There are numerous ways that the motor can move on this free energy surface. However, the valley connecting all the local free energy minima in the center of Figure 2.1.1 a (arrows) is the optimal reaction pathway that nature chooses. Chemical transition is precisely coupled to mechanical motion as the slope of the surrounding energy barriers restricts the motor movement along the low-energy pathway. In this way, when the motor proceeds in the chemical coordinate, simultaneously, advancement in the position coordinate is achieved.

2.2 THREE LEVELS OF MODELING

The free energy surface in Figure 2.1.1 a is used to demonstrate the general principle of modeling molecular motors. The next question is how to reconstitute this

free energy surface for a particular motor based on available experimental information. There are three levels of modeling methods that we can use for this purpose [65].

2.2.1 All Atom Molecular Dynamics Simulation

The highest level is the all atom Molecular Dynamics (MD) simulation. Molecular Dynamics method follows the motions of all of the atoms of the motor and sometimes the surrounding water and other chemical molecules in the system. By solving Newton's equations using a variety of semi-empirical potential functions that model the forces between atoms, MD simulation reveals intrinsic information about protein conformational changes and ion channel properties (see review in [66]). Recently, this method has been used in the study of molecular motors [67-68]. The MD simulation reconstitutes the free energy surface from fundamental all atom-atom interactions. Therefore the motor mechanism can be best understood once a correct MD model is built. However, this is not easy in practice. First, for an accurate MD simulation the atomic structures of the system are usually needed beforehand. Second, due to current computer capability, a large protein system involving many components in a complicated solvent environment is hard to solve. Third, the typical simulation time achievable with MD simulation is normally short, long time traces are hard to produce.

The above three limitations restricts the use of the MD method in molecular motor modeling. Molecular motors are normally large protein complexes with many components. Not all of them have a well determined atomic structure, especially the parts embedded in the cell membrane, which are extremely hard to crystallize. Additionally, molecular motors make remarkable and coordinated mechanical movements triggered by chemical catalysis of the fuel molecule. To capture the force

generation picture, a long time simulation of a multi-body system is normally required. This time scale (ms) exceeds the typical MD simulation time ($ns \sim \mu s$). Therefore, applying MD to domains of the molecular motor yields valuable insights, but the time to study the whole motor using MD has not yet come.

2.2.2 Discrete Kinetic Models

Compared to the complicated MD simulations, the simplest way of modeling is with discrete kinetic models. Kinetic models have been widely used in the description of chemical reactions. A kinetic model is usually based on the assumption that the free energy surface can be divided into discrete potential wells, which are separated by rather high potential barriers [69]. The system dwells in the potential well for most of the time, but can capture large thermal fluctuations and make instantaneous barrier-crossing transitions. This process is normally referred to as a Poisson process and the average number of transition events in a unit time is defined as the transition's kinetic rate.

The molecular motor cycle can also be modeled as Markov transitions between a discrete set of states connected by kinetic rates. For example, for ATP driven motors, the discrete states of chemical status are normally: catalytic site Empty (E), ATP bound (T), ADP/Pi bound (DP), and ADP bound/Pi release (D); for ion driven motors, the discrete states of chemical status usually are: ion bound (On) and ion release (Off).

In Figure 2.1.1 b, we show the equivalent kinetic representation of the motor reaction pathway shown in Figure 2.1.1 a. We assign state A, B, C to the three local energy minima. Therefore, a continuous optimal path on the state space can be replaced by a three states kinetic model.

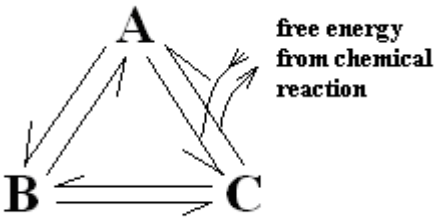

Figure 2.2.1 A three states kinetic model.

Next if we know the portion of free energy U_{ij} consumed and the percentage of mechanical advancement L_{ij} completed in each transition, the kinetic rates between states can be modeled as a function of the free energy and motor force via an exponential Boltzmann factor.

$$k_{ij} = k_0 \exp(\lambda \Delta G_{ij} / k_B T)$$
$$k_{ji} = k_0 \exp\left[(\lambda - 1)\Delta G_{ij} / k_B T\right]$$

$$\Delta G_{ij} = U_{ij} - Torque \times L_{ij} \qquad \text{formula (2.1)}$$

where λ is a free parameter that defines how ΔG influences the kinetic rate and k_0 the transition attempting rate.

In this way, a complete treatment of the potential of mean force is simplified to a set of kinetic transitions. The ΔG in the exponential factor reflects the physical ingredients that free energy from chemical transition assists forward transitions and output force opposes them. By solving the master equation that corresponds to a steady state of the kinetic model, one can retrieve the force-speed relationship of the molecular motor. A successful example following this approach is the three states model Richard Berry used to explain the torque-speed relationship of the BFM in reference [51].

However, kinetic models also have obvious limitations. They usually contain a large set of parameters. These parameters form a broad model space. In order to

reproduce the experimental results, the optimization process searching the model space requires a lot of computation power/time. Additionally, kinetic models are not specific to a certain system. The same framework can be used to explain various phenomena and even cross area results, with no or little modification. Completely opposite predictions can be made from different regions in the model space. This great compatibility to different predictions loses particularity of each model, therefore undermines the value of each kinetic model. For example, a four state kinetic model is often used to describe the function of the kinesin motor and with a certain parameter set, it reproduces some experimental results. The same model, however, with a new parameter set, can explain properties of the myosin motor. In this case, for the purpose of fitting experimental data, we have two different sets of parameters for kinesin and myosin, but it is usually very difficult to relate such choices to the fundamental distinctions between the two motors, such as differences in size, structure, molecular weight, biological activities, etc. To conclude, kinetic models are useful in providing phenomenal descriptions, but usually hard to reveal insights of the systems being modeled.

2.2.3 Markov-Fokker-Planck Model

The method I used in this thesis to model molecular motors is an intermediate between all-atom MD simulation and discrete kinetic models.

The motor proteins constitute a system with many degrees of freedom (DoF). Most of the DoF are high-frequency modes, eg. chemical transitions, compared with mechanical advancement. Therefore, the effects of these DoF can be averaged out. On the free energy surface we presented in Figure 2.2.1 a, if one can identify the primary chemical states, intersection planes at these discrete points along the position

coordinate gives you a set of primary driving potentials. The dynamics of the motor can be described by a set of such potentials of mean force as functions of these low-frequency DoF. In this way, the all-atom MD simulation of the system can be approximated by a combination of Langevin simulations of the motor in these driving potentials along the position coordinate and kinetic (Markov) jumps between potentials describing chemical transitions. This new approach can be formally retrieved from the all-atom MD simulation by selecting some primary degrees of freedom, projecting out all the remaining degrees of freedom. Also, this Markov-Fokker-Planck formalism replaces the discrete states of kinetic models with continuous potential functions defined on geometrical coordinates that represent the major conformational motions of the protein.

The Markov-Fokker-Planck model effectively simplifies the all atom MD simulation by treating the chemical process as kinetic transitions while dealing explicitly with mechanical movement. The particularity of each motor isn't lost as with pure kinetic model as these driving potentials have to be constructed from available molecular structures and relevant experimental results. We emphasize that Markov-Fokker-Planck models complement MD simulation and kinetic models; each has its proper place in understanding protein motors, depending on the users' requirement and expectation.

2.3 MATHEMATICAL FORMALISM OF THE MARKOV-FOKKER-PLANCK MODEL

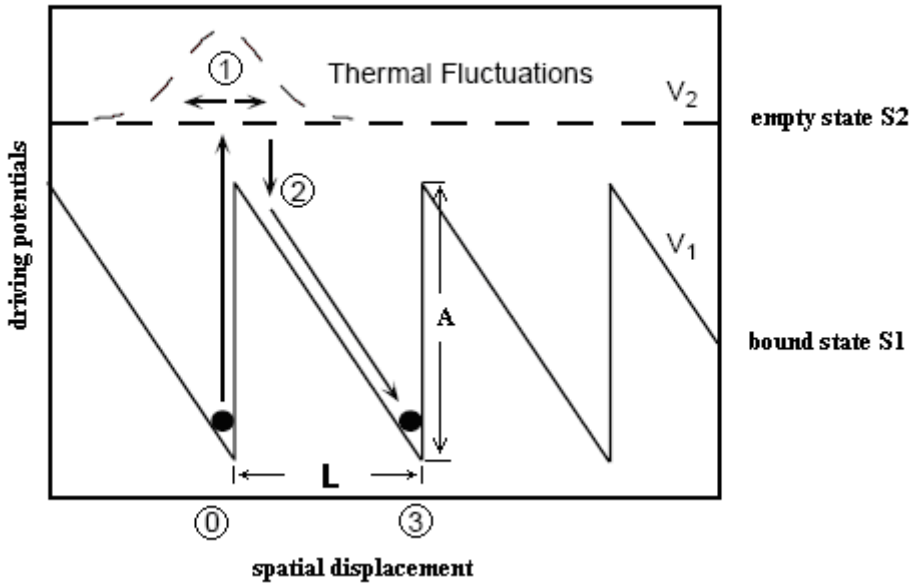

Figure 2.3.1 A simple 'flashing ratchet' model that illustrates the basic working mechanism of a linear motor.

In Figure 2.3.1, we show the simplest Markov-Fokker-Planck model that can be used to illustrate the working mechanism of a linear walking motor [70]. The model consists of two states, S1 and S2. The motor can be in one of these two chemical states: S1 corresponds to the nucleotide-binding site being occupied and S2 corresponds to it being empty. In the empty state, the motor is dissociated from the polymer track and subject to free Brownian motion. In the bound state, the motor attaches to the track and during hydrolysis of the fuel molecule, a power stroke pushes the motor forward by the step size L. The kinetic scheme for the chemical reaction is

$$S1 \underset{k21(x)}{\overset{k12(x)}{\rightleftharpoons}} S2$$

where the transition rates k12(x), k21(x) are dependent on the position coordinate x. The potential of mean force we assign to the empty state is a constant zero and that of the bound state is a saw tooth potential of period L and amplitude A. Although simply

constructed, this model captures the primary feature of a dynein motor. When the motor is in the bound state, it dwells at the local minimum of the saw tooth potential, eg. position 0. Dissociation of the fuel molecule switches the motor to the empty state. Hence, the motor undergoes free Brownian motion around position 1, it has the same probability to diffuse to the left side or right side of position 1. When the next fuel molecule binds to the motor, it brings the motor to S1 again. The motor can be caught at position 0 or position 2. If at position 0, then the hydrolysis of the fuel molecule is futile, producing no mechanical movement; if at position 2, the driving slope of the saw tooth potential (power stroke) pushes the motor forward by step size L.

This 'flashing ratchet' is the simplest Markov-Fokker-Planck model that can be used to understand motor function. Next, we discuss how to solve the model numerically. There are mainly two approaches to solve the above two-state model. The first way is the classical Langevin simulation.

2.3.1 Langevin Simulation Approach

The dynamics of a particle undergoing one-dimensional Brownian motion (here referred to as the motor) subject to a potential can be described by the following Langevin equation: (In the low Reynolds number case, the inertial term has already been neglected [2])

$$\zeta \frac{dx}{dt} = -\frac{\partial \phi_i(x)}{\partial x} + f(t); \qquad \text{i =empty, or bound} \qquad \text{formula (2.2)}$$

where ζ is the frictional drag coefficient of the motor, x is the position coordinate, t is time, ϕ_i is the driving potential of the empty state or bound state, and *f(t)* is the Brownian force due to thermal fluctuations. The statistical properties of *f(t)* are

$$\begin{aligned} &< f(t) >= 0 \\ &\text{cov}[f(t) f(s)] =< f(t) f(s) >= 2kT\zeta\delta(t-s) \end{aligned} \qquad \text{formula (2.3)}$$

where T is the temperature in Kelvin.

A random variable described as such is referred to as Gaussian White Noise.

Numerical simulation of the Langevin equation can be performed by introducing the Weiner Process,

$$x(t+\Delta t) = x(t) - \frac{1}{\zeta}\frac{\partial \phi_i(x)}{\partial x}\Delta t + \sqrt{2D\Delta t}Z \qquad \text{i=empty, or bound} \qquad \text{formula (2.4)}$$

where Z is a standard normal random variable, i.e. with mean 0 and variance 1, and $D = \frac{k_B T}{\zeta}$ through the Einstein relation. With this numerical algorithm, one can update the position of the motor systematically. First, we specify the simulation time step Δt (usually a very small value for accurate modeling and convergence of the result) and the initial chemical state i and position x of the motor. Then in each Δt, we calculate the deterministic displacement '$-\frac{1}{\zeta}\frac{\partial \phi_i(x)}{\partial x}\Delta t$' according to the driving potential of this state. The motor trajectory is updated following equation (2.4) with a random variable generator to mimic the stochastic force due to thermal fluctuations. At the same time, a Monte Carlo process determines whether the motor will stay or jump to the next chemical state according to the kinetic scheme. The new chemical state i and position x of the motor is taken to the next iteration.

The Langevin simulation approach readily shows the stepping trajectory of the motor under all stochastic forces, although trajectories will differ given the same initial conditions due to the stochastic nature of the Brownian force and chemical transitions. Moreover, even a detailed examination of the path cannot distinguish whether a particular displacement (eg. step) is caused by a Brownian fluctuation or the effect of the driving potential. Only by tracking the particle for a long time and computing the average position vs. time can one detect that the diffusion of the

particle exhibits a drift velocity in the direction of the force. Therefore average properties of the motor (eg. speed) can only be obtained by running a very long time simulation and dividing the final displacement by the total simulation time.

2.3.2 Coupled Fokker Planck Equation Approach

The second way to solve the two-state model is through the Fokker-Planck equation [71]. A better way to think about stochastic motion is to imagine a large collection of independent particles moving together. Then we can define the concentration of particles at position *x* and time t and track the evolution of this ensemble. The Fokker Planck equation works directly with the probability distribution functions. Average properties of the stochastic system can be represented as a function of the final steady state probability distribution function. For the above two-state model, we use $\rho_1(x,t)$, $\rho_2(x,t)$ to represent the probability density function that the motor can be found at position *x* and time t in state 1 (bound) and 2 (empty) respectively. The coupled Fokker-Planck equations governing the propagation of the two states probability density functions are:

$$\frac{\partial \rho_1(x,t)}{\partial t} = D\frac{\partial}{\partial x}\left(\frac{1}{k_B T}\frac{\partial \phi_1(x)}{\partial x}\rho_1(x,t) + \frac{\partial}{\partial x}\rho_1(x,t)\right) - k_{12}\rho_1(x,t) + k_{21}\rho_2(x,t)$$

$$\frac{\partial \rho_2(x,t)}{\partial t} = D\frac{\partial}{\partial x}\left(\frac{1}{k_B T}\frac{\partial \phi_2(x)}{\partial x}\rho_2(x,t) + \frac{\partial}{\partial x}\rho_2(x,t)\right) + k_{12}\rho_1(x,t) - k_{21}\rho_2(x,t)$$

formula (2.5)

Comparing formula (2.5) with the Langevin approach, we notice that the Brownian force is replaced by the diffusion term and the effect of the deterministic forcing is captured by the drift term. Equation (2.5) further couple chemical transitions by probability flux in /out of state 1 and 2. The above Fokker-Planck equation must be solved with appropriate boundary conditions, which are closely dependent on the

system being modeled. For the two-state 'flashing ratchet' we show in Figure 2.3.1, we can choose a periodic condition. At steady state, the total probability flux in the spatial dimension is

$$J = -D(\frac{1}{k_B T}\frac{\partial \phi_1(x)}{\partial x}\rho_1 + \frac{\partial}{\partial x}\rho_1)$$
$$- D(\frac{1}{k_B T}\frac{\partial \phi_2(x)}{\partial x}\rho_2 + \frac{\partial}{\partial x}\rho_2) \quad \text{which is a constant independent of } x$$

After the coupled Fokker Planck equation is solved, the average speed of the motor can be easily calculated as $v = LJ$.

To conclude, in this section, we demonstrated the two primary mathematical approaches that can be used to deal with a stochastic system and their application to a simple two-state model. Each formalism has its own advantages and shortcomings. The implementation of the Langevin simulation is often straightforward, but the user has to be cautious about the time step size and the overall simulation is time consuming. On the other hand, the Fokker-Planck approach yields the average quantity of the system by solving the steady state probability distribution function. However, this often involves complicated numerical techniques to solve the PDEs. In practice, these two methods complement each other and people usually use both.

A successful application of the Markov-Fokker-Planck model in the study of molecular motors is to the F_1F_0 ATPase, pioneered by George Oster, Hongyun Wang, Timothy Elston and Jianhua Xing *et al.* Detailed information can be obtained from their publications [31-33]. The Markov-Fokker-Planck model can also be used to explain protein translocation [72], biomolecular transport [73] and protein allostery [74].

2.4 CONCLUSION

The unique size and living environment of molecular motors requires a special stochastic modeling treatment. Molecular motor operation can be conveniently visualized as stochastic motion on a free energy surface. The optimal path on the surface ensures molecular motor mechanochemical coupling. All atom MD simulation, kinetic model, and Markov-Fokker-Planck model are modeling approaches at different levels. In this thesis, we focus on the Markov-Fokker-Planck model. The key element in using this model is to identify the primary chemical states and the rates of transition between them. The driving potentials along the mechanical coordinate of each state can be determined from available knowledge of protein geometry. Langevin simulation and the Fokker Planck equation are the mathematical tools to solve the Markov-Fokker-Planck model.

In this chapter, we finished the theoretical preparation and are ready to start mathematical modeling of the bacterial flagellar motor system.

CHAPTER 3

The Torque-Speed Relationship of the Bacterial Flagellar Motor

Many swimming bacteria are propelled by flagellar filaments driven by a rotary motor. Each of these tiny motors can generate an impressive torque. The motor torque vs. speed relationship is considered one of the most important measurable characteristics of the motor and therefore is a major criterion for judging models proposed for the working mechanism. Here we give an explicit explanation of the physics behind this torque–speed curve.

This chapter is mainly reformed from my publication:

Xing, J., Bai. F., Berry, R.M. and Oster, G. Torque-speed relationship of the bacterial flagellar motor. *Proc.Natl.Acad.Sci.USA.* 103, 1260-1265 (2006).

Here I acknowledge the contributions from Jianhua Xing, Richard Berry and George Oster.

3.1 MODEL FORMATION

To understand the mechanism of the bacterial flagellar motor, we need to understand the mechanochemical cycle of torque generation and how it couples ion flux to motor rotation. Before direct step measurement, the torque–speed relationship

is the best probe that we can use to explore the mechanism. Experimentally, two different methods have been used to measure the torque–speed relationship of the BFM. The first method is electrorotation and the second method is to tether a polystyrene bead to a flagellar stub with the cell fixed to the surface of a glass coverslip.

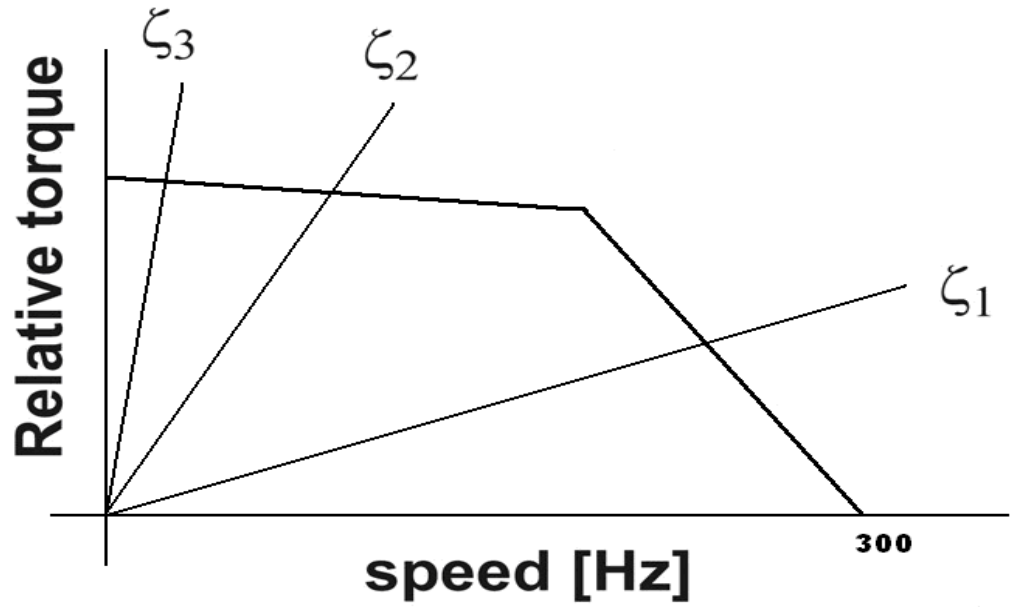

Figure 3.1.1 Idealized motor behaviour. The motor torque–speed curve is nearly constant up to a knee speed, whereupon it decreases nearly linearly. Here, torque is normalized to the maximum torque at stall ($\omega = 0$). For a given viscous load (characterized by its frictional drag coefficient, ζ_i, $i = 1, 2, 3$), the speed of the motor is determined by the intersection of the "load line" with the motor torque-speed curve.

These two methods give similar torque-speed curves for the BFM. In Figure 3.1.1, we show an idealized plot of motor torque (normalized to the maximum torque) vs. speed. At a given pmf, the motor–torque curve is swept out by varying the viscous drag on the load. The torque generated by the BFM remains approximately constant up to ≈170 Hz at 23°C and then drops rapidly beyond a "knee" velocity to zero at a velocity of ≈300 Hz. The sodium-driven BFM exhibits a similar motor torque–speed relation. Experiments using micropipettes revealed that motor rotation rates depend linearly on the pmf at the high load regime [75]. The unusual motor torque–speed relation and pmf dependence are thought to reveal properties underlying the working

mechanism of the BFM. Here we will show that those observations arise from some very general characteristics of the motor.

The lack of detailed information about the motor structure and the mechanochemical cycle leaves much room for speculative modeling, and indeed various models have been proposed for the working mechanism of the BFM (see reviews in reference[76]). However, the special shape of the torque vs. speed curve discussed above remains unexplained. Here, we will demonstrate that the mechanochemical behaviour of the BFM can be reproduced by any model that incorporates the following physical assumptions.

Assumption A. The rotation of the motor is observed through a soft elastic linkage between the motor and the viscous load.

The soft linkage arises from the elasticity of the "hook" region connecting the rotor and the flagellum and the linkage between MotB and the peptidoglycan (see Figure 1.2.1) [77]. The consequence of this compliant linkage is to allow the motor and the load to move on different characteristic time scales. When coupled to a large viscous load, the soft linkage produces the plateau region of the motor torque–speed curve.

Assumption B. Motor rotation and ion transport are tightly coupled.

First suggested by Meister *et al.* [78], this assumption is necessary to explain the linear pmf dependence at low speed, and the addition of equal increments of motor torque with each additional stator in resurrection experiments [79].

Assumption C. The power stroke is driven by a conformational transition in the stator that is triggered by the protons hopping onto and off the stator, probably via the MotB residue, D32.

The proton motions are much faster than the mechanical motion of the stator, so the stator conformational movement is the rate-limiting step for the motor. This assumption also was suggested by Gabel and Berg to explain the nearly linear pmf dependence at high speed [54].

Assumption D. The ion channel through the stator is gated by the motion of the rotor.

That is, access of the periplasmic protons to the stator-binding site is triggered by a rotor–stator interaction. Consequently, the ion conductance through the stator varies with the motor speed. This assumption is necessary to explain the non-linear shape of the torque–speed curve, especially the sharp transition at the knee between the flat and decreasing regions.

Current biochemical and structural studies imply that the motor torque is generated by conformational changes in the stator upon ion binding/unbinding to the negatively charged D32 residue on the MotB helices. This motion is transmitted to the rotor by means of interactions at the rotor–stator interfaces [48]. The details of these interactions will remain vague until the atomic structure of the stator has been determined; currently the structures of but a few portions of the rotor are available [80-81]. Here we construct our model based on the rotor–stator interaction model proposed by Blair and coworkers [82].

To generate sufficient torque, we assume that one power stroke cycle of the stator is driven by the binding free energy of two protons (the need for two ions is intensely discussed in reference [40-41] and investigated by a kinetic model in reference [51]) to the two negatively charged D32 residues on the two MotB helices in the stator. The binding energy of the protons to MotB is converted into a "flashing" electric field in the stator that triggers a pair of conformational transitions. The detailed dynamics of the motor can be described by the stochastic motion along the slow DoF (degree of freedom) driven by the multidimensional potentials of mean force.

In Figure 3.1.2a we show a schematic illustration of the torque generation mechanism of the BFM suggested by our model. In our model, one motor cycle consists of two steps:

Step 1: The stator can be modeled as an asymmetric bistable system, alternating between two free-energy potential minima as shown in Figure 3.1.2 a. At the end of previous cycle, D32 residues on the stator are unprotonated, and the stable conformation is as shown on the left; the cytoplasmic loop of one MotA (the right one in the figure) is down, engaging the rotor. Binding of two protons to the MotB D32 residues neutralizes them, allowing a thermally activated transition to the alternate conformational equilibrium to perform the first power stroke with the other MotA loop engaging the rotor. This process is characterized by the transition rate k_{on}, which is a composite of ion hopping on rates and the thermally activated conformational transition rate.

Step 2: At the end of the first power stroke, the two binding protons are released to the cytoplasm. This transition triggers another conformational change of the stator so the (right) MotA loop engages to the rotor to perform the second power

stroke. This process is characterized by the transition rate k_{off}, which is a composite of ion-hopping off rates and the thermally activated conformational transition rate. At the end of the cycle, the stator has returned to its conformation at the beginning of the cycle, with the rotor advancing one step to the right. During the entire two-step cycle, the rotor is almost always engaged, so that the duty ratio is close to 1. The stator loops interact electrostatically/sterically with 26 copies of FliG arrayed circumferentially around the rotor.

In Figure 3.1.2b we show the modeled driving potentials sensed by the rotor when stator changes its conformation. The driving potentials (free energies) of the stator are approximated by identical piecewise linear functions offset by half a wavelength $2\pi/26$ (parameters used to construct the saw-tooth potential are listed in Table1 and Figure 3.1.4.). Each transition between the two potentials initiates a power stroke, which, for simplicity, we model as a constant force. The motion of the rotor is tracked by means of a large load (with drag coefficient ζ_L) attached to the motor via a compliant elastic linkage. The soft elastic coupling between the rotor and the load is indicated by the spring. The sharp peaks in the potential may be due to steric interactions between FliGs and the MotA cytoplasmic loops that prevent thermal fluctuations from taking the system down the backside of the potential. In our model, these peaks ensure tight coupling between rotation and proton flux. Each motor cycle transports two ions from periplasm to cytoplasm, which decreases the free energy of the system by $2e \times pmf$ and advances the rotor by $2\pi/26$. The (shaded) transition regions specify the positions where the transitions between the potentials can take place. Assumptions A-D have all been presented in this model.

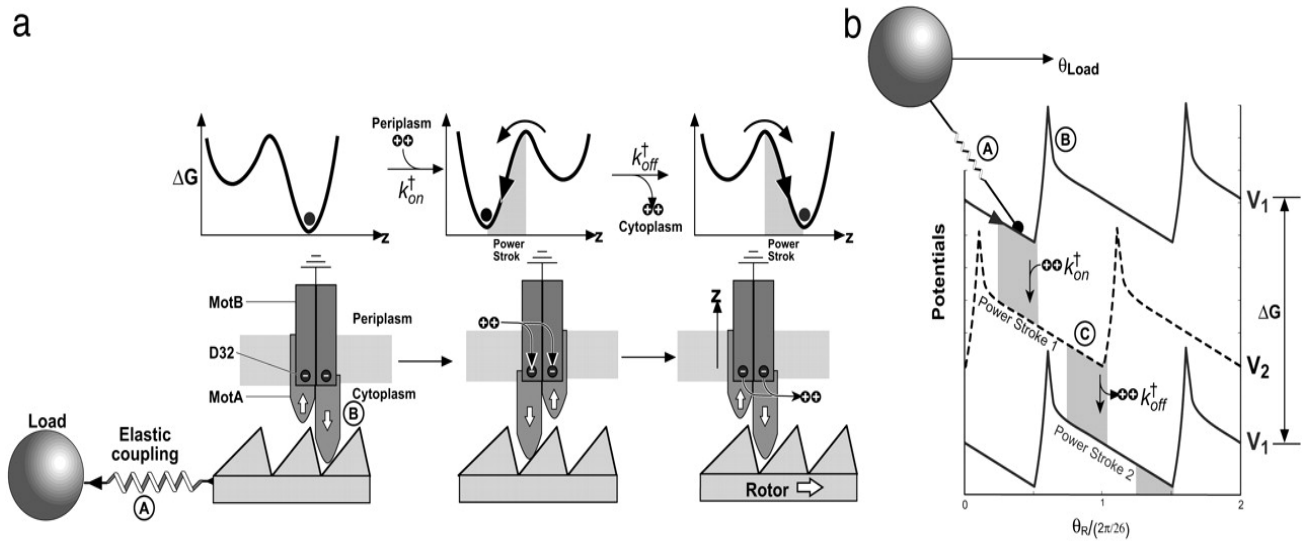

Figure 3.1.2 The rotor–stator interaction according to the model of Blair *et al.* [82]. The stator assembly MotA4/MotB2 is a bistable system: two conformations are separated by an energy barrier. (a) Schematic illustration of one motor cycle. (b) The driving potentials (free energies) of the stator corresponding to (a) are approximated by identical piecewise linear functions offset by half a wavelength $2\pi/26$. The soft elastic coupling between the rotor and the load is indicated by the spring, A. The sharp peaks in the potential labelled B ensure tight coupling between rotation and proton flux. The (shaded) transition regions C specify the positions where the transitions between the potentials can take place.

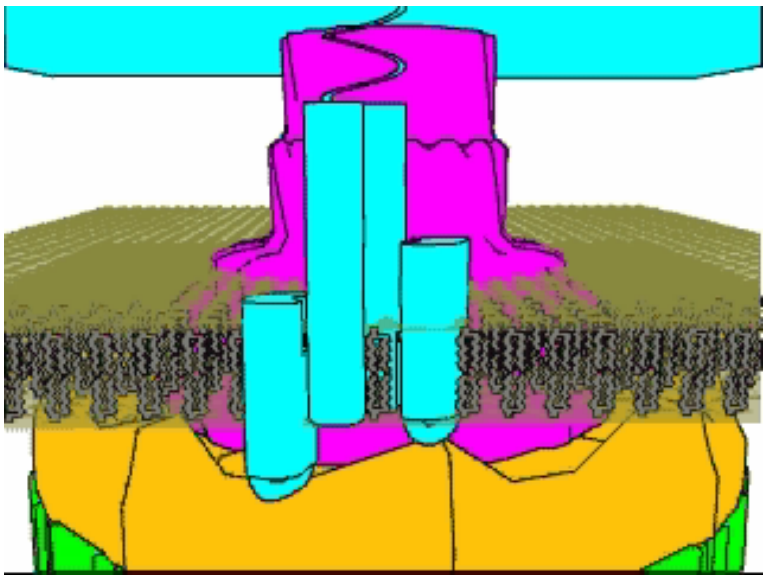

Figure 3.1.3 A 3 D view of the stator-rotor interaction mechanism proposed by our model.

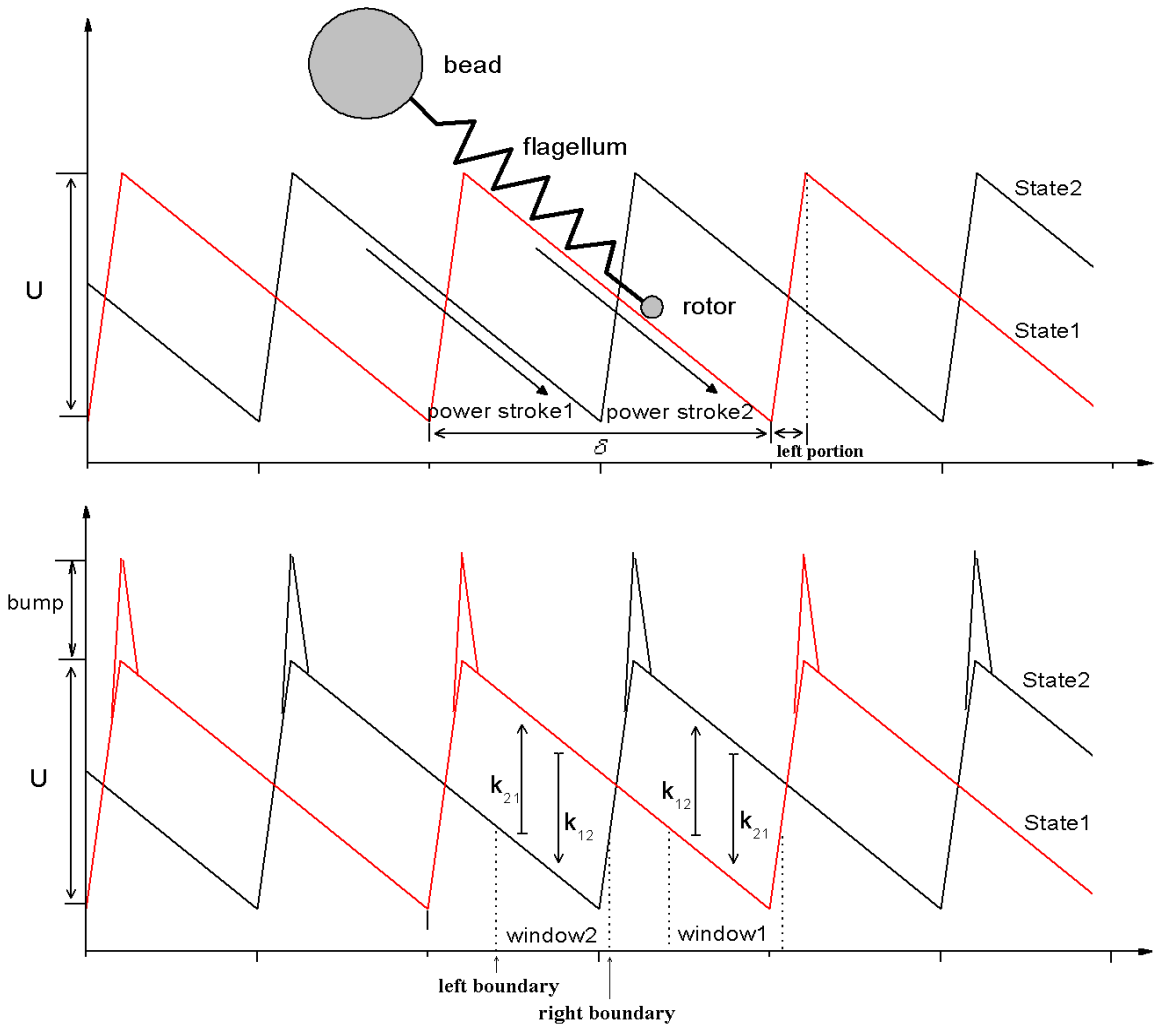

Figure 3.1.4 Schematic plot shows how the model driving potential is constructed from parameters listed in Table 1.

In our model, the choice of a saw-tooth potential is mainly to capture the 'power stroke' feature of the rotor-stator interaction [51]. However, the parameters that we used are not all determined by experiments. They are reasonable estimates of the actual interaction energy profile (we made these estimates based on the typical value of inter-protein interaction energy at this length scale and previous modeling experiences of molecular motors [31-33][50]). θ_α and θ_β specify the boundaries of two localized windows for chemical transitions. This localization arises because the ion channels open only when the conformational change in the stator complex pushes the rotor to a certain relative position. We let the transition window centre on the local

minimum of the saw-tooth potential to achieve maximum length of the power stroke. These parameters can be justified and further tuned when structural information of the motor's key components becomes available.

Table 1. Parameters used in the model calculations.

Quantity		Value	Comments
Potential periodicity, δ		$2\pi/26$	Reference [58]
Rotor drag coefficient, ζ_M		2×10^{-3} pN•nm•s/rad^2	Estimated
Bead drag coefficient, ζ_L		0.01–200 pN•nm•s/rad^2	Calculated from Stokes' Law
Linkage spring constant, κ		150-500 pN•nm/rad^2	Estimated from experimental measurements [77]
Saw-tooth potential height, U		10 k_BT	Fixed parameters of the model
Ratio of the two potential branches, L_{left} / L_{right}		1/9	
Potential bumps	Height	15 k_BT	
	Width	0.2 δ	
	Centers	0.1 δ (State1) 0.6 δ (State 2)	
Transition windows	θ_α,	0.3δ, 0. 8δ	
	θ_β	0. 58δ, (0.58+0.5)δ	Free parameters of the model.
	k_0	0.9×10^5 s^{-1} (T=22.7 °C) 0.5×10^5 s^{-1} (T=17.7 °C) 0.45×10^5 s^{-1} (T=15.8 °C)	Fitting data.

3.2 CALCULATION DETAILS

The physical model we proposed in the previous section is a two state Markov-Fokker-Planck model. We can translate it into a mathematical model following the procedure we introduced in Chapter 2. The dynamics of a single stator motor pulling a viscous load by means of an elastic linkage can be described by the following Langevin equation:

$$\textbf{Motor:}\quad \underbrace{\zeta_{\mathrm{M}}\frac{d\theta}{dt}}_{\substack{\text{effective viscous}\\ \text{drag torque}}} = -\underbrace{\frac{\partial}{\partial\theta}V_{\mathrm{M}}(\theta, s)}_{\substack{\text{Potential of mean force}\\ \text{between rotor and stator}}} - \underbrace{\kappa(\theta-\theta_{\mathrm{L}})}_{\substack{\text{Elastic coupling force}\\ \text{between rotor and load}}} + \underbrace{\sqrt{2k_{\mathrm{B}}T\zeta_{\mathrm{M}}}f_{\mathrm{M}}(t)}_{\text{Brownian torque}},$$

formula (3.1)

where ζ_M is the effective drag coefficient of the rotor. The viscous load (e.g., the bead in Figure 3.1.2 b) is coupled to the rotor via an elastic linkage, which is modeled by a harmonic potential, $V_{RL} = 1/2\kappa(\theta-\theta_L)^2$, where θ_L is the angular position of the load with respect to the rotor. The last term is the stochastic Brownian force acting on the rotor, where $f_M(t)$ is uncorrelated white noise. V_M is the potential of mean force along the minimum energy path re-expressed as a function of the rotation angle θ, and s is a binary variable referring to the stator conformational state: right or left piston down. The slope of V_M determines the force profile the stator exerts on the rotor. This potential has not yet been measured, and so for simplicity we choose the two potentials V_M as identical periodic free-energy profiles, each offset by a half-period, as shown in Figure 3.1.2 b (parameters used to construct the saw-tooth potential are listed in Table1 and Figure 3.1.4). The features of the potentials implement the requirements labelled A, B, and C in the cartoon. The high peak at the top of each potential ensures tight coupling between the rotor and stator by preventing a thermal

fluctuation from carrying the system to the left and "wasting" a translocated proton. Structurally, this type of interaction is likely due to steric or electrostatic repulsion between an engaged (half) stator and the FliG proteins of the rotor. The switching between the two stator chemical states corresponds to switching between the two potential curves shown in Figure 3.1.2 b, which can be described by a Kramers jump process between the two stator potential minima.

Simultaneously, the motion of the load is described by the Langevin equation:

$$\textbf{Load:}\quad \underbrace{\zeta_{\mathrm{L}}\frac{d\theta_{\mathrm{L}}}{dt}}_{\substack{\text{Viscous drag}\\ \text{force on the Load}}} = \underbrace{\kappa(\theta-\theta_{\mathrm{L}})}_{\substack{\text{Elastic coupling}\\ \text{force}}} + \underbrace{\sqrt{2k_{\mathrm{B}}T\zeta_{\mathrm{L}}}f_{\mathrm{L}}(t)}_{\substack{\text{Brownian force}\\ \text{on the load}}}.$$

formula (3.2)

Here the elastic coupling term appears with a sign opposite to that in formula (3.1), and ζ_L is the drag coefficient of the load. The last term is the Brownian force on the load. The characteristic time scale for the motion of the load is $t_L = \zeta_L / \kappa$.

The above formula (3.1) and (3.2) can be replaced by the equivalent coupled Markov–Fokker–Planck equations describing the probability density, $\rho_j(\theta_L, \theta, t)$ of the rotor and load being at position (θ_L, θ) at time t in chemical state j when driven by a single stator:

$$\frac{\partial\rho_j}{\partial t} = \frac{1}{D_{\mathrm{M}}}\frac{\partial}{\partial\theta}\left(\frac{1}{k_{\mathrm{B}}T}\left(\kappa(\theta_{\mathrm{L}}-\theta_{\mathrm{M}})+\frac{\partial}{\partial\theta}V_j\right)\rho_j\right)$$
$$\underbrace{+\frac{1}{D_{\mathrm{L}}}\frac{\partial}{\partial\theta}\left(\frac{1}{k_{\mathrm{B}}T}\kappa(\theta_{\mathrm{M}}-\theta_{\mathrm{L}})\rho_j\right)}_{\substack{\text{Motion due to the potential}\\ \text{and the load force}}} \underbrace{+D_{\mathrm{M}}\frac{\partial^2\rho_j}{\partial\theta_{\mathrm{M}}^2}+D_{\mathrm{L}}\frac{\partial^2\rho_j}{\partial\theta_{\mathrm{L}}^2}}_{\text{Brownian motion}}$$
$$\underbrace{+\sum_i k_{ji}(\theta)\rho_i}_{\substack{\text{Chemical}\\ \text{transitions}}}, \quad i, j = 1, 2.$$

formula (3.3)

Here D_M and D_L are the diffusion constants of the rotor and the bead, respectively, related to the drag coefficients by the Einstein relation, $\zeta = k_B T / D$.

Assumption D is implemented by the potentials in Figure 3.1.2 b by ensuring that chemical transitions between chemical states are localized to a band near the potential minima (shaded in Figure 3.1.2 b). Localizing the stator transitions implies that there is a timing mechanism that depends on a rotor–stator interaction so that the power strokes are delivered to the rotor near the optimal angular rotor position. Blair *et al.* [82] ascribe this property to a charge–charge pairing between the MotA cytoplasmic loop and the α-helix of FliG. Within this band, the most probable location where transitions take place varies with the rotor speed. This variation is because the effective transition rate is given by weighting the transition rate at each angle, θ, by the probability of being at that position

$$\langle k \rangle \approx \int k(\theta)\rho(\theta,\theta_L)d\theta_L d\theta \qquad \text{formula (3.4)}$$

Because of the elastic coupling to the load, the potentials in Figure 3.1.2 b will be sheared, skewing the probability density, ρ, and thus the most probable transition locus.

To ensure that the transitions obey detailed balance, the transition rate between potentials are modeled by

$$k_{12}(\theta) = k_0 \exp(\lambda \Delta G_{12}(\theta)/k_B T),$$

$$k_{21}(\theta) = k_0 \exp((\lambda - 1)\Delta G_{12}(\theta)/k_B T) \qquad \text{formula (3.5)}$$

where

$$\Delta G_{12}(\theta) = U_1(\theta) - U_2(\theta) + pmf \qquad \text{formula (3.6)}$$

In formula (3.5) λ apportions the free-energy difference between forward and reverse rates; in our computations we set λ = 0.5. Note that in diagrams like Figure

3.1.2 b, the derivatives of the driving potentials specify the instantaneous torque generated at the rotor–stator interface: $\tau(\theta) = -\partial V / \partial \theta$ and the vertical distances between the potentials in the transition region is the thermodynamic contribution from the proton-motive force. In a full motor cycle, the motor consumes the free energy of two protons $2e \times pmf$. In our model, we chose to use half of the energy for each transition, making each transition use the energy of one proton.

In a full torque generation cycle, the system will go through

state1 (proton unbound, empty state)→ state2 (proton bound, occupied state)→ state1 (proton released, empty state)

the individual binding/unbinding rates are modeled as a function of position θ:

periplasm on rate

$$k_{perion}(\theta) = k_0 f(\theta) \exp(0.5(U_1(\theta) - U_2(\theta) + pmf) / k_B T) \qquad \text{formula (3.7)}$$

periplasm off rate

$$k_{perioff}(\theta) = k_0 f(\theta) \exp(-0.5(U_1(\theta) - U_2(\theta) + pmf) / k_B T) \qquad \text{formula (3.8)}$$

cytoplasm off rate

$$k_{cytooff}(\theta) = k_0 f(\theta) \exp(0.5(U_2(\theta) - U_1(\theta) + pmf) / k_B T) \qquad \text{formula (3.9)}$$

cytoplasm on rate

$$k_{cytoon}(\theta) = k_0 f(\theta) \exp(-0.5(U_2(\theta) - U_1(\theta) + pmf) / k_B T) \qquad \text{formula (3.10)}$$

where k_0 is the binding attempting rate constant, a free parameter of our model and $f(\theta)$ is the transition window gating function accounting for the requirement that chemical transitions and the rotor position are coupled. Here we use a triangle shape

$$f(\theta_\alpha,\theta_\beta)=\begin{cases}\dfrac{\theta-\theta_\alpha}{\frac{1}{2}(\theta_\beta-\theta_\alpha)}, \text{ for } \theta_\alpha<\theta<\dfrac{1}{2}(\theta_\alpha+\theta_\beta)\\ 1-\dfrac{\theta-\frac{1}{2}(\theta_\alpha+\theta_\beta)}{\frac{1}{2}(\theta_\beta-\theta_\alpha)}, \text{ for } \dfrac{1}{2}(\theta_\alpha+\theta_\beta)<\theta<\theta_\beta,\\ 0, \text{ otherwise}\end{cases} \qquad \text{formula (3.11)}$$

$\theta_\alpha,\theta_\beta$ are the two boundaries of the transition window.

The above two-state Markov-Fokker-Planck model can be solved by the methods we introduced in Chapter 2. However, when there are N stators acting in parallel (Figure 3.2.1) in the system, the mathematical representation becomes much more complicated. The torque now applied to the rotor will be a sum of the driving potential induced by individual stator at different position and with different ion binding status. Since the potentials we used are $2\pi/26$ periodic, we can project all the stator positions into one period $\delta=2\pi/26$. The projection allows us to visualize the relative relations of these stator positions. In our model we assume the N stators are randomly distributed in $\delta=2\pi/26$ (however, we have also tried equally distributed stator positions and this distribution does not greatly influence the ability of our model to fit the data). Due to the distance between stators, the driving potential sensed by the rotor now is a combination of the positions that are separated by a relative phase $\Delta\theta_i/\delta, i=1...N$.

Unless stated otherwise, all of the results shown in this chapter are computed with N = 8 (the classically agreed stator number).

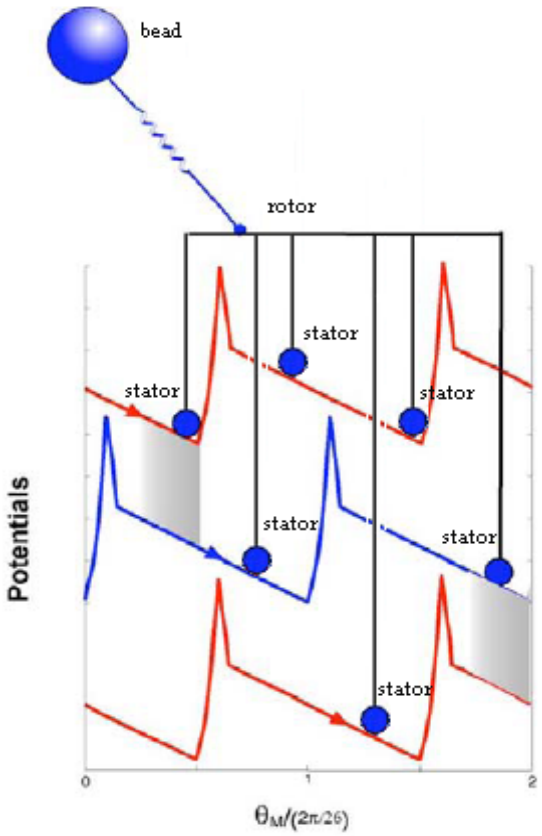

Figure 3.2.1 A cartoon plot shows how the motor works with multiple stators in the system.

The complete two-state Markov-Fokker-Planck model with N stators is solved by the Langevin simulation approach. The simulation code (in FORTRAN language) is attached in the APPENDIX. In this code we implemented parallel Monte Carlo processes, to simulate the motion of the rotor and the bead driven by model potentials and the ion hopping on/off in each stator.

Results shown in next section are all obtained from the Langevin simulation approach. Uncertainty of the exact values of the rotor and stator diffusion constants does not affect our ability to fit the motor torque–speed relations, which are mainly determined by the much slower load diffusion constant and effective chemical transition rates.

3.3 MODEL RESULTS

3.3.1 Low-Speed Plateau of the Torque-Speed Relationship

Analysis and simulations of the model equations show that, for a motor dragging a large load with a compliant elastic linkage, there exists a time-scale separation between the motor and the load dynamics: $t_M << t_L$. In rotation experiments, viscous loads are attached to the flagellar motor via the hook, which is soft enough to allow the rotor to fluctuate over several step lengths before the load moves appreciably. Distending the soft elastic linkage effectively converts the viscous load into a conservative load on the motor. That is, the work done to stretch the linkage can be returned to the motor before it is dissipated by the viscous load. The Stokes and thermodynamic efficiencies are defined as the ratios of the power dissipated by a viscous load (Stokes) or the rate of work done against a conservative load (thermodynamic), respectively, to the power consumed by the motor. The separation of time scales between the flagellar motor and the load renders the Stokes efficiency nearly equivalent to a thermodynamic efficiency. Thermodynamics dictates that 100% thermodynamic efficiency is approached as the system evolves "infinitesimally" slowly (i.e., reversibly). This requirement is satisfied with a large bead and a soft linkage even at rotation speeds of several hundred Hz, because the bead motion is still much slower than the motor internal dynamics. Furthermore, the soft hook and time-scale separation ensure that the load does not see the details of the free-energy potentials shown in Figure 3.1.2 b, but a nearly smooth effective potential. Thus, the measured Stokes efficiency also will be ≈100%, implying that the torque appears nearly constant. This region is the operating regime in the plateau of the flagellar motor torque–speed curve, in which the following approximation holds:

$$\zeta_L \omega_L \approx \Delta G / \delta = (\Delta H - T\Delta S) / \delta \qquad \text{formula (3.12)}$$

where ω_L is the angular velocity of the load, $\delta = 2\pi/26$ is the angular step length (i.e., distance between FliGs), and ΔG is the free-energy drop per motor cycle.

3.3.2 The Motor Torque–Speed Curve Drops Sharply at High Speed

As the viscous load (e.g., a bead or the cell body) decreases, the tension between the load and the motor relaxes faster, and so the motor works against a smaller elastic load. An elastic load "shears" the potentials toward the left in Figure 3.1.2 b and this shear decreases along with the load. Reduced load shifts the probability density distributions right toward the potential minimum, where the stator contributes zero, or even negative, torque. The average torque between the motor and the load (i.e., the motor torque) is determined by the potential gradients weighted by the probability density; therefore, the apparent motor torque decreases as the load decreases. However, this dependence only guarantees a concave-down torque–speed curve, but the sharpness is not so well controlled. The experimentally observed non-linear shape of the torque–speed curve in the transition region sets a loose constraint on the relation between the potential shapes and the chemical rates $k(\theta)$. The model system presented in this work is only one of the many possible realizations.

In our model we choose $k(\theta)$ to be localized around the potential minima of each potential curve (see Figure 3.1.4). This localization arises because the ion channels open only at certain relative positions between the rotor and the stator. We propose the sharp transition in the torque–speed curve arises because of a positive feedback mechanism that can be explained through interplay between localized transitions along θ and stator mutual interference. To make a transition from one potential curve to another one (corresponding to ion hopping on and off within one stator), the rotor needs to rotate into the transition window. However, other stators may push the rotator to move out of the transition window before the chemical

transition takes place. Consequently, the rotor is trapped before thermal fluctuations bring it back into the transition window so the stator can switch its chemical state. A load reduces occurrence of the trap by pulling the rotor backward. Therefore decreasing the load shortens the bead response time, and lengthens the motor internal dynamics at the same time. This results in abrupt change of the system from the thermodynamics-controlled plateau region (with time-scale separation between the bead response time and the motor internal kinetics) to the kinetics-controlled knee region (with no time-scale separation between them).

Below, we show the model can well reproduce the experimental results. The model should be viewed as a framework for studying the BFM, which can be further elaborated as new experimental inputs become available.

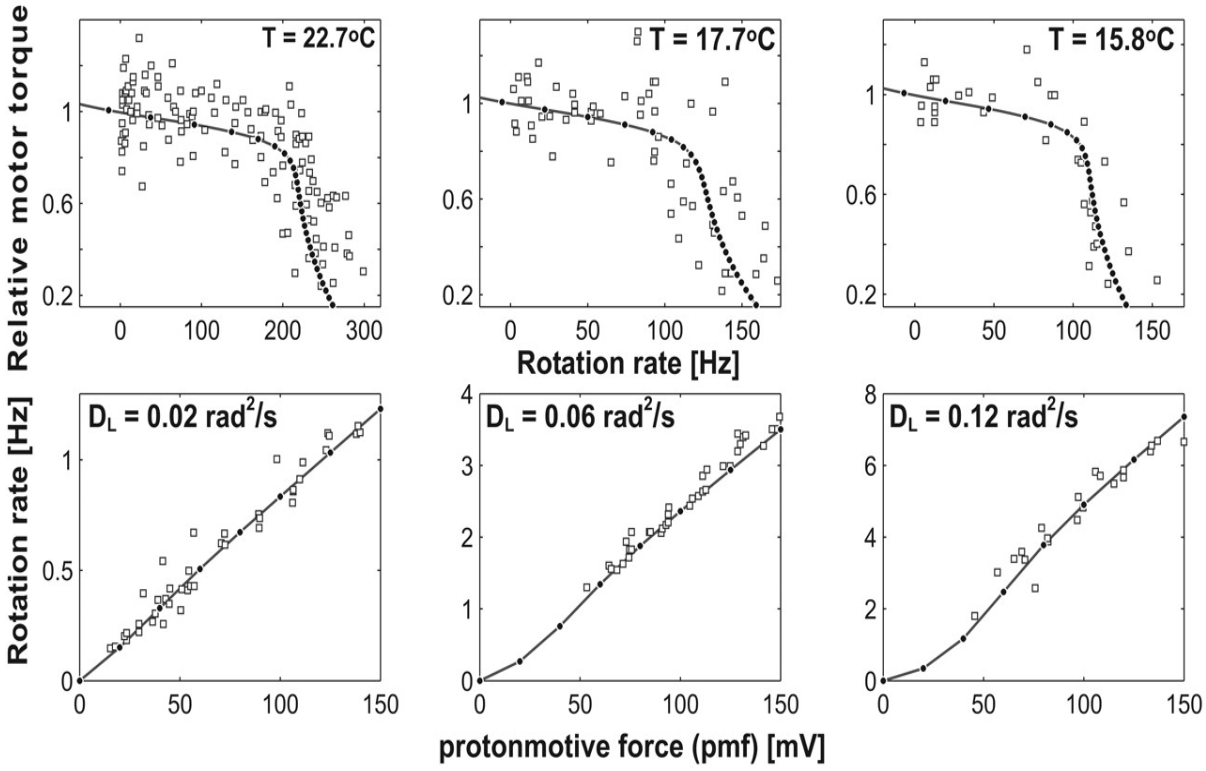

Figure 3.3.1 Comparison of model calculations and experimental data. (Upper) Experimental torque-speed curves at different temperatures (squares) (data from reference [45]). The filled dots are calculated from the model. (Lower) The linear dependence of the motor rotation speed with pmf at three different high loads. The experimental data (squares) are taken from Fung and Berg [75]. The calculated results are shown as filled dots.

3.4 CONCLUSION

In this chapter, we have demonstrated that the motor speed of the BFM as a function of motor torque and pmf indicates some general physical features of the system. We have constructed a Markov-Fokker-Planck model of the BFM based on the qualitative proposal by Blair and coworkers that incorporates four generic assumptions. Although simply constructed, we show our model is consistent with a large body of experimental observations on the BFM and have explicitly explained the physics underneath the torque-speed relationship of the BFM.

A central aspect of the mechanochemical measurements summarized in Figure 3.3.1 is that they are performed by observing the motor through the filter of an elastic compliance coupled to a viscous load. Elston *et al.* [83-84] have given a detailed mathematical analysis of the role of a soft elastic linkage and time-scale separation on motor performance. A similar situation holds for other mechanochemical systems. For example, the F_1 motor of the F_1F_0 ATPase achieves ≈100% Stokes efficiency when loaded with a long elastic actin filament and exposed to high ATP concentrations. In this situation, the motor dynamics are not rate limiting. However, when the ATP concentration drops, slowing the motor dynamics, the Stokes efficiency drops as well [29][85]. Another example is the motor that drives the gliding motility of the mollicute Mycoplasma mobile. This bacterium can move forward at an amazing speed of several cell-body lengths per second. By attaching to the bacterium a large bead, Miyata *et al.* [86] observed that the velocity increased linearly with temperature, exactly what one would expect when the motor is observed through the filter of an elastic compliance (the cell body) attached to a large viscous load.

Another notable feature of our model is the explanation it offers for the sharp transition between the two regimes of the torque–speed curve in terms of positive

feedback between the external load and the angle-dependent transition rates between the stator kinetic states.

CHAPTER 4

Model Studies on the Dynamics of the Bacterial Flagellar Motor

Recent experiments that directly observe steps shed light on the fundamental working mechanism of the BFM and evoke a new generation of models. In the previous chapter, we have explained the general physics underneath the torque-speed curve with a simple two-states model. Here we continue our exploration of this model. With a more realistic formalism of ion jumping rate, we reproduced the latest experimental results of rotation dependence on ion concentration and stepping dynamics. We also showed that the same model can explain the behaviour of the Na^+ driven chimera motor. Inspired by the method used to detect chimera motor stepping, the model predicts the conditions under which wild-type H^+ *E. coli* BFM stepping can be observed and the corresponding stepping statistics. The model makes further predictions that can be tested by experiments.

This chapter is mainly reformed from the paper we are going to publish:

Bai, F., Lo, C., Berry, R.M. and Xing, J. Model studies on the dynamics of the bacterial flagellar motor.

Here I acknowledge the contributions from Jianhua Xing, Richard Berry and Chien-Jung Lo.

4.1 SEPARATION OF PMF

The model of Chapter 3 was constructed before direct step measurement, when the torque-speed relationship was the best biophysical probe to study the mechanism. It gives a full picture of the motor's power output under external loads, and gives an indication of the energy conversion efficiency. In the previous chapter, we have intensely studied this torque-speed relationship and we showed the flat plateau and steep concave-down transition are mainly due to rotation being observed through a soft elastic linkage between the motor and the viscous load and the diffusion dynamics of the motor and load being on different time scales. Recent progress in experimental techniques allowed us to observe 26 steps/revolution in a slow rotating chimera motor [58], consistent with the periodicity of the ring of FliG protein. Additionally, the smf (sodium motive force) can now be measured now in the chimera motor with the help of a fluorescent dye [49]. Changes in the membrane potential and ion-gradients show a nonequivalent control of the motor speed. All these new results evoke a revisit of our model. In this chapter, we improve the model with a more realistic formulation of the transition rate between potentials and compare it with the latest experiments.

In the Chapter 3, we modeled the jumping rate between potentials as

$k_{12} = k_0 \exp(\lambda \Delta G_{12} / k_B T)$,

$k_{21} = k_0 \exp((\lambda - 1)\Delta G_{12} / k_B T)$ formula (3.5)

where $\Delta G_{12} = U_1 - U_2 + pmf$ to satisfy detailed balance.

Although this formulation has correctly modeled how pmf assists forward transitions, to use it as a single energy term instead of the sum of ion gradients and membrane voltage is thermodynamically unrealistic. This formulation is also unsatisfactory because we cannot test the motor response to individual changes in ion

gradient or membrane voltage. However, in most experiments it is easier to change ion concentration or membrane voltage alone rather than controlling the whole. Therefore, any model trying to explain the working mechanism of the BFM needs to predict how ion concentration and membrane voltage influence motor speed. The first improvement we make here is to model the jumping rate as an explicit function of external and internal ion concentrations, and membrane voltage.

For the jump rates between the bulk ion concentration on the periplasmic side (C_{peri}) and a stator binding site we specify:

$$k_{perion}(\theta) = (C_{peri})^2 k_0 f(\theta) \exp(0.5(U_1 - U_2 + V_{mem})/k_B T) \qquad \text{formula (4.1)}$$

$$k_{perioff}(\theta) = 10^{(-2pK_a)} k_0 f(\theta) \exp(-0.5(U_1 - U_2 + V_{mem})/k_B T) \qquad \text{formula (4.2)}$$

For the jump rates between the bulk ion concentration on the cytoplasmic side (C_{cyto}) and a stator binding site we specify:

$$k_{cytooff}(\theta) = 10^{(-2pK_a)} k_0 f(\theta) \exp(0.5(U_2 - U_1 + V_{mem})/k_B T) \qquad \text{formula (4.3)}$$

$$k_{cytoon}(\theta) = (C_{cyto})^2 k_0 f(\theta) \exp(-0.5(U_2 - U_1 + V_{mem})/k_B T) \qquad \text{formula (4.4)}$$

In this new formulation, while detailed balance still holds, we successfully separate the contributions from the membrane potential and the ion concentration difference in the pmf (smf). (Notice, in our model we assume two ions bind cooperatively in one torque generation cycle. Hence we take the square of C_{cyto} C_{peri} and the binding site pK_a value. A model implementing sequential binding of ions is in consideration.)

First we show that the *E. coli* BFM torque-speed curve can be reproduced with this new jumping rate formulation (Figure 4.1.1 a). At normal living conditions, the *E. coli* BFM works with intracellular pH 7.6, external pH 7 and membrane potential 120mV. Without modifying the flashing energy profile, the *E. coli* BFM torque speed

curve can be easily reproduced by inputting these realistic values into our new formulation (Table 2).

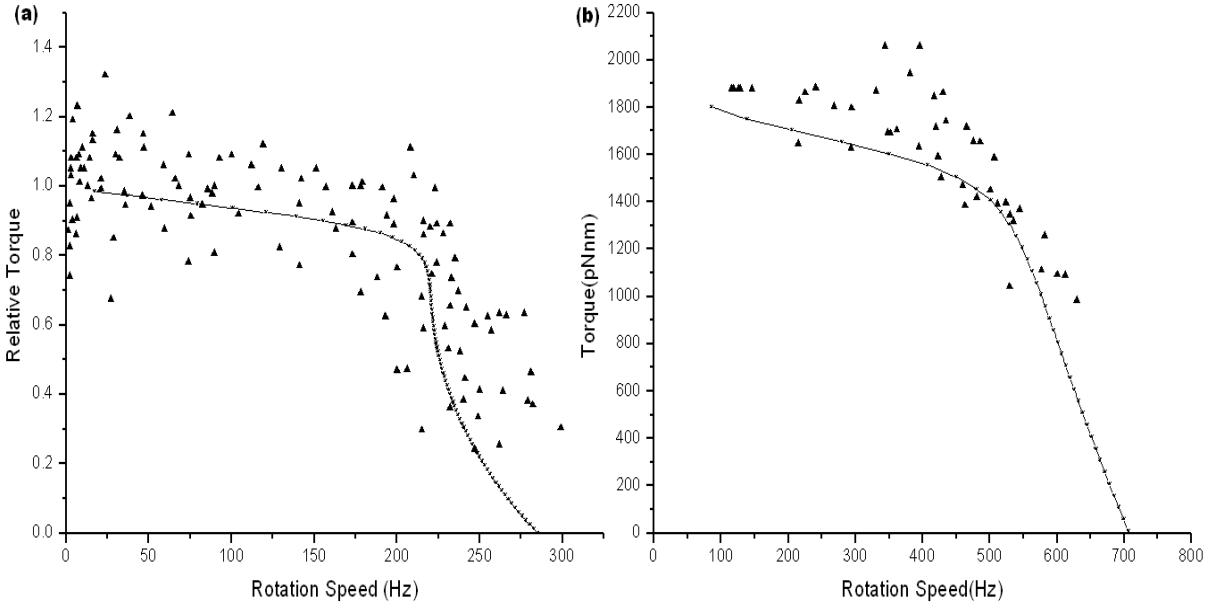

Figure 4.1.1 Model predicted torque-speed curves of (a) *E. coli* and (b) chimera with experimental data underneath. (experimental data points are from [52] and [87])

The chimera motor, which uses Na^+ type BFM stator and *E. coli* BFM rotor, is a successful product from synthetic biology. Since it is much easier to change Na^+ concentration than pH value in the medium, we gain a more robust control of the energetics in the chimera motor than in the *E. coli* motor. Because of this obvious advantage, the chimera motor has become the favourable target in recent BFM studies. The torque-speed relationship of the chimera motor has been reported by Inoue *et al.*[87]. It is highly similar to that of the *E. coli* BFM except for a higher 'knee' speed and zero-load speed. Without changing the driving potential profile, we substitute the experimental values of chimera motor living condition into our model and fit the chimera torque speed curve (Figure 4.1.1 b).

Table 2

E. coli BFM torque-speed curve fitting parameters (in addition to Table 1)		
Periplasmic ion concentration	$C_{peri}=10^{-7}$ M	from experiments
Cytoplasmic ion concentration	$C_{cyto}=10^{-7.6}$ M	
Membrane voltage	V_m=120 mV	
Stator binding site property	$pK_\alpha = 7.3$	free parameters pK_α is chosen half way between pH_{peri} and pH_{cyto}
Binding rate	k_0= 1.0 $\times 10^{20}$ s^{-1}/M^2	
Chimera BFM torque-speed curve fitting parameters		
Periplasmic ion concentration	C_{peri}=85 mM	from experiments
Cytoplasmic ion concentration	C_{cyto}=12 mM	
Membrane voltage	V_m=140 mV	
Stator binding site property	$pK_\alpha = 1.5$	free parameters pK_α is chosen half way between -($\log C_{peri}$) and -($\log C_{cyto}$)
Binding rate	k_0= 6.0 $\times 10^{7}$ s^{-1}/M^2	

Here we show the torque-speed curves can be reproduced (for both *E .coli* and chimera) with the same model framework. Therefore we conclude that there is no fundamental distinction in the working mechanism between the *E. coli* BFM and the chimera motor, as expected from the similar shapes of the torque-speed curves. We attribute the differences to mainly the binding/unbinding rates of H^+ and Na^+ to the stator, not the stator-rotor interactive potential.

With our new rate formulation, we can now test the motor response to independently varying ion concentration and membrane potential. Figure 4.1.2 shows that the motor speed varies proportionally with membrane voltage over a wide range

(*E. coli* 100mV-140mV, chimera 120mV-160mV). This result is consistent with Berg's experiment [75].

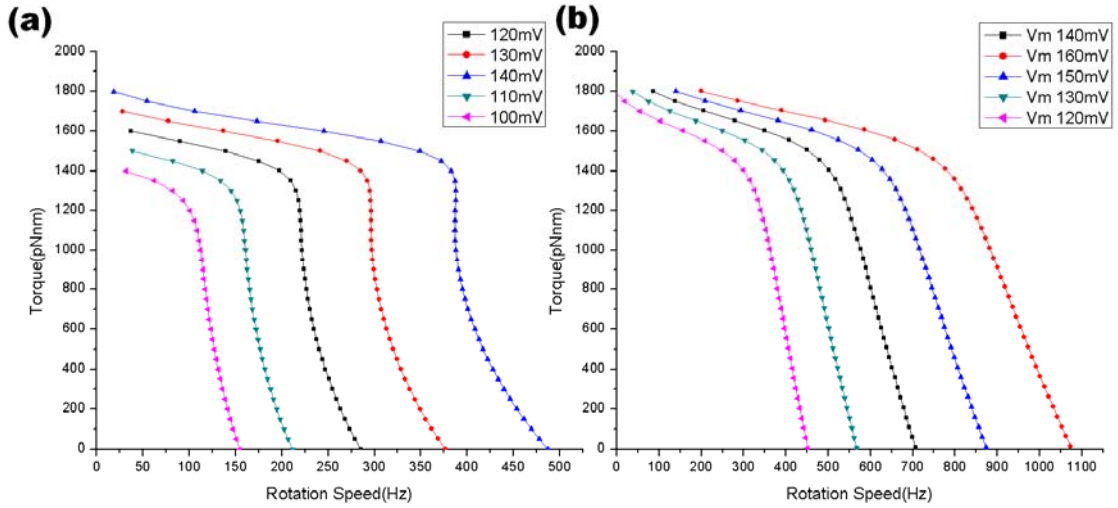

Figure 4.1.2 Model predictions show motor response to membrane potential is proportional over a wide range (a) in the *E. coli* motor (b) in the chimera motor.

However, as shown in Figure 4.1.3, the motor speed response to periplasmic ion concentration is asymmetric. The saturation effect at high ion concentration is very obvious. This is consistent with Sowa's experiment [53]. The underlying physical explanation for this is that at saturating ion concentration the internal conformational change that generates the 'power stroke' becomes the dominant rate-limiting factor. The high ion binding rate can not effectively increase the flashing rate between driving potentials.

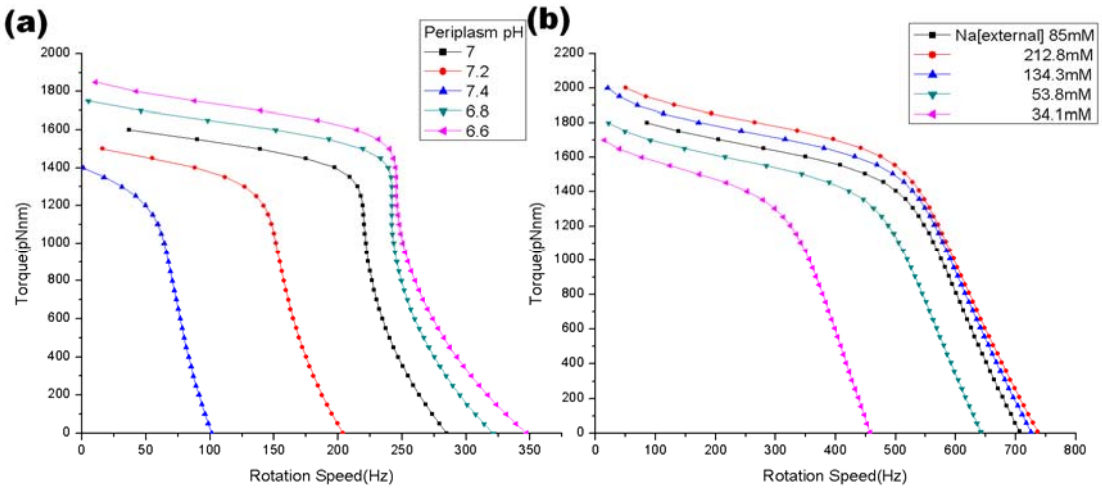

Figure 4.1.3 Model predictions show motor response to periplasmic ion concentration is asymmetric (a) in the *E. coli* motor (b) in the chimera motor.

More interestingly, with our model we can investigate the effect of varying the relative ion concentration and membrane potential contributions while holding the total pmf (smf) constant.

Figure 4.1.4 gives the torque-speed curve under a lower external ion concentration but with a higher membrane potential condition. We see the external ion concentration has a much stronger influence on the motor output. The motor speed decreases dramatically when external ion concentration is lowered despite the total pmf (smf) being compensated by a membrane voltage increase. This is consistent with Lo *et al.*'s recent publication [49].

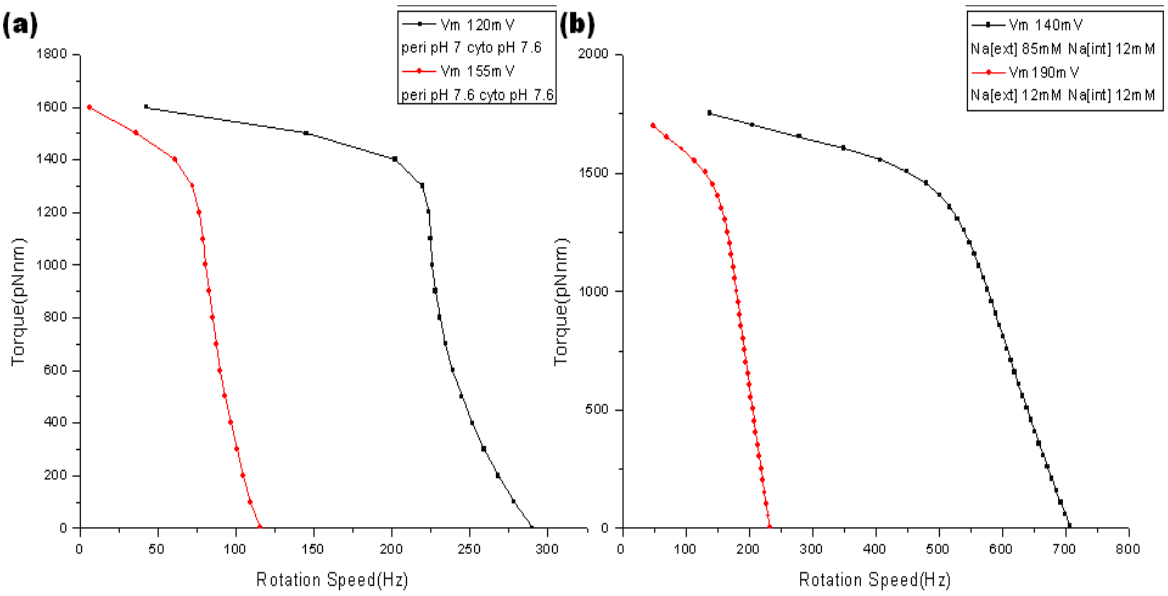

Figure 4.1.4 Model prediction shows motor response to different combinations of membrane potential and ion concentration with the same total pmf (a) in the *E. coli* motor and the same smf (b) in the chimera motor

Our new rate formulation has correctly captured the fact that motor speed does not respond solely to total pmf (smf). It depends more strongly on external ion concentration than membrane voltage. One obvious explanation is that the diffusion limited binding of ions is the rate limiting step in the motor cycle (see reference [49] for a detailed discussion).

4.2 THE MOTOR IS A STEPPER

The efforts devoted to the observation of BFM steps have lasted for more than three decades. In Chapter 1 I reviewed the technical difficulties. Only very recently, Sowa *et al.* managed to resolve steps in a chimera motor. The key requirements to the successful observation of steps are: 1) low induction of stator units (1～2); 2) low external sodium concentration; 3) optical trapping system with high temporal and spatial resolution. Finally, 26 steps per revolution were observed. However, this observation was made when the motor was in a non-stable transient state: stator resurrection and external sodium concentration were not precisely controlled. The

information of the living conditions of these cells was lacking. Here we can use our model to simulate stepping behaviour of the chimera motor and hence we gain an estimate of the environment that these experiments are conducted in.

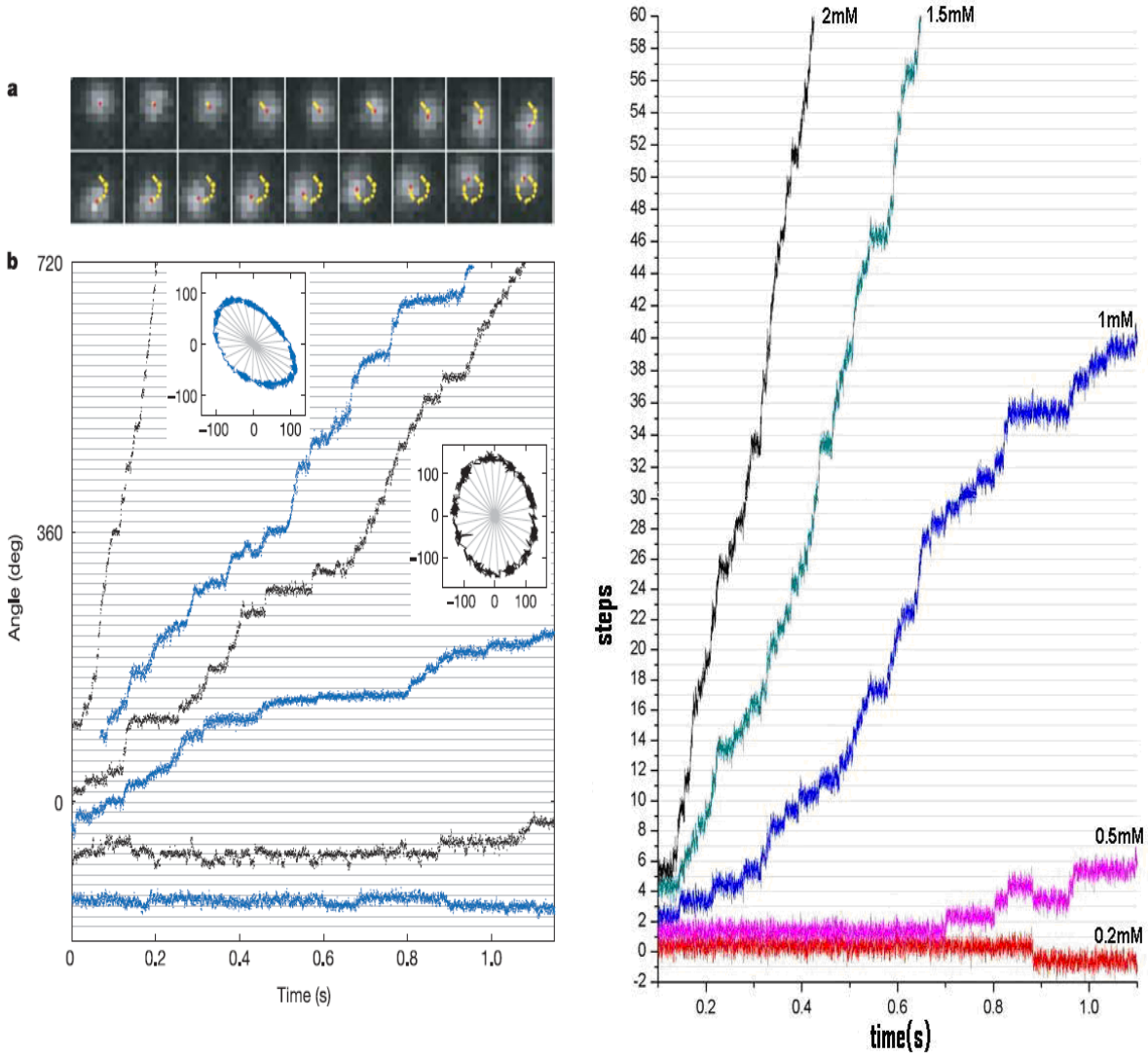

Figure 4.2.1 Steps of chimera stator. (left) experimental data taken at low sodium concentrations (adapted from [58]) (right) trajectories predicted by the model at different external Na^+ concentrations.

Similar to the experimental procedure, in our simulation we assign N_{stator}=1 and lower the external sodium concentration. Langevin simulation (code attached in the APPENDIX) generates motor trajectory under these conditions. Stepping behaviour becomes very obvious when the motor speed is lower than 10Hz. In Figure

4.2.1, we show a series of stepping traces under different external sodium concentrations. By comparing the experimental traces with our simulation, we reach an educated guess of the sodium concentration for these cells. The central three traces running at 0.5 ～2 Hz are from an environment with approximately 0.5～1.5 mM external sodium concentration. If lower than 0.5mM, backwards steps occur frequently and the motor can not make noticeable advancement.

Although steps have been resolved in chimera motors, whether they can be observed in the wild type *E. coli* motor remains unanswered. With our model, we can theoretically explore the conditions under which stepping of the *E. coli* motor could be observed. The speed of the motor decreases rapidly when the external pH value is increased. However, the *E. coli* cells are not able to endure a large pH change since they cannot survive in a strong alkali environment. Therefore, our aim is to find the least demanding condition in which steps could be resolved.

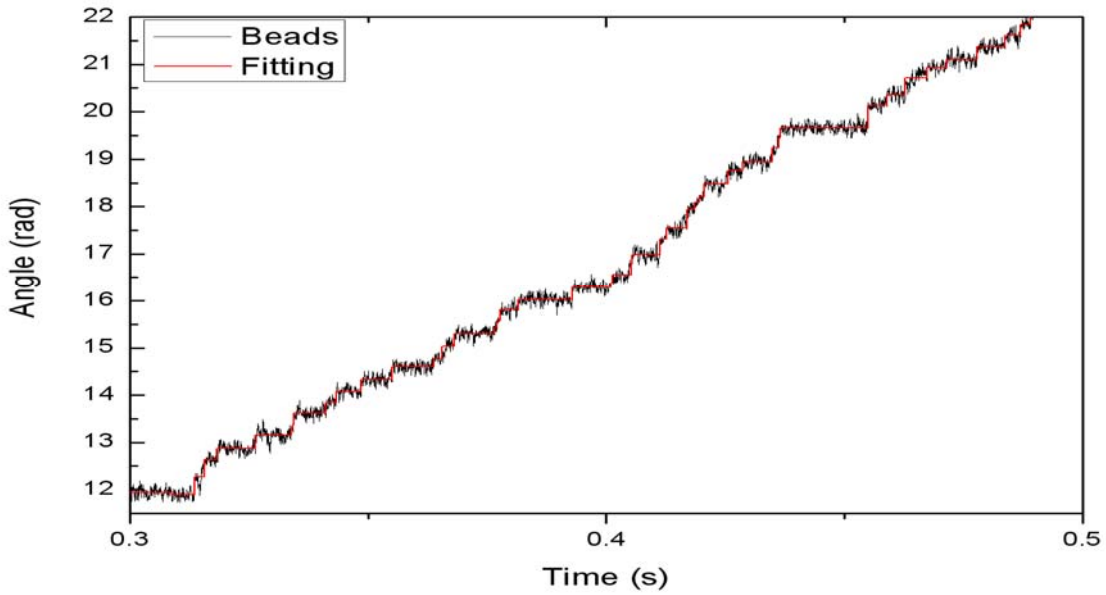

Figure 4.2.2 A selected part of the sample trace (10s long) of the wild type *E. coli* BFM stepping predicted by our two-state model.

In Figure 4.2.2, we simulated the condition of pH_{peri}=8.4, pH_{cyto}=7.6. The motor runs at about 8Hz and steps are easy to detect. With the step finder developed by Lo, the bead traces are filtered, which makes the stepping behaviour more obvious and collection of the corresponding statistics simpler.

The step fitting algorithm is as described in reference [88]. In Figure 4.2.3, we show the step-size distribution of the sample trace shown in Figure 4.2.2 found by the step finder program. In this distribution, we see a clear peak in the centre corresponding to the step size of 26 steps / revolution.

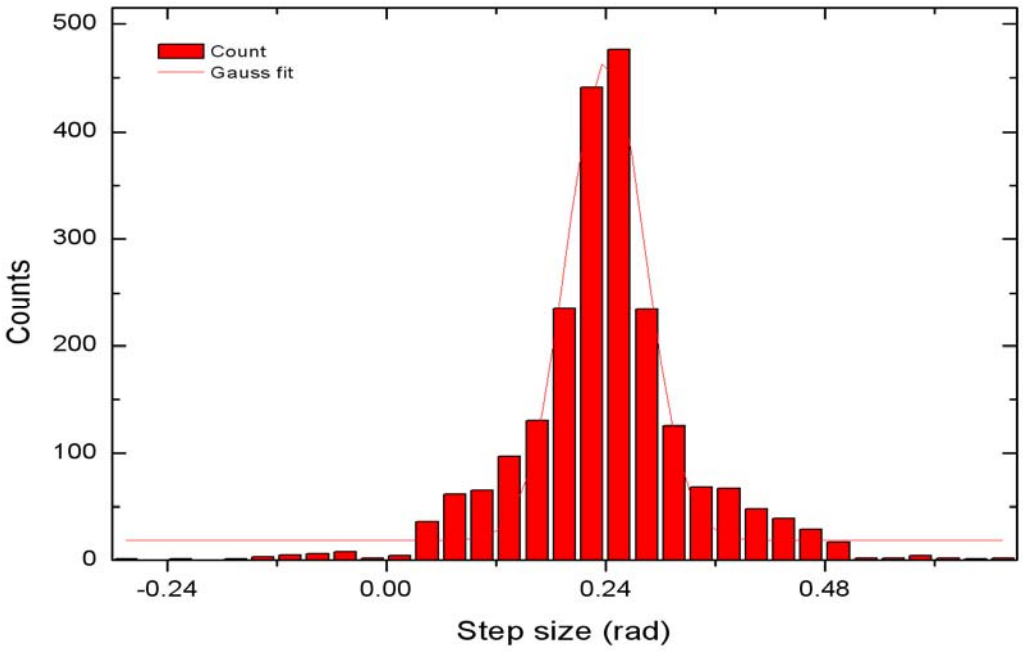

Figure 4.2.3 Step-size distribution of the sample trace (10s long) shown in Figure 4.2.2.

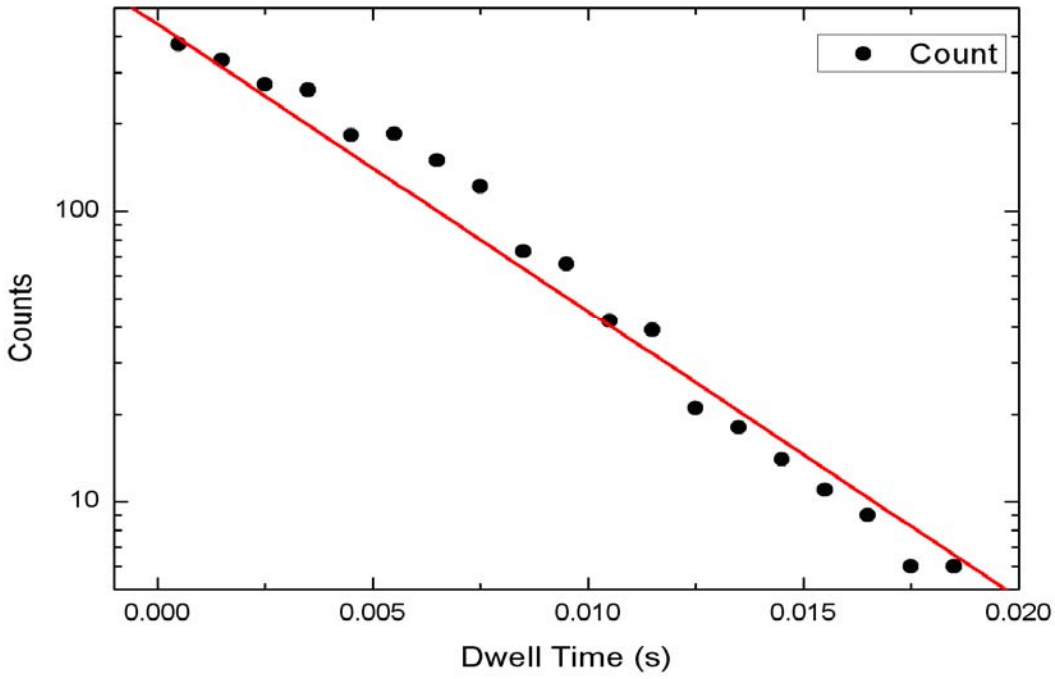

Figure 4.2.4 Dwell time distribution between steps of the sample trace (10s long) shown in Figure 4.2.2

The step finder can also detect the dwelling time between each stepping event and plot their distribution. In Figure 4.2.4, we see a linear relation on a log-linear plot, indicating a single exponential distribution of the dwelling time between steps. The underlying explanation for this distribution is as follows. When we lowered the external ion concentration, the binding rate of ions from the periplasm to the stator was greatly reduced. Compared to other rates, this binding rate becomes the only rate limiting step. The motor has to wait for the ion binding to start a new cycle and the other states in the cycle can be completed at a relatively high speed. Therefore, what we see is a dwelling state in between two fast jumping steps. From the exponential dwelling time distribution we can calculate the mean time between steps. Combining the already known step-size, we know the motor speed. The motor speed calculated

by this method is consistent with the program output that divides the displacement by the simulated time, which confirms the accuracy of our step finding algorithm.

In this section, our model reproduced the chimera motor stepping and predicted the conditions under which the *E. coli* motor stepping can be seen and the corresponding statistics. Inspired by this work, experiments designed to observe wide-type *E. coli* BFM stepping are underway.

4.3 STEP SIZE VS. STATOR NUMBER

According to our model, the BFM is a stepper. For one stator, the current model shows a step size of $2\pi/26$ at low external ion concentration. In this section, we will discuss how the step-size changes when there are multiple stators in the system.

So far there is no experiment designed to directly answer this question. Fluctuation analysis predicted that the step-size will decrease to 1/n of $2\pi/26$ if there are n stators in the system [56]. However, the latest observation of chimera motor steps [58] reported 'the apparent independence of step size on stator number'. Clearly, the studies are contradictory.

Our model can give some insights into the above question. Because the potentials are $2\pi/26$ periodic, we can project all the stator positions into one period $\delta = 2\pi/26$. The projection allows us to visualize the relative relations of these stator positions. We first focus on the situation of 2 stators in the system. Taking the first stator as the reference point, the second stator can come in at any position $\theta \in [0, \delta]$. Since the stators are tightly coupled, the rotor and bead are now powered by two stator units. Figure 4.3.1 is a simple cartoon illustration of how the system works. Due to the distance between two stators, the driving potential sensed by the rotor is a

combination of the two positions that are separated by a relative phase θ / δ.

Here our model makes some interesting predictions:

1. After the second stator resurrects in the system, the observed apparent step size may not be unique and depends on where the second stator recovers. In our model the ion binding step is the only rate limiting step. When there are two stators in the system, the original $2\pi/26$ step will be divided into two substeps.

In Figure 4.3.2, we show a simulation with θ=0.8 δ. The step sizes of the two substeps are 0.2L and 0.8L, respectively.

In Figure 4.3.3, we show a simulation with θ=0.5 δ. The step sizes of the two substeps are half of the original step size.

2. If the stator distribution has certain symmetries, the step size does not necessarily increase with an additional stator. If θ=0 or θ= δ, two stators are synchronized. The system won't move until both of them jump to the 'bound' state and once they move, a displacement of $2\pi/26$ will be finished in one step.

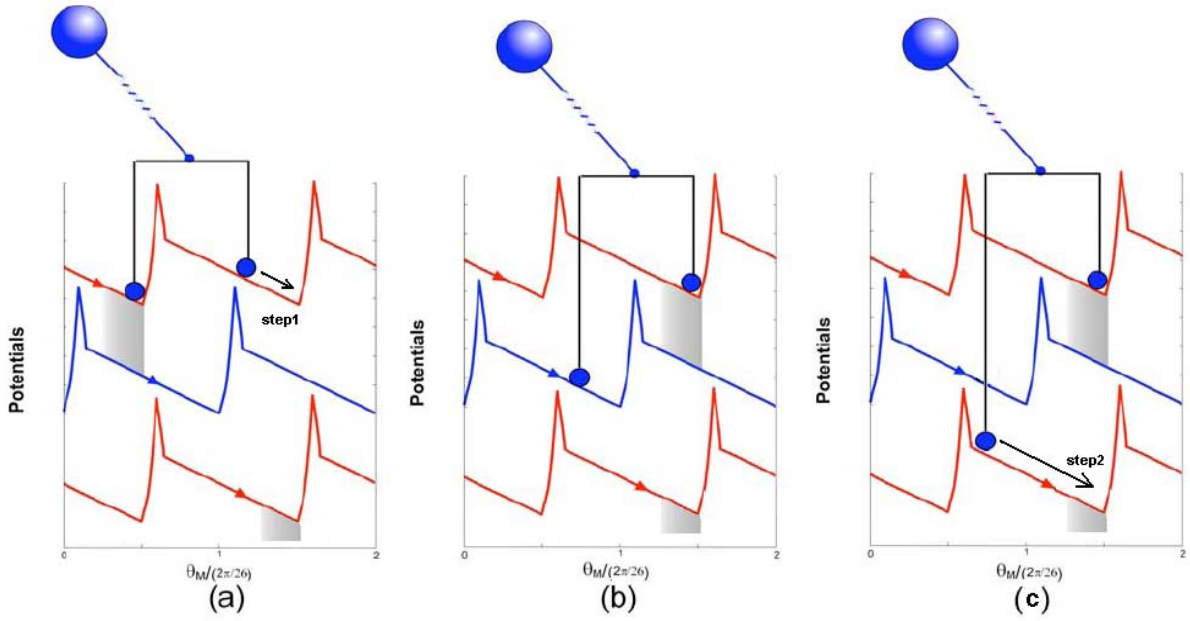

Figure 4.3.1 Cartoon plot shows how two stators power the system.

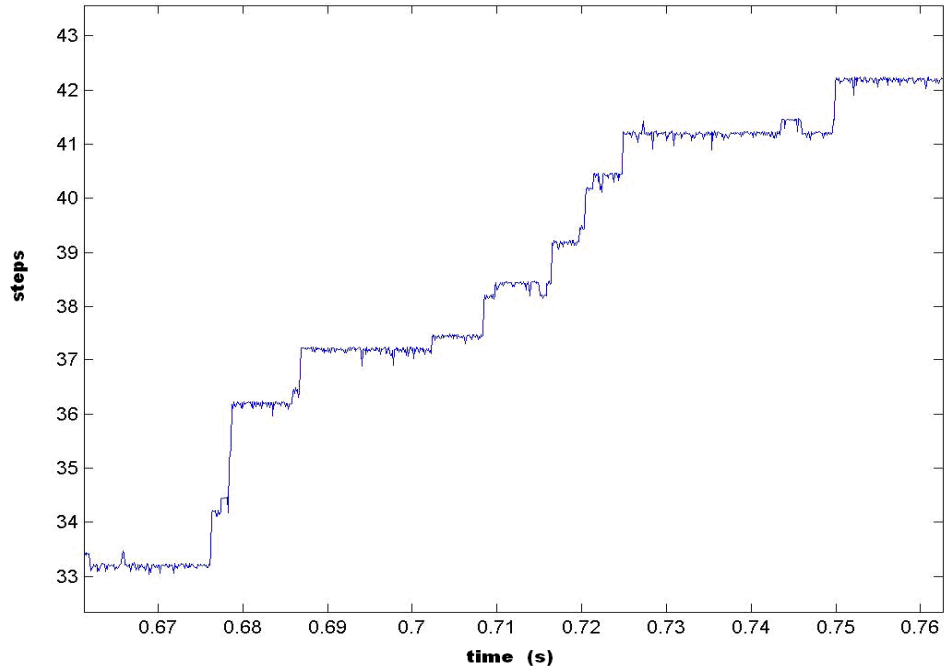

Figure 4.3.2 Substeps predicted by the model when there are two stators in the system separated by 0.8 δ.

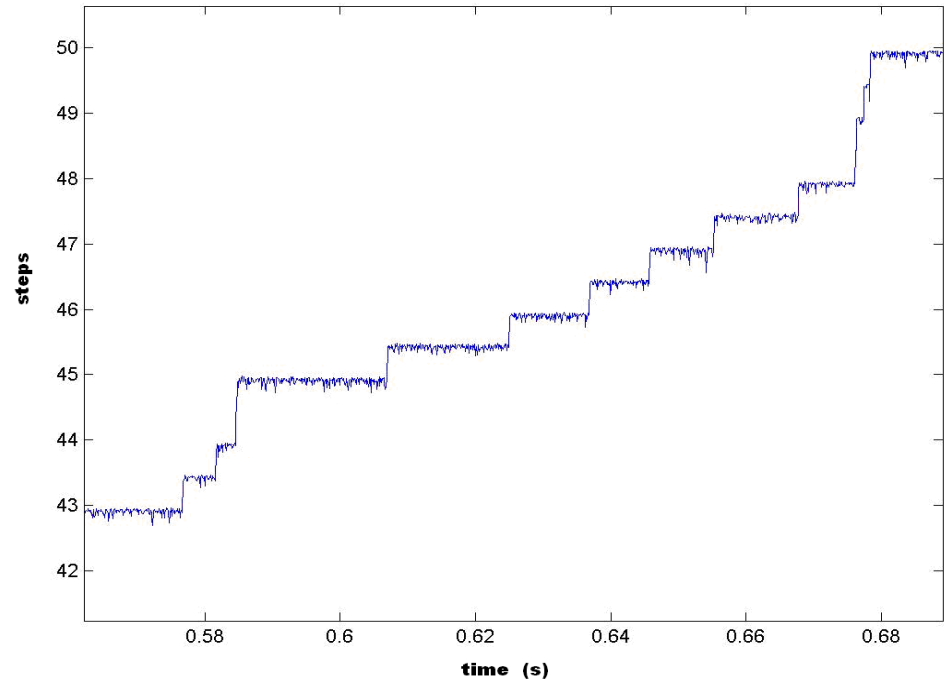

Figure 4.3.3 Substeps predicted by the model when there are two stators in the system separated by 0.5 δ.

Our model provides a possible way to reconcile the result from fluctuation

analysis and Sowa *et al.*'s observation. The theoretical step size obtained from fluctuation analysis may differ from the actual step size observed in experiment. For example, in the special case θ=0 or $\theta = \delta$, the actual angular step size does not change with the additional stator, and two independent rate limiting chemical transitions must take place at the same time for the rotor to advance. This might be the situation observed by Sowa *et al.*. However, fluctuation analysis, which counts the number of statistically independent events, will give a higher stepping count and hence half the step-size.

4.4 TETHER STIFFNESS VS. TORQUE-SPEED CURVE

As we emphasized many times in previous chapters, the BFM motor torque-speed relationship derives from a set of general physical assumptions, among which the soft connection between the rotor and load is crucial. This soft tether allows the rotor and the bead to move on different diffusion time scales and hence produces the flat plateau. In Figure 4.4.1 our model verifies this. The red, blue and green torque-speed curves are the model predictions with 1, 10 and 100 times the original hook stiffness respectively. The destruction of the flat plateau is very obvious. This is another important prediction of our model that can be tested by future experiments if the hook stiffness can be modified by biochemical means.

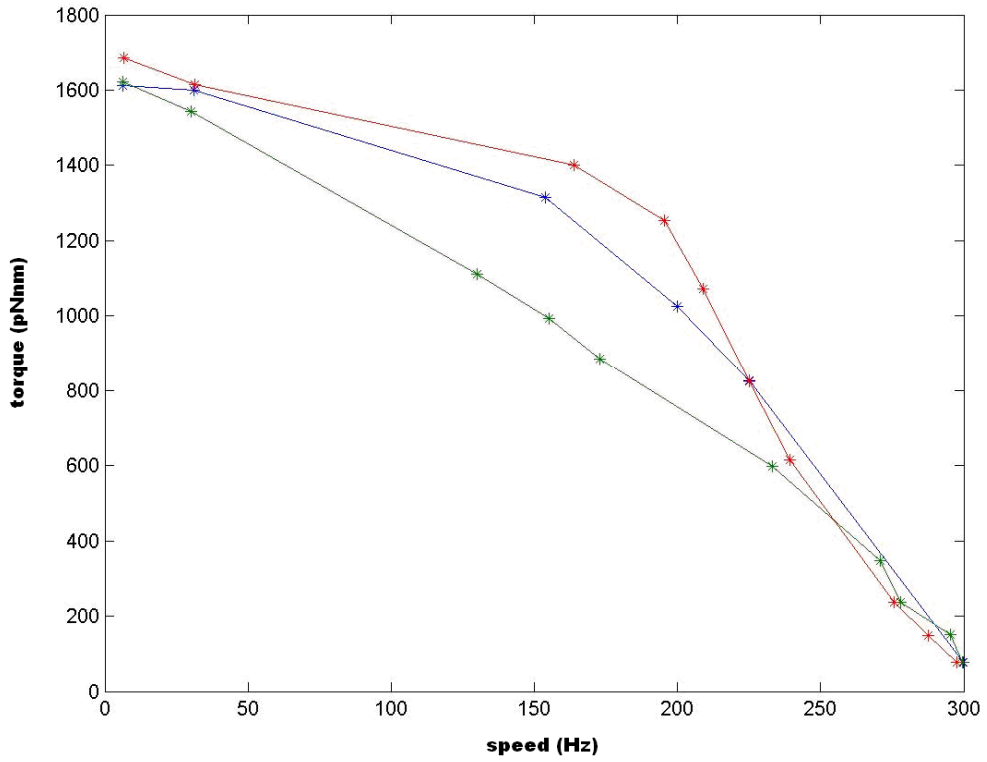

Figure 4.4.1 Model predicted BFM torque-speed curve at different hook stiffness (red) original value (blue) 10 times larger (green) 100 times larger.

4.5 CONCLUSION

Recent progress in the study of BFM has greatly pushed forward our understanding. This includes the observation of 26 steps/revolution in a slow rotating chimera motor and non equivalent control of motor speed between ion gradient and membrane potential. In this chapter we continued our exploration of the two-state Markov-Fokker-Planck model we constructed in Chapter 3, with special focus on the dynamics of the BFM. The questions we have discussed are: motor response to individual changes in ion concentration and membrane potential; BFM stepping behaviour; stepping statistics (step-size distribution, dwelling time distribution); predicted conditions under which wild type *E. coli* BFM stepping can be observed.

We first advanced the model by adding extra details to the dynamics of ion hopping on/off. Then we discussed the motor dynamics predicted by the model and compared them with experimental observations by presenting parallel results that can fit *E. coli* and chimera motor data respectively. Models of the two species derive from the same framework but differ by the values of some parameters (.e.g, ion hopping rates).

Although simply constructed, we showed that our model has captured the main physical properties of the BFM and explained many puzzles. More importantly, a series of testable predictions have also been made, which will become the starting point of a new generation of experiments, demonstrating the instructive power of mathematical modeling in directing experiments.

CHAPTER 5

Switching Dynamics of the Bacterial Flagellar Motor

The chemotaxis network that controls the motion of *E. coli* is one of the most fascinating and best studied sensory systems in biology. Impressive progress has been made in identifying the relevant signalling proteins and their interactions have been intensely investigated, making this system a good candidate for quantitative systems biology analysis. However, how the direction of the mechanical rotation of the flagellar motor is reversed by the signalling molecule CheY-P – a central step in this system – remains unclear. Here we have investigated the dynamics of bacterial switching with a fast and high precision optical trapping system. Switching, pausing and slowdown events have been presented in great detail. By measuring the switching time (the interval that the motor takes to complete a switch), we conclude that switching is not instantaneous. It shows a wide distribution with a characteristic time of 4-8ms while the fastest events take less than 1ms and the slowest take up to 100ms. This switching time distribution does not change with the direction of the switch (CCW-CW or CW-CCW) or the bias of the motor. We further show that the switching interval (the time that the motor dwells in each state) follows an exponential distribution.

The three pieces of evidence we present in this chapter are all direct predictions of the Ising Allosteric transition model. A comprehensive discussion of the model is included and dynamic parameters of motor switching are estimated. This work has established that the Ising phase transition model is a universal amplifying mechanism in both physical and biological systems.

This chapter is mainly reformed from the paper we are going to publish:
Bai, F., Branch, R.W., Nicolau, V.D., Pilizota, T., Maini, P.K. and Berry, R.M. Experimental evidence for conformational spread in the bacterial switch complex.

In this chapter, I designed and performed all the experiments and most of the data analysis. I also need to acknowledge the contributions from Richard Branch, Dan Nicolau, Teuta Pilizota, Philip Maini and Richard Berry and special thanks are given to Dr. Ian Graham and Prof. Thomas Duke from Cambridge University for introducing us the Ising Allostery model.

5.1 CHEMOTACTIC GAIN

A central goal in the study of the *E. coli* chemotaxis network is to locate the 'amplifier' in the system, which can convert subtle change in the attractant concentration into prodigious gain of rotation bias at the output end [89]. Recent findings have identified two amplification steps in the signalling pathway. One is at the beginning of the chemotactic network - the sensor cluster. The fractional change in receptor occupancy can generate fractional changes in kinase activity that are 35 times larger, via long-range cooperative interactions between receptors in the cluster [90]. The other one is at the BFM end: the motor is ultrasensitive to the concentration of the signalling molecule CheY-P [91]. A steep sigmoidal relationship has been revealed between the concentration of CheY-P and motor rotational bias (Figure

5.1.1). Earlier studies by Sourjik *et al.* [92] and Sagi *et al.* [93] revealed that binding of CheY-P to the FliM part of the motor is much less cooperative than the motor response and suggested that the amplification step is within the switch, subsequent to the binding of CheY-P. These results are all in favour of the Ising Allosteric model proposed by Duke *et al.* [94], which provides a new view of allostery and can reproduce the ultrasensitivity of the BFM to CheY-P.

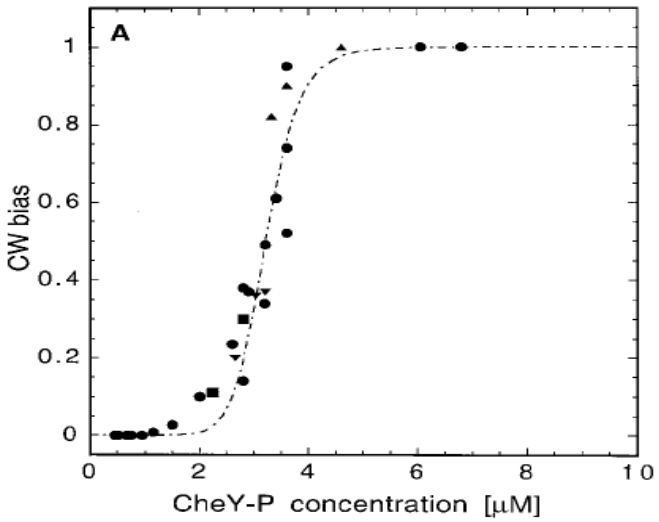

Figure 5.1.1 Response curve between chemotactic regulator CheY-P concentration and motor rotation bias revealing ultrasensitivity at the flagellar motor end (figure is courtesy of reference [91])

5.2 ISING ALLOSTERIC MODEL OF THE BFM SWITCH COMPLEX

In the Ising Allosteric model, the subunits of the BFM switch complex are assumed to exist in two distinct conformations corresponding to CW and CCW rotational states. A subunit makes rapid stochastic transitions between the above two states and may also bind a single molecule of CheY-P, present in the surrounding solution at a given concentration. When no CheY-P binds to the subunit, the CCW state is energetically favoured by E_A and the binding of CheY-P stabilizes the CW state. The free energy diagram for the energy states that a subunit may exist in is

shown in Figure 5.2.1.

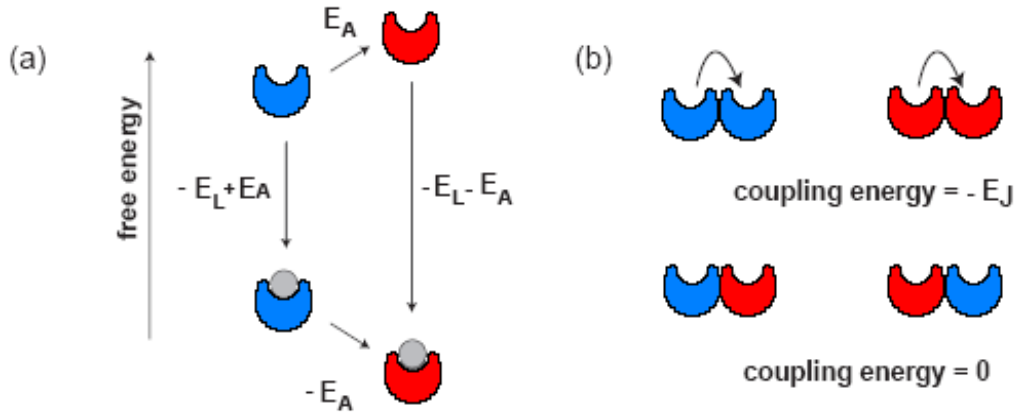

Figure 5.2.1 Energy states of a subunit in the BFM switch complex. (a) The free energy of the CW state (red) changes from $+E_A$ to $-E_A$ relative to the CCW state (blue), when a subunit binds CheY-P. E_L represents the binding energy in the absence of any conformational change ($E_A=0$). (b) The subunit is stabilized by E_J if the adjacent neighbor is in the same conformation.

In order to model the ultrasensitivity, a coupling energy E_J between adjacent neighbors in the ring is introduced. The free energy of a subunit is reduced by an amount equal to the coupling energy E_J for each neighboring subunit that is in the same conformational state.

The probability of transition between state 1 and state 2 of a subunit is proportional to

$exp(-(energy_2-energy_1)/kT)$, formula (5.1)

where k is Boltzmann's constant and T is temperature and $energy_1$ and $energy_2$ are the energies of state 1 and state 2 respectively.

The ratio of the dissociation constants for CheY-P from CW and CCW subunits, K_d^{CW} / K_d^{CCW}, is given by $exp(-2E_A/kT)$.

Below a critical coupling energy, the ring exhibits a random pattern of states as the subunits flip independently of each other. Above the critical coupling energy, switch-like behaviour ensues: the ring spends the majority of time in a coherent

configuration, stochastically switching between the two extreme states where subunits are either all CW or all CCW. The proportion of time spent in each of the bistable configurations is governed by the concentration of CheY-P, with the sensitivity of the system to variations in this concentration determined by E_A.

By implementing parallel Monte Carlo processes, a computer program has been developed by my colleague Dan Nicolau to simulate the transition behaviour of the ring of subunits of the BFM switch complex. In each iteration, every subunit on the ring is polled by formula 5.1 to determine whether to stay in the old state or jump to a new state according to the free energy difference between the old state and the new state as a function of 1) free energy of the subunit itself 2) binding condition of the regulator molecule CheY-P 3) energy state of adjacent neighboring subunits.

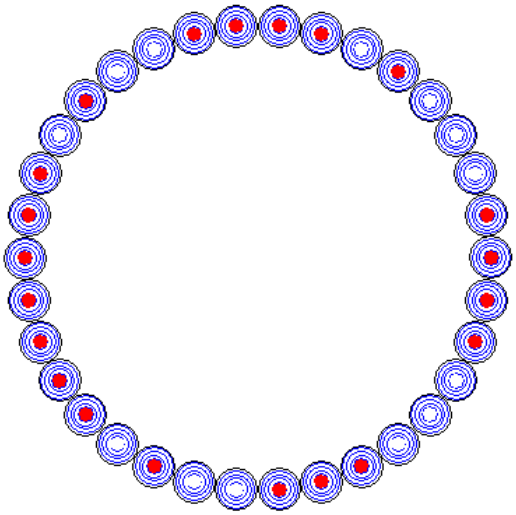

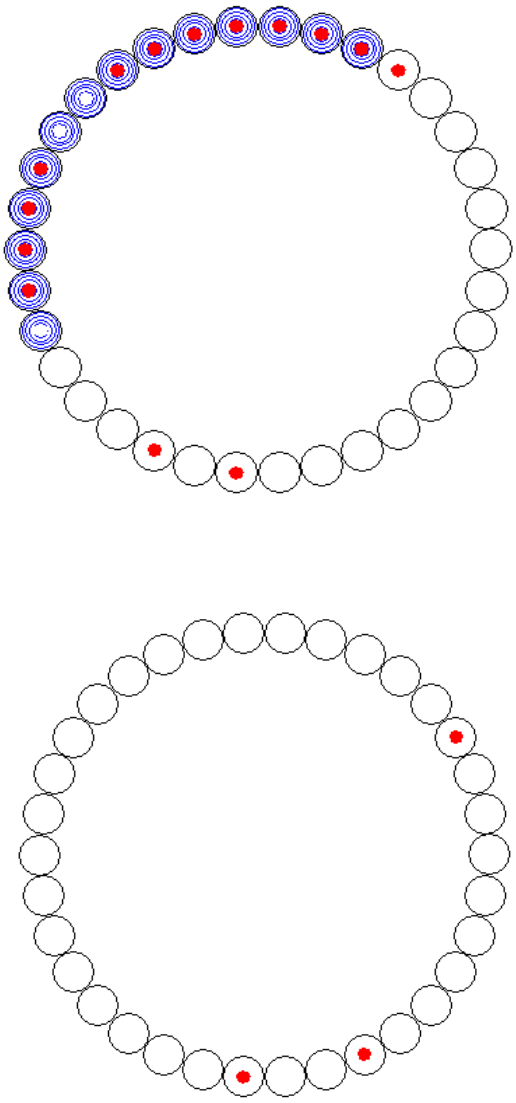

Figure 5.2.2 Snapshots from the simulation realizing the Ising Allosteric model. On these plots, each subunit can exist in either the CCW state (white circle) or CW state (blue circle). The CheY-P regulator is indicated by red dots in the middle.

In Figure 5.2.2 we show a series of snapshots taken from this Ising Allosteric model simulation program. In this program, the model has five free parameters, E_A, E_J, basic flipping rate k of each subunit, and the binding/unbinding rate k_{on}/k_{off} of CheY-P to each subunit.

5.2.1 Structural Basis for the Ising Allosteric Model

The original Ising Allosteric model proposed by Duke *et al.* is a general model for allostery. Here we discuss putative structural bases for its application to the BFM system.

In the BFM, critical charge residues on the FliG C-terminal domain are found to interact electrostatically with opposite charge residues on the cytoplasmic loops of the stator complex. The chemotactic signalling molecule CheY-P binds to FliM [95-96] and increases the probability of CW rotation. CheY-P binding presumably triggers a conformational change in FliM (and FliN) that is transmitted to FliG to reorientate its C-terminal with respect to the stator complexes. Recent publications support this idea by locating a putative hinge region in the FliG structure [81][97], along residues 183-196 connecting the C-terminal domain and the middle domain. Mutational studies replacing these 'hinge' residues generates a group of mutants that are extreme in bias (exclusively CCW or CW), less frequently switching, rapidly switching, transiently paused and permanently paused [98]. This result strongly argues that this hinge region is directly involved in switching of the BFM.

The following two models are all based on the assumption that this hinge region allows a relative movement of the C-terminal domain of FliG to the middle domain during a switch. They represent possible structural bases for the Ising Allosteric model.

Scheme 1:

This model is based on a crossbridge-type stepping mechanism. Biochemical and structural analyses suggest torque generation occurs via conformational changes in the stator unit upon ion binding/unbinding to the negatively charged D32 residue on the

MotB helices. This motion pushes/pulls the rotor by means of electrostatic and/or steric interactions at the stator-rotor interface. Critical charge residues responsible for this interaction have been labelled in Figure 5.2.3 a. Our main concern here is to understand how two opposite rotations could be generated by the same stator movement. Certainly, ion flux is not reversed in the natural CW state induced by chemotactic signalling (in forced reversed rotation by external torque such as with electrorotation or optical tweezers, ion flux through the stator is suspected to change direction and the motor functions as an ion pump, given the assumption of tight coupling. However, this idea requires further experimental evidence). The existence of the hinge region allows us to propose hypothetical models. Our first model is depicted in Figure 5.2.3 b, with the corresponding periplasmic view given in Figure 5.2.3 c. This scheme makes the most of the MotA4MotB2 stoichiometry: the C-terminal of the FliG interacts with the nearer two MotA cytoplasmic loops in CCW rotation and the farther two MotA loops in CW rotation. Changes in the occupation state of the channel result in relative movement between MotA and MotB for both of the two half stators driving cyclic motions of the cytoplasmic loops on MotA. The two cytoplasmic loops engage the rotor alternately (to ensure the high duty ratio) during the first and second half of the cycle to push the rotor. Due to the symmetrical arrangement in the stator complex, in a full motor cycle, the farther two MotA cytoplasmic loops undergo a similar conformational change as the nearer two, but in an opposite direction. The switching puzzle could be resolved if binding of the CheY-P molecule to FliM triggers the spatial reorientation of the C-terminal FliG to a different interacting track (see Figure 5.2.3 c). Current structural data are not sufficient to verify this model but the distribution of charge residues on FliG and MotA are compatible in both working modes.

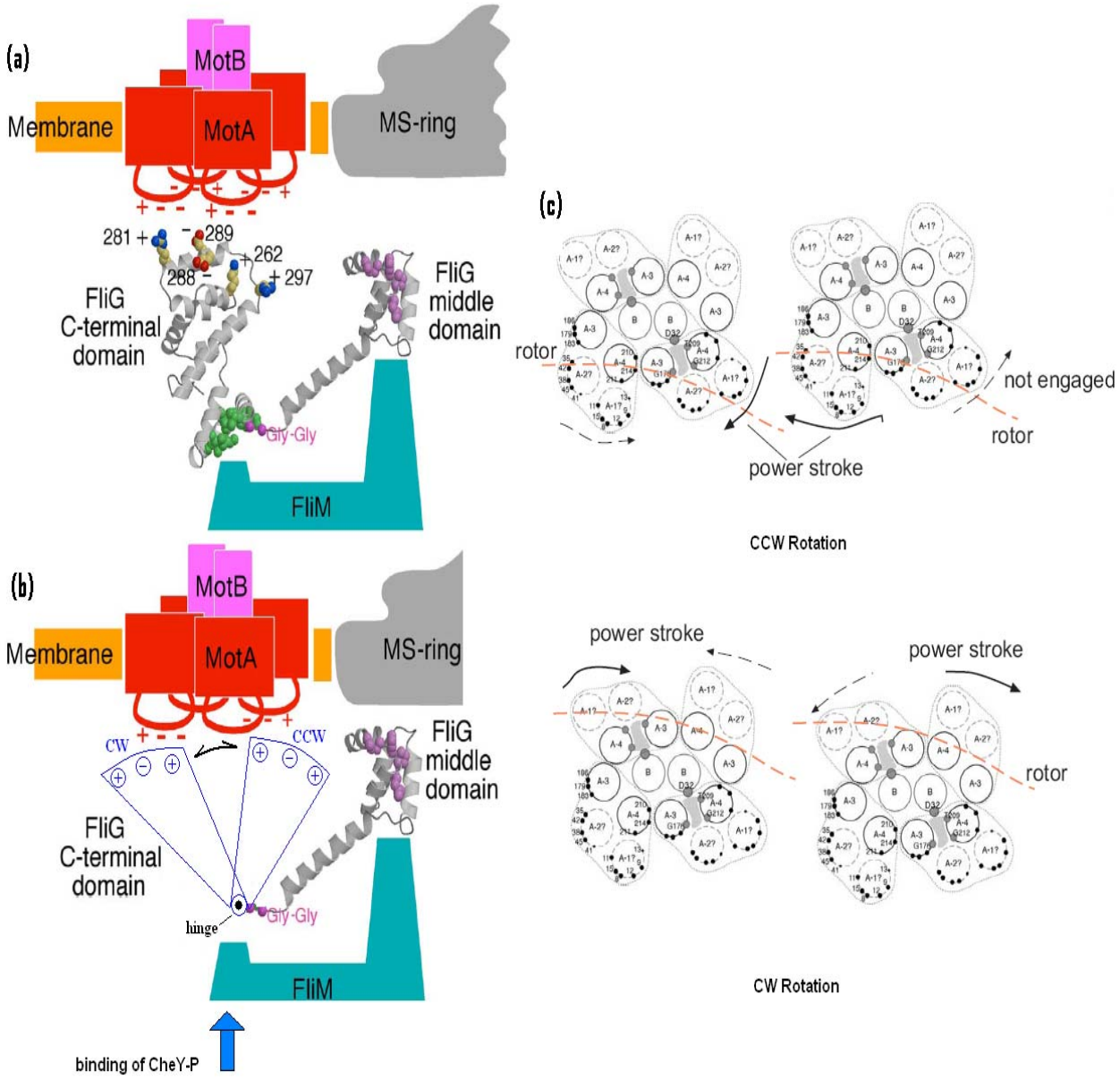

Figure 5.2.3 Hypothetical FliG conformational transitions driving the switch — Scheme 1. (*a*) crucial charge residues for the torque generation at the stator-rotor interface. (*b*) side view of the proposed FliG reorientation upon CheY-P binding. Charge residues on the stator and rotor are compatible when FliG interacts with either the nearer end of the MotA4MotB2 complex or the farther end. *(c)* top view of the two tracks on which the stator interacts with the rotor, corresponding to counter-clockwise and clockwise rotations. Switching rotation direction can be achieved by a conformational change in the FliG C-terminal domain controlled by CheY-P binding to the rotor.

Scheme 2

This model is based on the 'two pistons' stepping mechanism proposed by Xing *et al.* [99] (Chapter 3). Kojima and Blair's work [82] showed that when an ion binds to the D32 residue on MotB, a conformational change occurs in the stator complex. However, this conformational change might not only have an effect in the horizontal plane. The cytoplasmic loop between the MotA helix 2 and 3 may stretch and withdraw in the vertical plane acting like a piston. This up-and-down motion interacts with the rotor electrostatically and/or sterically to generate power strokes (which would require an inclined stator-rotor contact surface as shown in Figure 5.2.4 a and the accompanying movie of reference [99]). The switching puzzle can be resolved in this model by assuming a different FliG/FliM assembly on the rotor that forms an opposite inclination on the stator-rotor contact surface. Figure 5.2.4 b is the crystal structure of FliG taken from RCSB Protein Data Bank. Again, the flexible hinge region allows a spatial reorientation of the FliG C terminal, but this time FliG is not required to span the stator complex in the radial direction as proposed in Scheme 1. It only changes the way it leans against the neighbours when CheY-P binds to the FliG/FliM complex (Figure 5.2.4 c). This picture is structurally more probable.

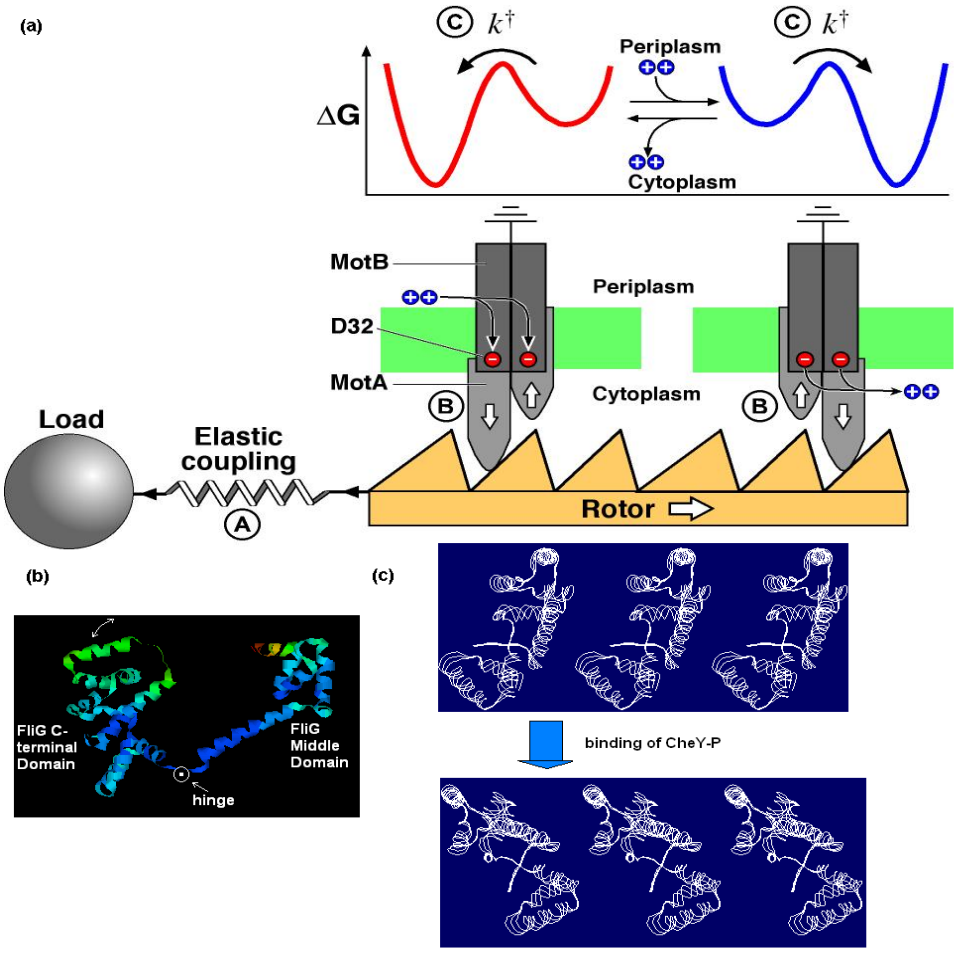

Figure 5.2.4 Hypothetical FliG conformational transitions driving the switch — Scheme 2. (*a*) a carton picture shows the 'two piston' stepping mechanism (*b*) side view of the FliG crystal structure (taken from RCSB Protein Data Bank No.1LKV) *(c)* view on the radial axis (facing the centre of the ring) of the two opposite inclinations of the stator-rotor contact surface. Switching rotation direction can be achieved by a conformational change in the FliG C-terminal domain controlled by CheY-P binding to the rotor.

The above two models provide structural foundations for the Ising Allosteric model. Each FliG/FliM complex can exist in two conformations that lead to CCW/CW rotation respectively. The fact that these complexes are packed up into a ring structure naturally gives rise to the coupling energy between neighbours, which is the essential element of the Ising Allosteric model.

5.2.2 Predictions of the Ising Allosteric Model

A strong coupling energy in the Ising Allosteric model (E_A =1 k_BT , E_J= 4 k_BT) can reproduce the ultrasensitivity (Figure 5.1.1) of the motor bias to CheY-P concentration (see Figure 6 of reference [94]). Further support for the model can be gained by testing predictions of the model, which are explored here.

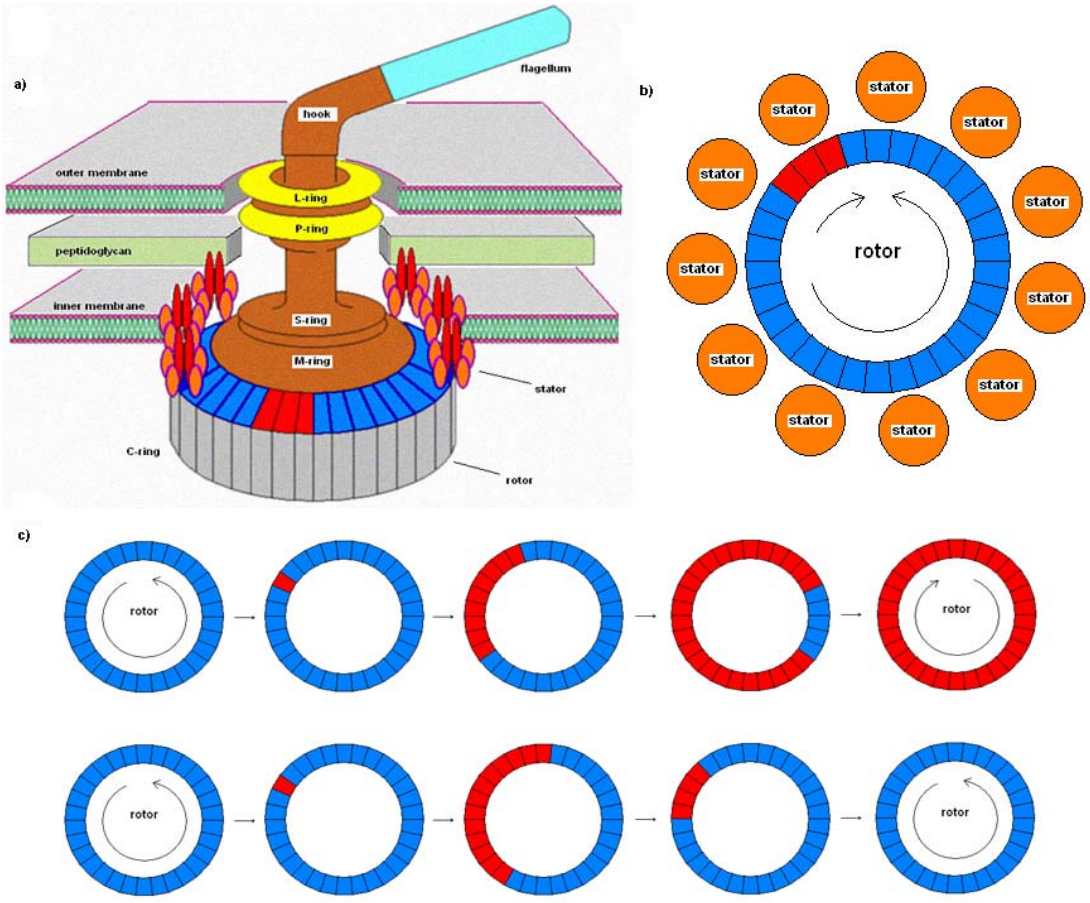

Figure 5.2.5 Cartoon plot showing the conformational spread on the FliG/FliM ring as a mechanism for bacterial switching. (a) 3 D view of the motor structure. Stator units are interacting with the FliG/FliM ring with a mixed conformation of CCW/CW subunits. (b) view from cytoplasm of the same structure as in (a) (c) a nucleation event followed by successful growth will eventually encompass the whole ring; but more frequently, the event will collapse due to the strong coupling energy of neighboring subunits.

In Figure 5.2.5 we show a key element of the Ising Allosteric model – conformational spread. Switches are observed to occur via a nucleation event -

typically the flipping of one subunit to the opposite state – followed by growth of the new domain until it encompasses the entire ring as demonstrated in Figure 5.2.5 c. However, this conformational spread is not always successful. For most of the time, the 'seed' of the opposite conformation will soon disappear due to the strong coupling energy of neighboring subunits. This conformational spread as a mechanism for bacterial switching is the unique feature of the Ising Allosteric model. Next we construct a simple mathematical model to translate the ring activity simulated by the Ising Allosteric model into motor speed that can easily be observed.

The latest result by Reid *et al.* revealed that the maximum number of torque-generating units in *E. coli* is at least 11 [57]. When the rotor interacts with this many stators, it is the percentage of CCW complexes on the ring rather than the distribution of CCW complexes that determines motor speed; additionally, due to the strong coupling energy, the chance of seeing more than two domains on the ring is very small. Therefore we make a simple assumption that a subunit in the CCW/CW state will promote CCW/CW rotation so that there is a direct proportionality between the overall state of the switch complex and motor speed: for example, 34 CCW/CW subunits will cause full speed CCW/CW rotation; 17 CCW and 17 CW subunits will result in a stationary motor. This assumption will fail if there are only 1-2 stators in the system, which will be investigated in future work. Here we use this linear approximation, as in our experiments we all use a fully resurrected wild-type *E. coli* strain.

The proportionality between the state of the switch complex and motor speed is given by

$$V_{rotor}(t) = V_0(N(t) - 17)/17; \qquad \text{formula (5.2)}$$

V_0 is an average speed taken from our experimental data or published torque-speed curves at a given load.

Langevin simulation can be used to describe the motor movement as in Chapter 3. In each simulation step (we choose $\Delta t = 10^{-7}\, s$), rotor position is updated following:

$$\theta_{rotor}(t+\Delta t) = \theta_{rotor}(t) + V_{rotor}(t)\Delta t\,; \qquad \text{formula (5.3)}$$

here V_{rotor} is the instantaneous speed calculated from formula (5.2) as a function of the $N(t)$ subunits out of 34 that are in the CCW state predicted by the Ising Allosteric model simulation at time t (this can be done by running two simulations in parallel and transfer the $N(t)$ value to the Langevin simulation).

In our experiments, all switching behaviour of the BFM is observed through the response of a latex bead attached to the flexible hook/flagellum. To make any comparison between our experimental results and predictions from the Ising Allosteric model, we need to take the bead movement into account.

Bead position is updated by introducing a Wiener process

$$\theta_{bead}(t+\Delta t) \approx \theta_{bead}(t) + \frac{\tau}{\zeta_{bead}}\Delta t + \sqrt{2D_{bead}\Delta t}\,Z\,; \qquad \text{formula (5.4)}$$

here Z is a normal random variable with zero mean and unit variance (3), ζ_{bead} is the drag coefficient of the bead, D_{bead} is the diffusion coefficient of the bead following

$$D_{bead} = \frac{k_B T}{\zeta_{bead}}\,; \qquad \text{formula (5.5)}$$

τ is the torque delivered through the flexible linkage in the hook/flagellum that can be modelled by assuming an ideal elastic spring

$$\tau = k(\theta_{rotor} - \theta_{bead})\,; \qquad \text{formula (5.6)}$$

where k is the experimentally determined stiffness of the hook/flagellum [68].

Here we have developed a model framework that can correctly transfer the activity on the ring to an experimentally observable movement of the bead. In later parts of this chapter, when we refer to 'simulated motor speed', 'simulated switching interval distribution', 'simulated switching time distribution', we mean that they are all generated by this model framework.

Below we show an example of how this model framework works.

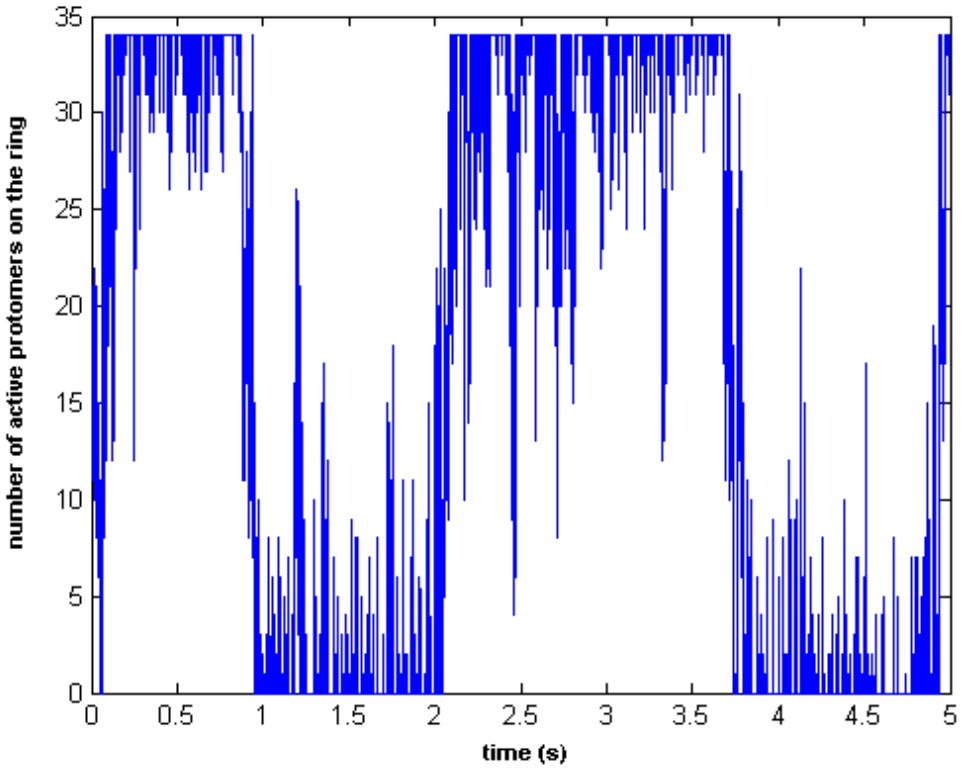

Figure 5.2.6 Five second record of the number of CCW subunits on the ring predicted by the Ising Allosteric model simulation program.

In Figure 5.2.6 we show a 5 second long record of the number of CCW subunits on the ring predicted by the Ising Allosteric model. Because of the strong coupling energy, we can roughly identify two coherent states of the ring in the above trace (complete CCW state, N=34; complete CW state, N=0), though fluctuations from these two coherent states are frequent. The instantaneous ring activity was used to calculate the instantaneous rotor speed according to formula 5.2. The rotor moves

at this speed, twisting the flexible hook/flagellum and hence delivering torque to the bead. By running the Langevin simulation, we can generate the bead trace (Figure 5.2.7).

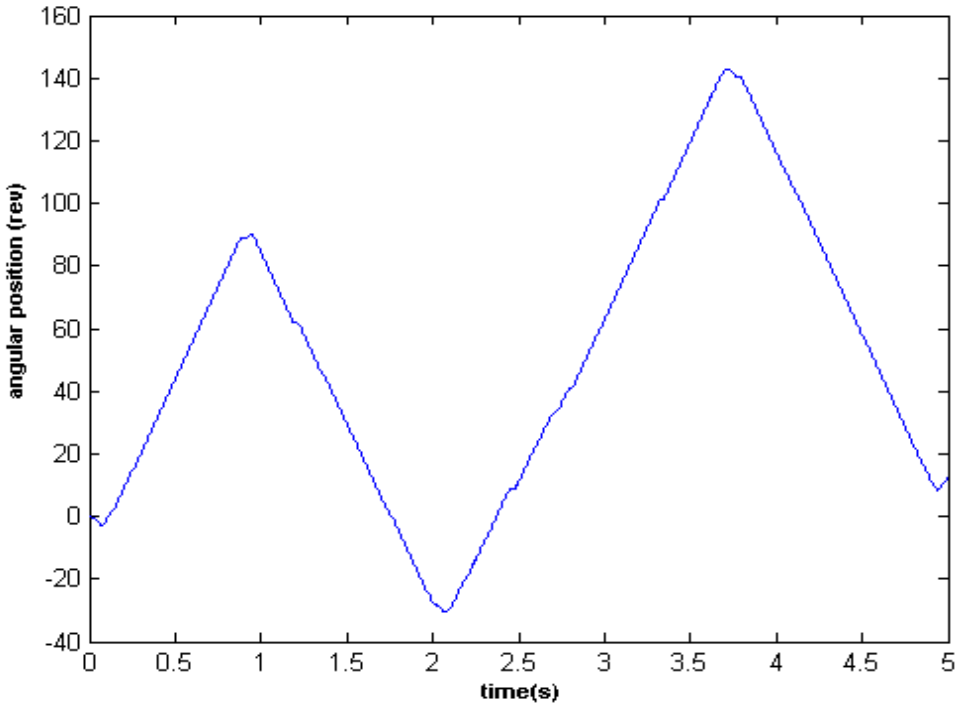

Figure 5.2.7 Bead response to the ring activity (Figure 5.2.6) predicted by the Ising Allosteric model

Comparing Figure 5.2.6 and Figure 5.2.7 we see the bead responds sensitively to the ring activity. When a majority of the ring is in the same conformation, the bead displays a smooth running. When the ring exists transiently in a mixed state, the bead pauses and slow downs; and reversal of direction occurs when the CCW subunits on the ring jumps from 0 to 34 or 34 to 0.

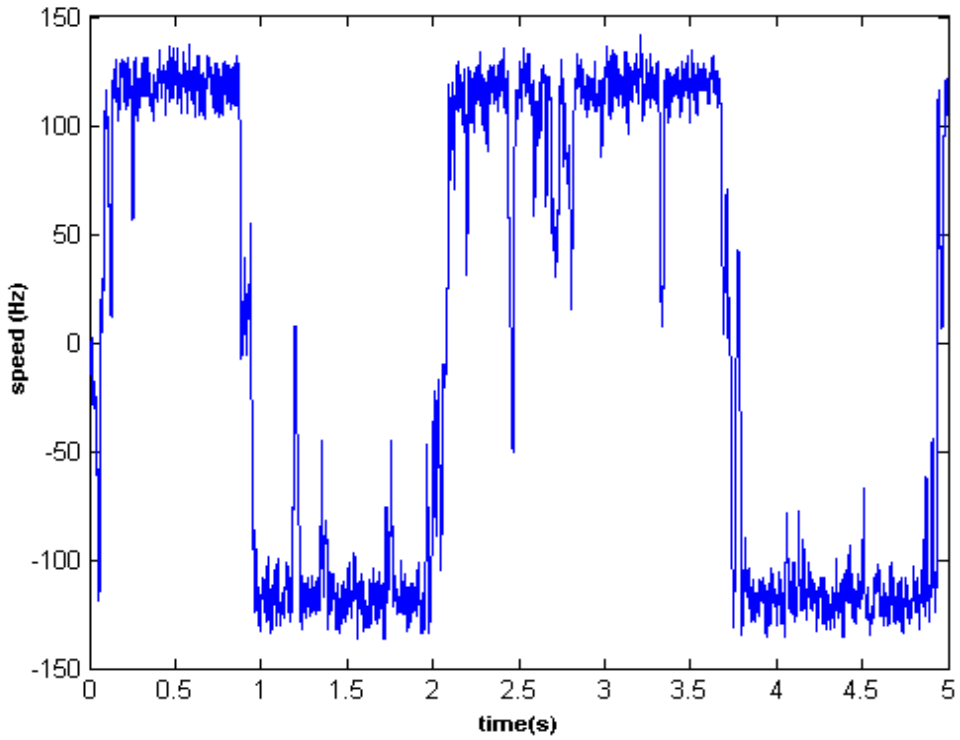

Figure 5.2.8 Filtered bead speed vs time trace calculated from the bead movement in Figure 5.2.7.

The speed of the bead, which is a directly observable quantity in our optical trapping system, can be calculated from the bead trace (Figure 5.2.6). The instantaneous bead speed is calculated by taking the derivative of adjacent points in the bead trace. However, this speed calculated by a two-point derivative is excessively noisy. This problem can be solved by applying a 100 point median filter (Figure 5.2.7) (the same method as we apply to the experimental data when we taking measurements at the sampling rate of 10 kHz). Comparing Figure 5.2.5 to Figure 5.2.7, our model has correctly translated the activity on the ring to the speed of the motor output. We notice that the existence of the flexible hook/flagellum and viscous drag of the bead smooths the ring activity. Small deviations from a coherent (0 or 34) state are filtered out and now hidden in the speed fluctuations. Only major breaks from the coherent state are preserved in the speed vs. time trace, observed as ‘slowdown’ and ‘pausing’ events.

With the above model framework, we are able to examine the unique features of the Ising Allosteric model.

If the Ising Allosteric model is the actual molecular amplification mechanism at the BFM end, three direct consequences should be observable:

1) Creation of domains of the opposite conformation is frequent due to fast flipping of single FliM/FliG subunits, but most of them shrink and disappear, failing to occupy the whole ring. However, some big fluctuations can still produce obvious slowdowns and pausing of the motor. Therefore, switching behaviour of the BFM does not produce a standard binary trace. The trace contains frequent speed slowdowns and pauses.

2) The switch interval (the time that the motor spends in the CCW or CW state) follows a single exponential distribution.

3) The time that the motor takes to complete a switch (switching time) is non-instantaneous. It can be modeled as a biased random walk along the ring. The characteristic switching time depends on the size of the ring and flipping rate of each subunit in a complicated manner and due to the stochastic nature of this conformational spread, we expect to see a wide distribution of switching times.

Testing the above three predictions is the goal of our experiments.

5.3 DYNAMICS OF BACTERIAL SWITCHING

5.3.1 Studies of the Switching, Pausing, Slowdown Events

Visual examination of speed records outputted from the Labview program reveals that the motor (WT strain KAF 84 with 0.50 μm bead attached as an indicator) is ordinarily locked in either a CW or CCW state, with switches between these states

accomplished rapidly. Contrary to representing a binary trace as reported recently, also visible are transient fluctuations in speed, to various levels including zero speed and reverse speeds, which do not reach the opposite locked state (Figure 5.3.1 a). Evidently from the angular position records (Figure 5.3.1 c d), a switch event begins with a deceleration in the original direction of rotation down to zero speed, and dwelling, then continues to accelerate in the reverse direction to full speed. Transient events to any level comprise a deceleration to a given speed, a dwell time of ~milliseconds at that speed, and acceleration back to the original speed.

The unparalleled resolution offered by our setup confirms the first prediction of the model regarding the existence of transient fluctuations in motor speed. Though these events have been reported previously [101-102], doubts have existed as to whether early resolutions were satisfactory to conclude their existence. The transient events are not an artefact due to mechanical hindrances experienced by the bead on its orbit. By monitoring the angular positions of these events, we conclude that they do not occur at fixed angles (Figure 5.3.1 b e f, Figure 5.3.2), as would be expected if mechanical hindrances were responsible. Additionally, in all our BFP data, a systematic binomial test demonstrates that the angles of pauses are uniformly randomly distributed around the orbit, with a confidence level of 0.01. The presence of transient events was also observed in an alternative switching *E. coli* strain (HCB 1271). Meanwhile, their absence in a non-switching *E. coli* (KAF95) strain (Figure 5.3.3) indicates further that the bead assay is not susceptible to hindrances and that the events are dependant on a functional chemotaxis network; notably, the events persist in WT *E. coli* records that are devoid of switching events (from extreme bias cells).

Figure 5.3.1 (see next page) Studies of the switching, pausing and slowdown events using our BFP data. a) A typical 30 second long speed vs. time trace of a cell we recorded in the optical trapping system. Switching, pausing and slowdown events are frequent and have been labelled by arrows of different colours. b) a typical slowdown event (green arrow). X, Y records and its angular position on the rotating orbit are shown. c) a typical switching event (purple arrow) d) a typical successive switching event (two switching events happens close to each other; grey arrow) e)-f) typical pause events (red arrow).

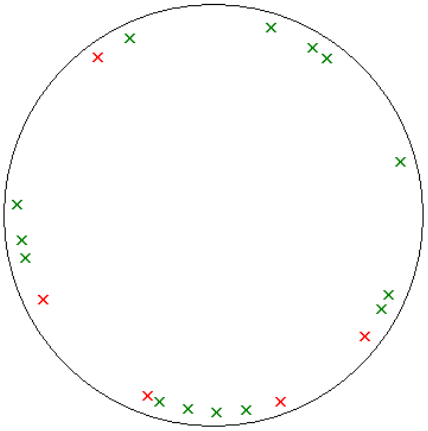

Figure 5.3.2 Angular locations of all the pausing and slowdown events from Figure 5.3.1 a trace. These events are distributed widely on the rotation orbit.

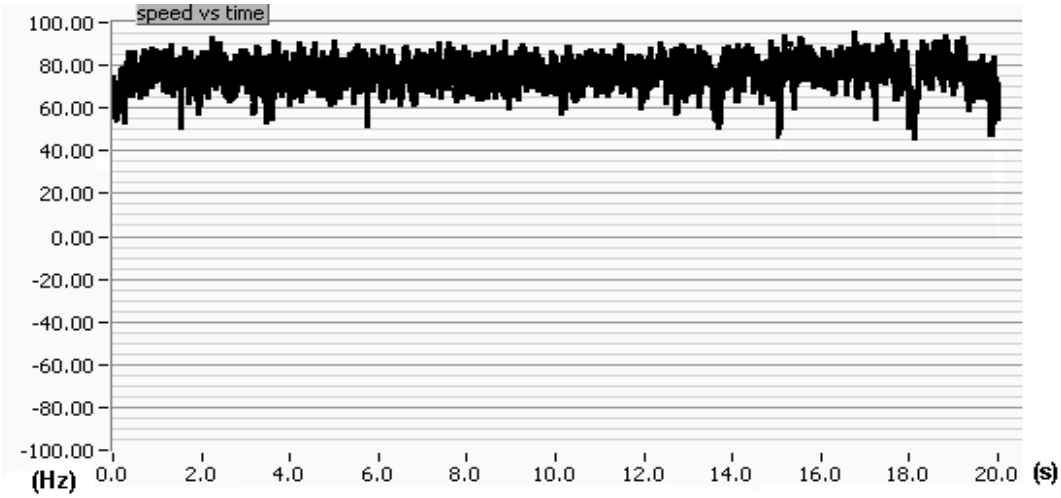

Figure 5.3.3 Speed vs. time trace taken from a non switching cell (strain KAF 95). Slowdown and pausing events are not seen.

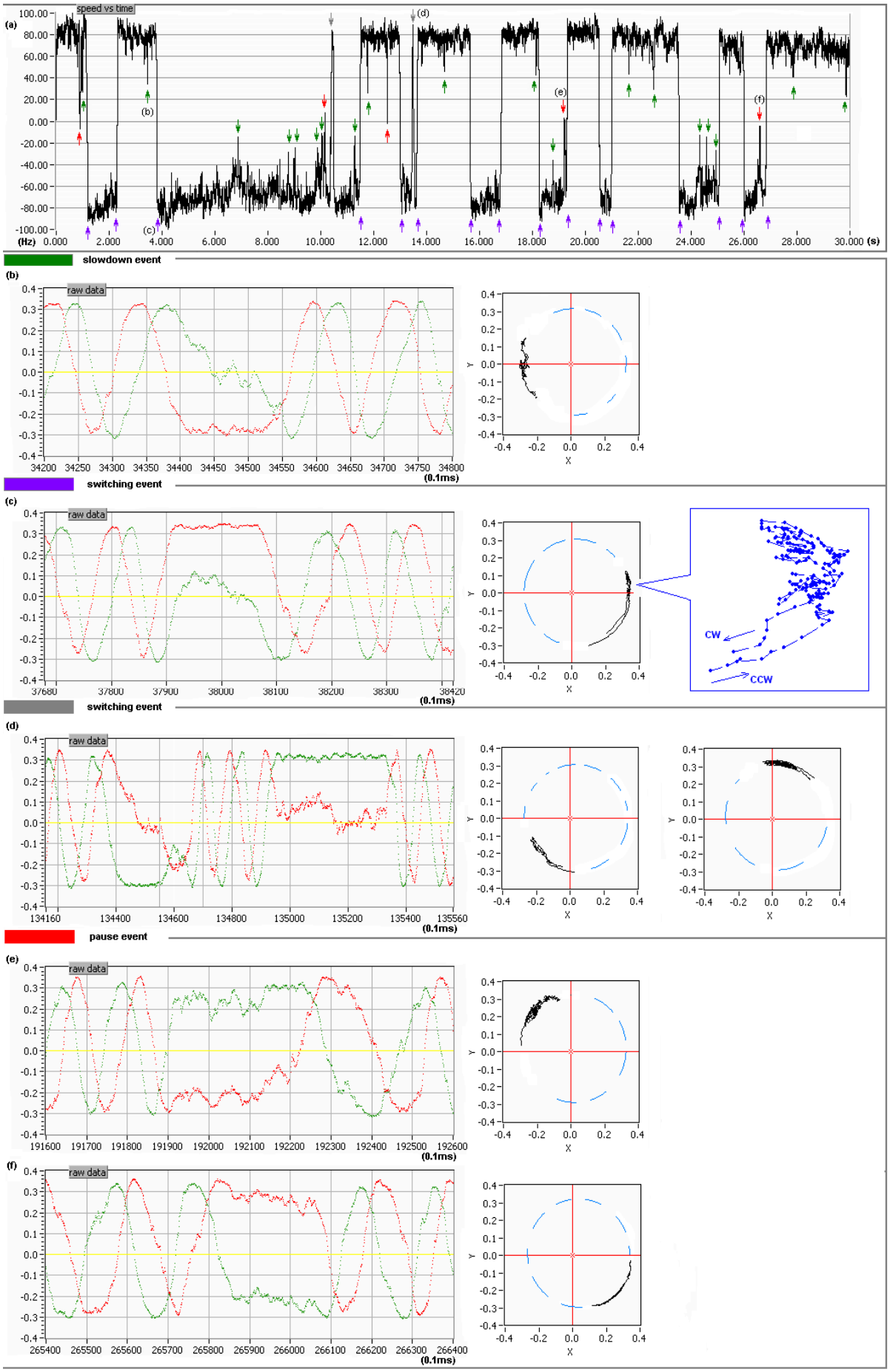
speed vs time
(a)
(b)
(c)
(d)
(e)
(f)
(Hz)
(s)
slowdown event
(b)
raw data
(0.1ms)
switching event
(c)
raw data
CW
CCW
(0.1ms)
switching event
(d)
raw data
(0.1ms)
pause event
(e)
raw data
(0.1ms)
(f)
raw data
(0.1ms)

5.3.2 Switching Interval Distribution

This part is contributed by my colleague, Richard Branch. Here I only give a brief introduction to his analysis method and present the final result.

For the interval work, only speed vs. time traces exhibiting bimodal speed histograms were considered. Furthermore, testing was conducted to disregard any records whose pause angles were determined to be non-uniformly randomly distributed. These measures ensure records are suitable for the implementation of a custom Matlab switching interval finding algorithm. The algorithm is designed to reliably determine the duration of locked state intervals without effect from transient events, which might otherwise skew the distribution towards a shorter timescale.

For the purposes of setting non-arbitrary thresholds, a speed histogram is constructed from a given speed vs. time trace. The histogram typically exhibits two major peaks corresponding to the locked states. Gaussian fitting to the two major peaks provides mean speed M_{CCW} and M_{CW} and standard deviations S_{CCW} and S_{CW} for the two locked states, with which thresholds can be systematically defined.

Positive and negative thresholds are set at M_{CCW}-$3S_{CCW}$ and M_{CW}+$3S_{CW}$ respectively. The algorithm output is robust to variation in threshold setting. Upward passages across the positive threshold mark the end of a CW interval and the beginning of a CCW interval. Downward passages across the negative threshold mark the end of a CCW interval and the beginning of a CW interval. Measurement of intervals is demonstrated in Figure 5.3.4.

The interval distributions for locked CW and CCW states were determined systematically from speed records of 538 cells. Data were binned by bias to compare the kinetics of cells with different levels of CheY-P activity. Maximum likelihood estimation was used to obtain the parameters of the distributions. The distributions for

both CW and CCW intervals across all nine bias bins are displayed in Figure 5.3.5. We conclude that WT *E. coli* switching intervals are exponentially distributed, confirming the second prediction of the Ising Allosteric model.

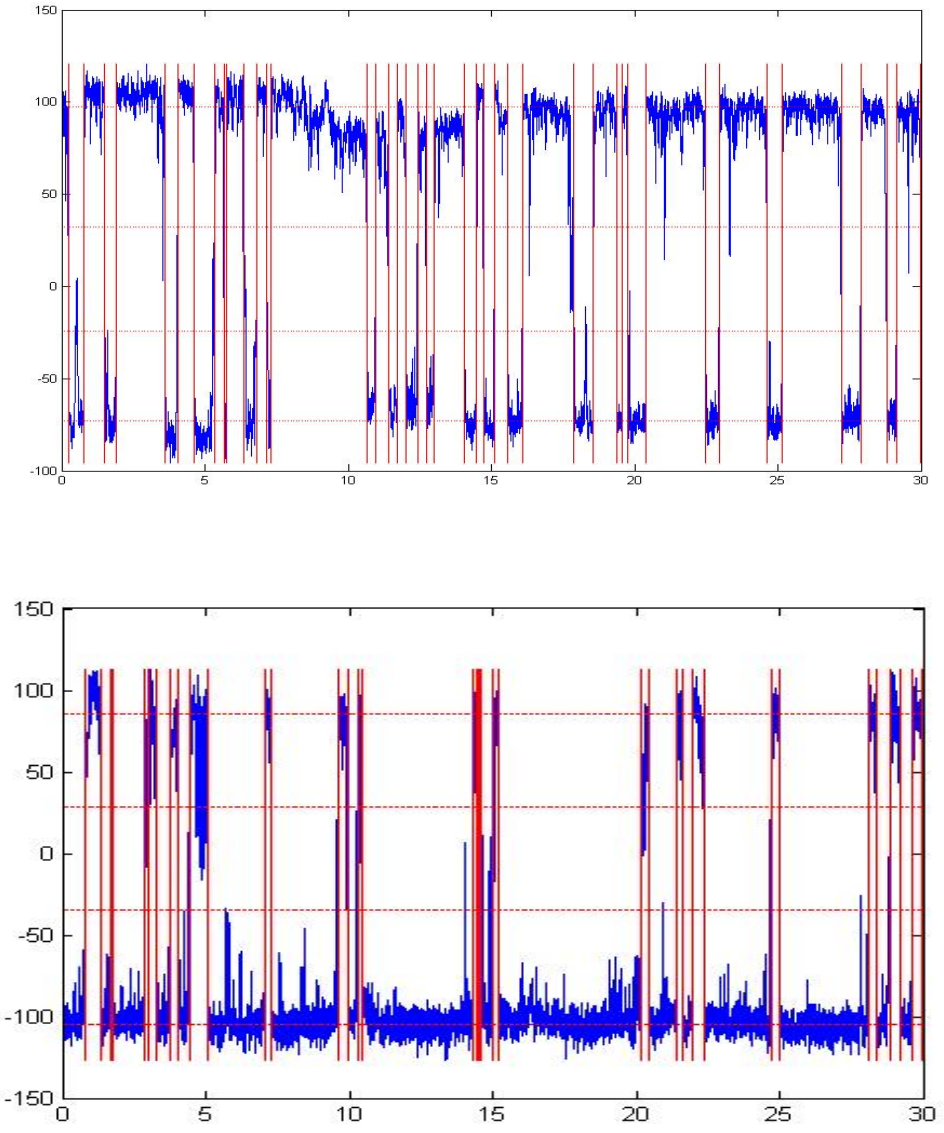

Figure 5.3.4 A custom written Matlab program can accurately find the length of switching intervals from our 30 second speed vs. time records.

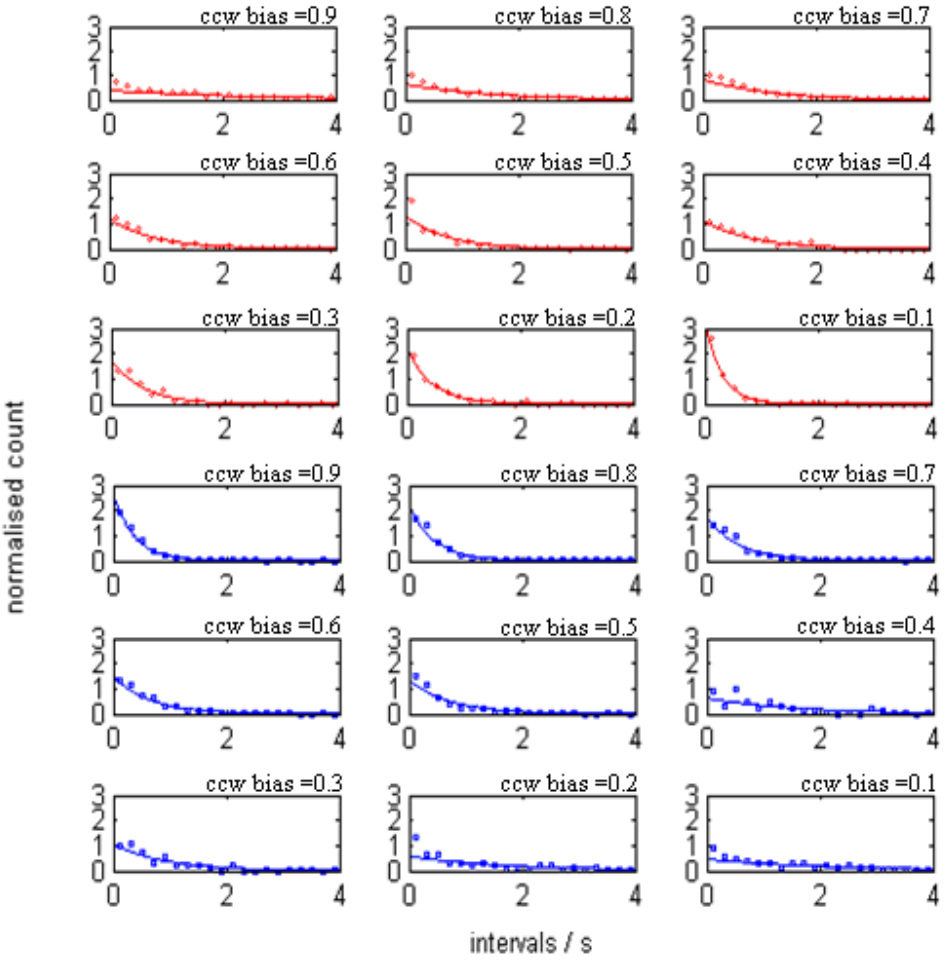

Figure 5.3.5 Distributions of the switching interval for both the CCW (red) and CW (blue) states across 9 bias bins. No peak is found in the distributions and they can be well fitted by exponential distributions.

5.3.3 Switching Time Distribution

In order to get an accurate measurement of the switching time, we follow a strict selection procedure in our data analysis:

1. When we take the data, the trajectory of the rotating bead is monitored in real-time by custom LabView program. We only select the cells that show steady circular or elliptical trajectories.
2. An ellipse fitting program was applied to the data recorded from the quadrant detector and motor angles were obtained. This program outputs 1) motor angle (revolution) vs. time; 2) instantaneous angular speed (calculated by taking the derivative of adjacent angular points) 3) rotation speed (smoothing the

instantaneous speed with a 100 point median filter) vs. time 4) radius of the circle as an indicator of fitting goodness.

3. We went through all the cells we recorded and excluded those cells that 1) cease rotation during the 30 seconds 2) do not switch during the 30 seconds 3) rotates too slowly (below 60Hz) 4) do not stay on the same circular orbit stably.
4. On these 'good switching cells', we apply a custom-written Matlab program to find the switching time distribution. It works with the output of the above Labview ellipse fitting program. First, the filtered speed vs. time plot was used to construct the histogram of the speeds (Figure 5.3.6), in which two peaks can be easily identified, corresponding to the rotation speed in CCW and CW modes respectively.

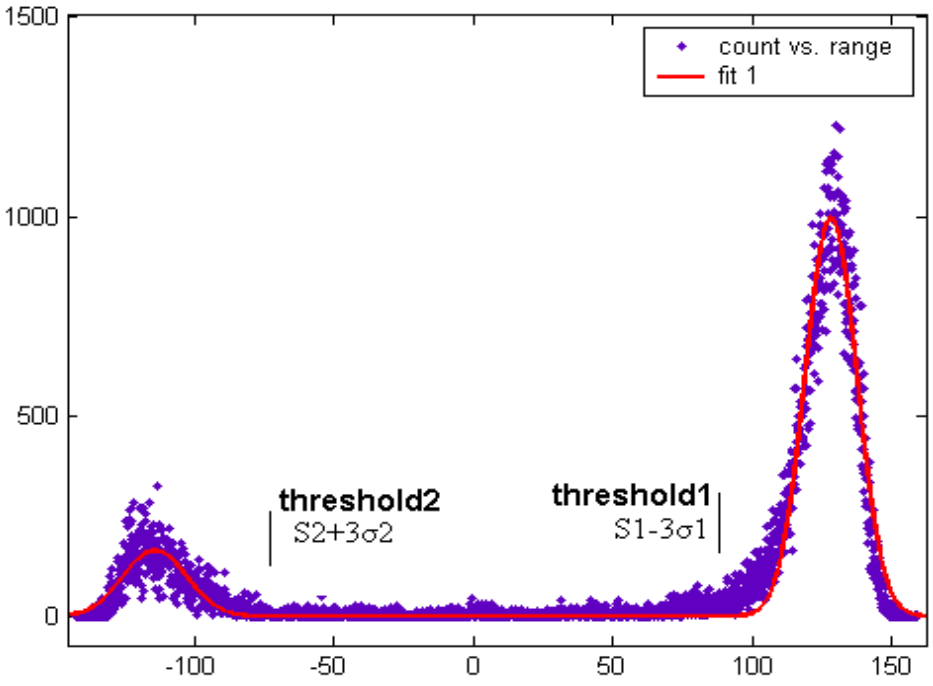

Figure 5.3.6 Speed histogram constructed from the speed vs. time records.

We run Gaussian fitting to these two peaks. As the shape of the speed histogram is influenced asymmetrically by transient pausing or slowdown

events, we therefore fit the outside portion of these two peaks to a Gaussian function, which gives us an accurate measure of the CCW speed S1 and its standard deviation σ1, CW speed S2 and its standard deviation σ2.

5. We construct two thresholds: the up-threshold is set as S1-3σ1 and the down-threshold as S2+3σ2. A switching event can be accurately located in the speed –time record if the program sees the speed pass through both thresholds; the direction of passage is used to label the direction of the switch CCW-CW or CW-CCW. The midpoint between these two thresholds is saved as the centre point of the switch event. (illustrated in Figure 5.3.7)
6. The finding program then inputs the revolution vs. time (unfiltered) trace and searches for all the centre points of switch events that have been recorded in Step 5. A typical switching event on the revolution vs. time trace is shown in the inset of Figure 5.3.7. In a switching event, we normally see a smooth rotation in the CCW/CW direction (linear part), followed by a flat plateau (deceleration in the original direction → full stop → acceleration in the reversed direction), and then a smooth rotation in the CW/CCW direction (linear part). The centre point lies central to the plateau region, from which two running windows are set to run outwards. The windows continue moving until 1) the slope of the linear fitting of the points in this window is within σ1 (σ2) of S1 (S2) and 2) the RMSE (root mean square error) of the linear fitting is within the noise profile of a smooth running state.
7. The noise profile of a smooth running state is defined as follows: the same running window goes through the 30 second revolution vs time trace (in total: 30×10 kHz = 300,000 points) and applies linear fitting. The RMSE at each point is used to construct the noise histogram (Figure 5.3.8). The shape of the

histogram deviates slightly from a Gaussian function, with a relatively long tail at large RMSE value, which is contributed by the transient and switching events in the trace. Again, we fit the noise histogram to a Gaussian function (without the long tail part) and define the RMSE value within this Gaussian shape as the noise profile of a smooth running state, which can be attributed to the fluctuations produced by the fundamental stepping mechanism. If the RMSE of the linear fitting of the window at a certain position is higher than the maximum value in the noise profile, we conclude that this position is still within a switching event. The noise profile changes slightly from cell to cell and so we repeat this process on each cell to calculate its own noise profile.

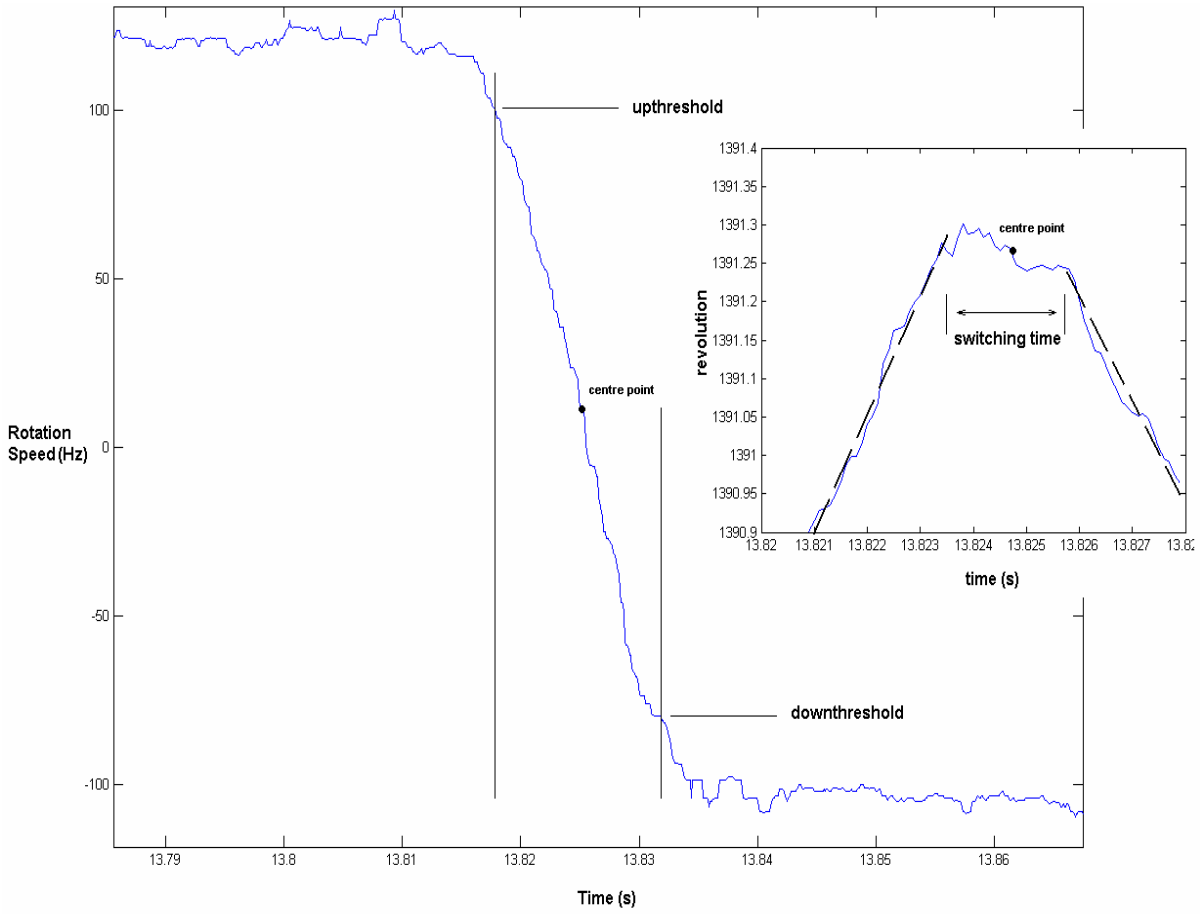

Figure 5.3.7 Our switching time finding program locates switching events from the filtered speed vs. time trace. The raw revolution vs. time trace corresponding to such events were used to measure the switching time.

8. Finally, the distance between the place where the left moving window stops (start point) and right moving window stops (end point) is defined as the switching time. The choice of the window size is important: too small and the window lacks statistical accuracy; too long and it is not sensitive to the local change of slope and RMSE. We use 20 points (2ms) for the window, which gives an accurate measurement compared to the switch time determined by visual examination of the angular record and is robust to variations of ±5 points.
9. In order to ensure that the switching time reflects the activity on the ring, the radius of each switching event is checked again. The radius of the ellipse fitting is used as a criterion of the fitting goodness. In our 'good switching cells', the histogram of the orbit radius exhibits a clear unimodal peak. We fit this peak to a Gaussian function and use one standard deviation from the mean as a radius threshold. In each switching event, we consider the interval 10 points before the start point to 10 points after the end point. If the radii of all the points in this interval are all above the radius threshold, we conclude the bead stays tightly on a circular orbit throughout the switch. The final switching time distributions we present here are all checked by this step.

The final switching time distributions across bias are shown in Figure 5.3.9 a – f.

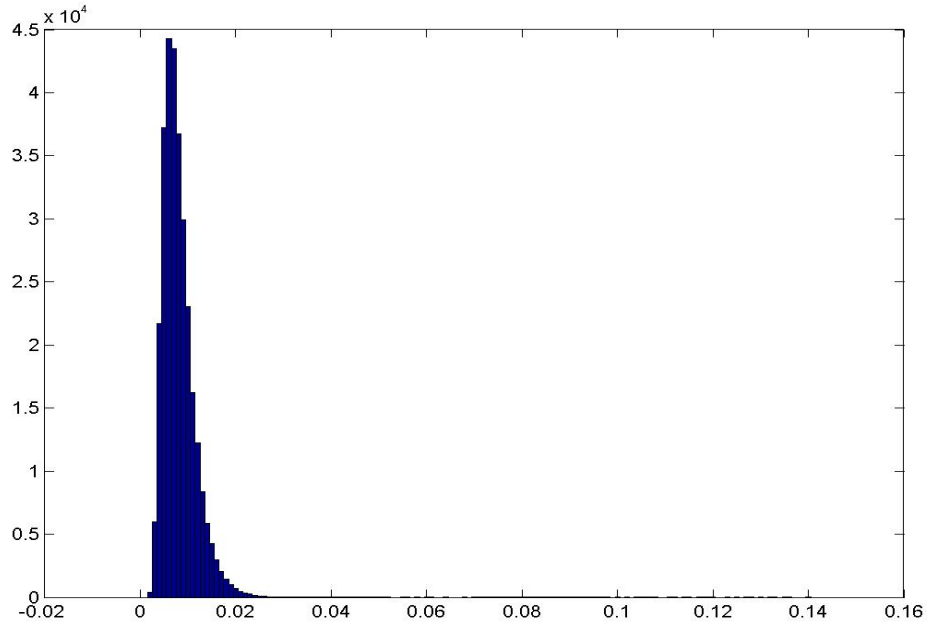

Figure 5.3.8 A typical noise profile generated by step 7 in our switching time finding procedure.

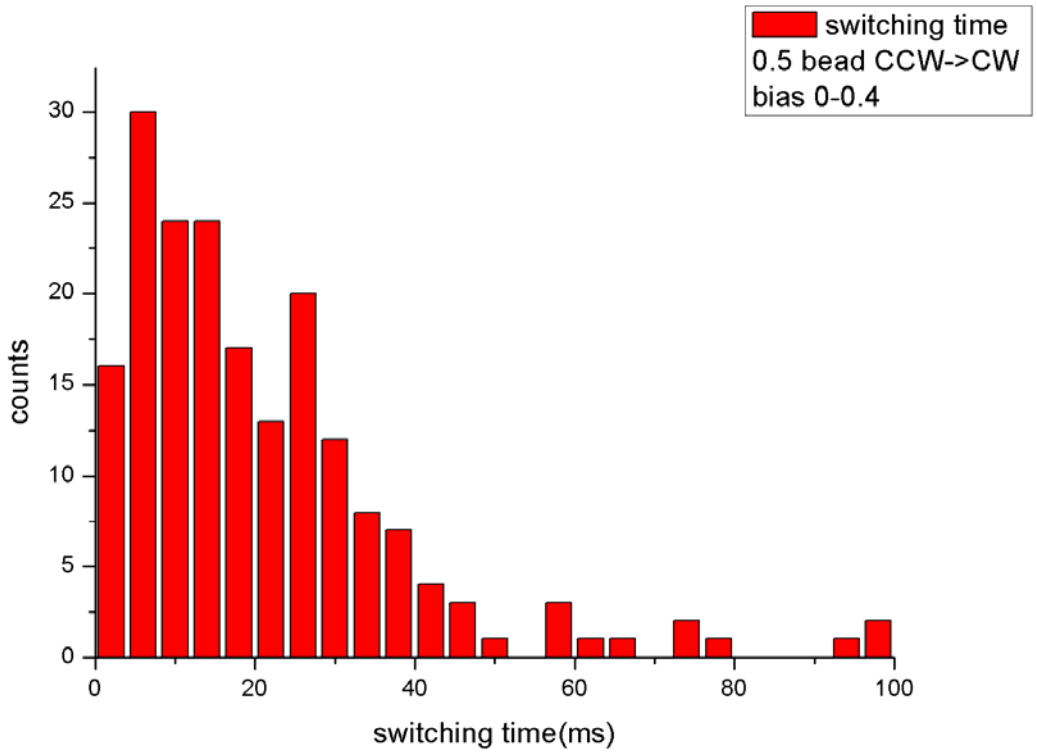

Figure 5.3.9 a Switching time distribution of CCW-CW switches from cells with CCW bias 0-0.4

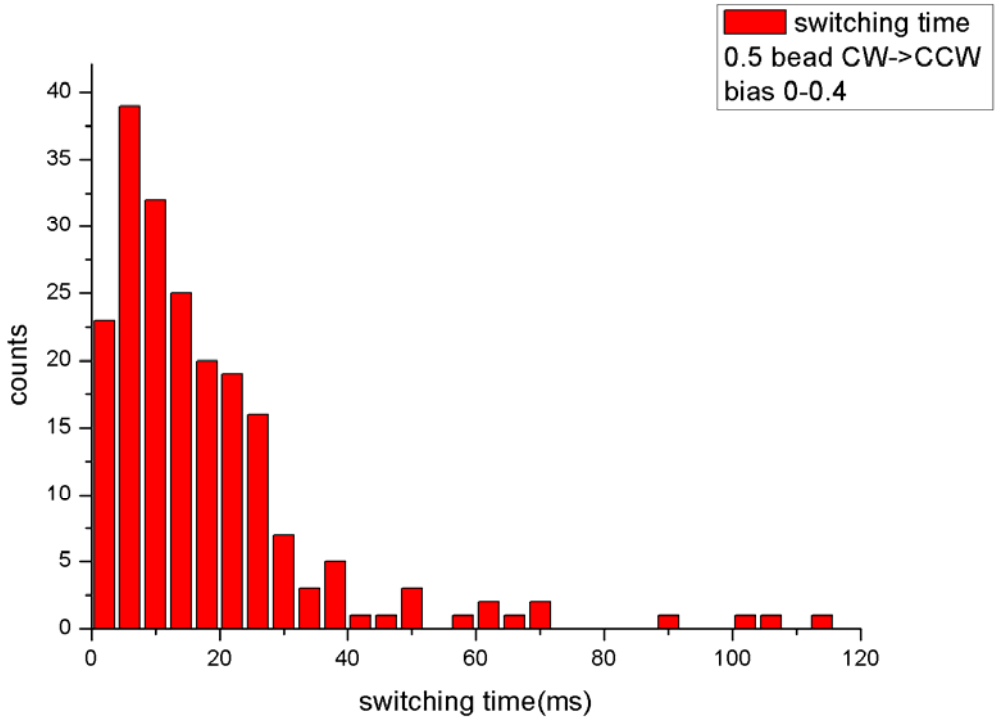

Figure 5.3.9 b Switching time distribution of CW-CCW switches from cells with CCW bias 0-0.4

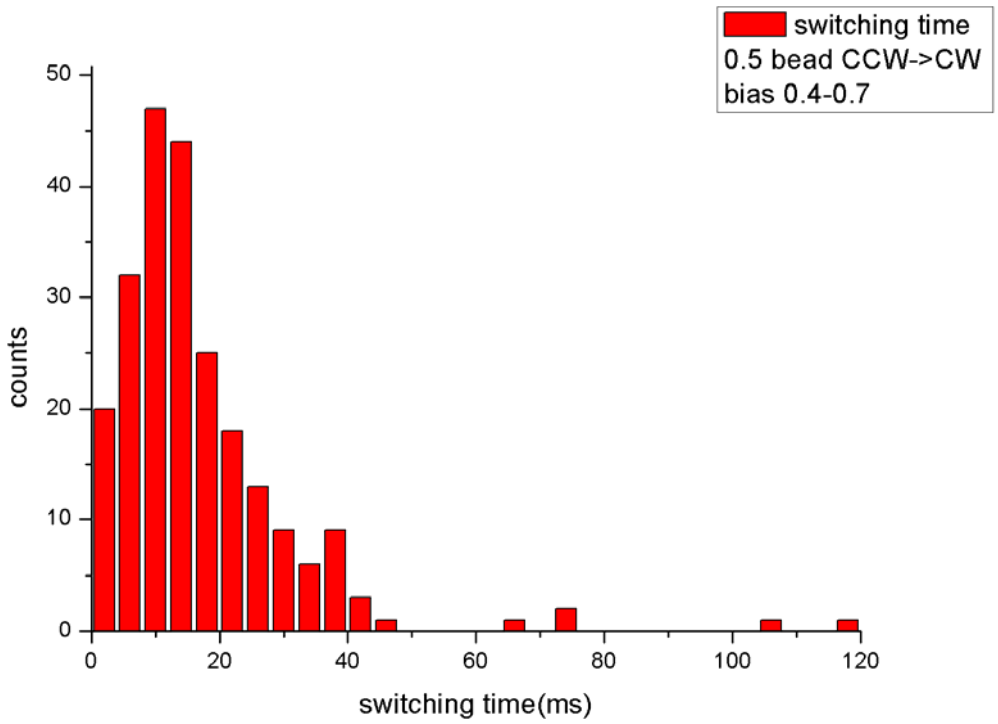

Figure 5.3.9 c Switching time distribution of CCW-CW switches from cells with CCW bias 0.4-0.7

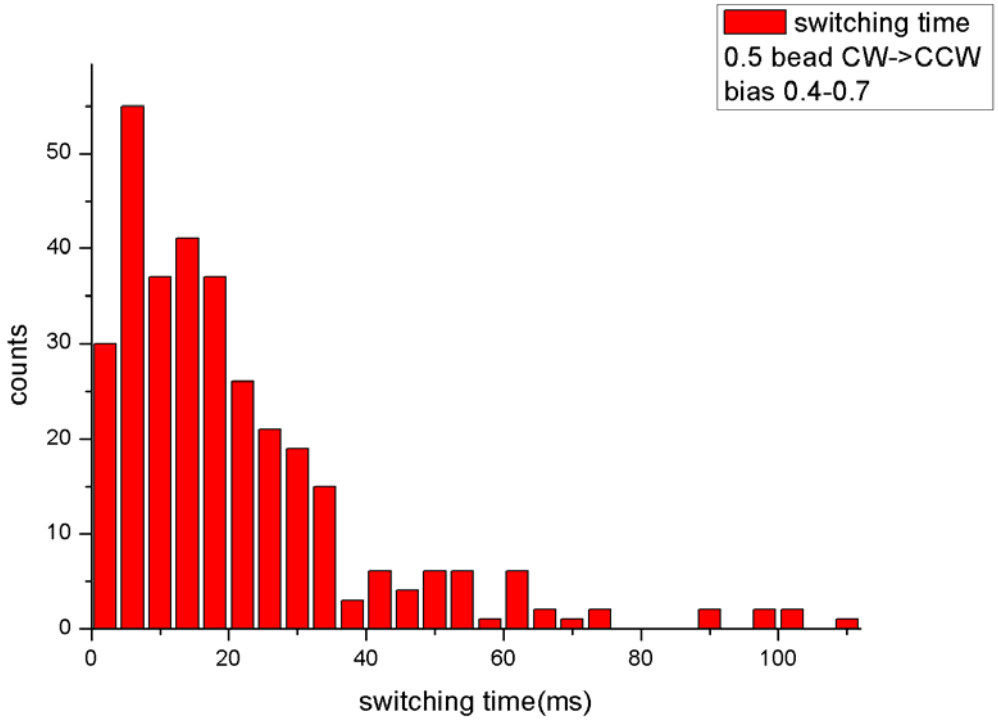

Figure 5.3.9 d Switching time distribution of CW-CCW switches from cells with CCW bias 0.4-0.7

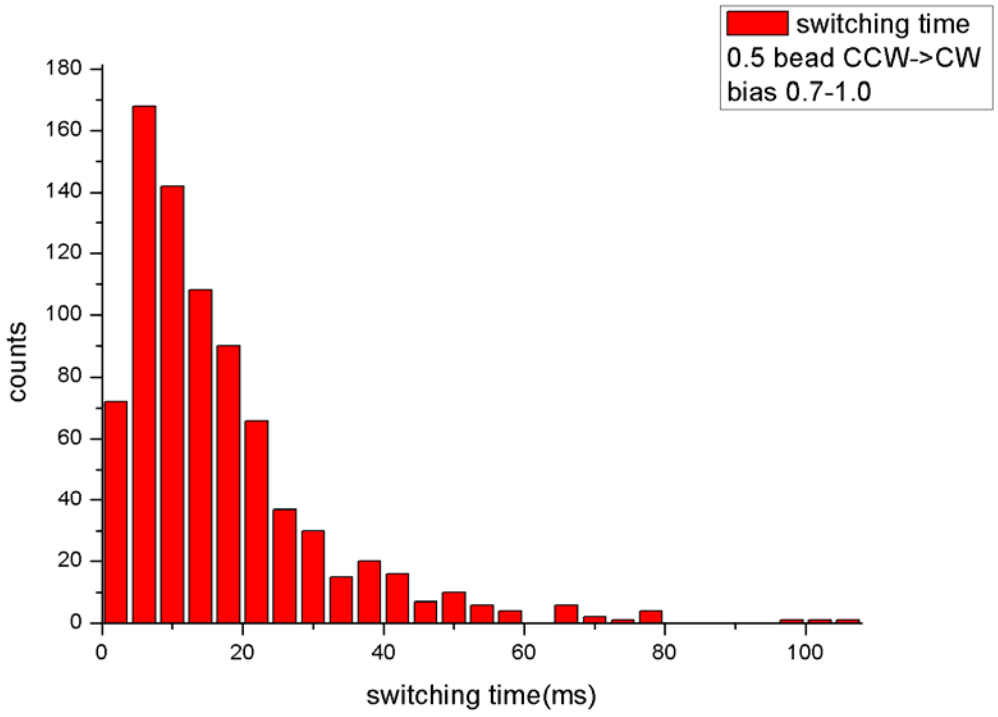

Figure 5.3.9 e Switching time distribution of CCW-CW switches from cells with CCW bias 0.7-1.0

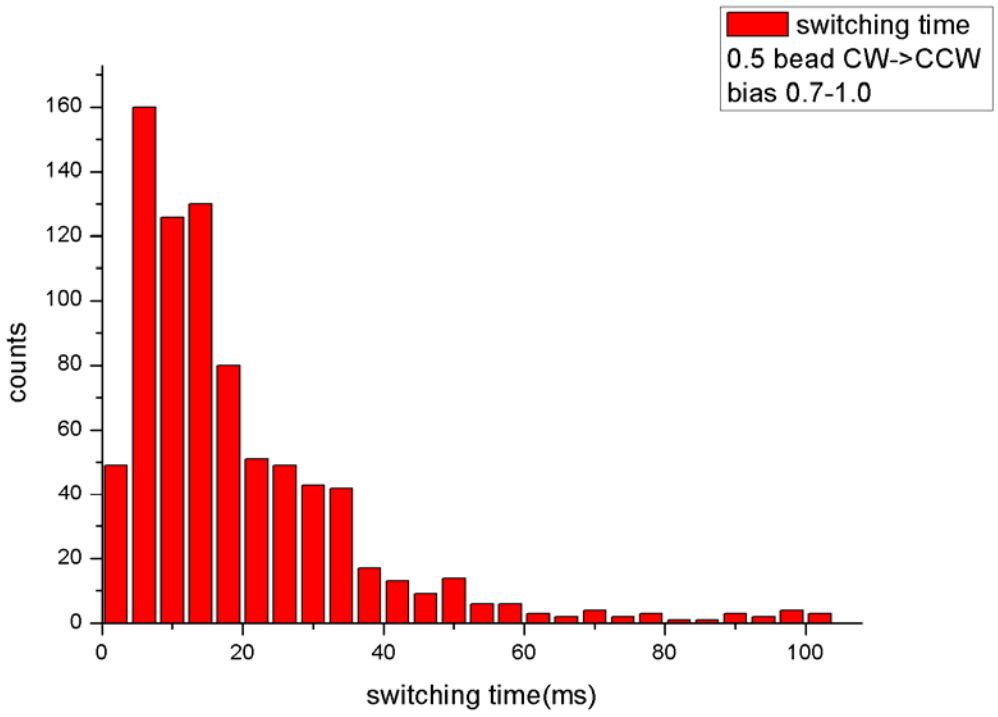

Figure 5.3.9 f Switching time distribution of CW-CCW switches from cells with CCW bias 0.7-1.0

Data for CW-CCW switches and CCW-CW switches were separated out and binned by bias, again to compare the kinetics of cells with different levels of CheY-P activity. We notice that the switching time follows a very broad gamma-shaped distribution with a peak at 4-8ms (statistics of the distributions are listed in Table 3; determined by the Matlab maximum likelihood estimates). Contrary to previous measurements [103], only the fastest switches are less then 1ms in duration. The switch time distribution does not differ with the direction of the switch, nor is it dependant on bias. This result is in agreement with the third prediction of the Ising Allosteric model. However, we need to rule out other possibilities before we draw the conclusion.

Table 3 Experimental switching time distribution statistics

	Gamma distribution parameter a	Gamma distribution parameter b	Peak position (ms)	Mean value (ms)	Standard deviation (ms)
CCW-CW bias 0-0.4	1.5905	13.1547	7.77	20.9221	17.85
CW-CCW bias 0-0.4	1.4240	12.6035	6.34	17.95	17.91
CCW-CW bias 0.4-0.7	1.9128	8.8354	8.06	16.90	14.57
CW-CCW bias 0.4-0.7	1.4645	14.3019	6.64	20.95	18.97
CCW-CW bias 0.7-1.0	1.8590	8.8880	7.63	16.52	14.51
CW-CCW bias 0.7-1.0	1.6883	11.8493	8.16	20.01	17.04

In our experiment, the switching time is observed through the response of a bead attached to the hook/flagellum. The flexibility in the hook/flagellum may lead to an observable switching time even it takes no time to switch on the rotor. We carried out a theoretical simulation to investigate this possibility. We used the same Langevin simulation as in section 5.2.2, but rather than the rotor speed being imported from the Ising Allosteric model, we simulated its movement as a 400 steps/ revolution poisson stepper [55] executing instantaneous switches at a fixed frequency. We used the speed we observed in experiments (0.5 μm bead average 120Hz, 0.35 μm bead average 160Hz) as a control parameter of the stepping frequency. The simulation outputs the bead movement vs. time trace (similar to the revolution vs. time trace in our experimental data). We apply the same switching time finding algorithm to the simulated trace and find the switching time distribution due to hook/flagellum/bead

response (the switch occurs instantaneously on the rotor) with a 0.50 μm bead (Figure 5.3.10) and a 0.35 μm bead (Figure 5.3.11).

From this simulated switching time, we can see:

1) The average switching time of a 0.5 μm bead is about 1.5ms and that of a 0.35 μm bead is 0.5 ms (to ensure that our results are not dependant on the hook-bead system response, identical experiments were carried out with a 0.35 μm bead at high CCW bias.). They are too short to account for the switching time we observe in experiment. Furthermore, the distribution of simulated switching time due to rewinding of the hook/flagellum is quite narrow (range 0—5 ms for the 0.5 μm bead data, and range 0—2.5 ms for the 0.35 μm bead data), far from the broad distribution (range 0—100 ms for both the 0.5 μm and 0.35 μm bead data) we observe in experiments. This strongly argues that our results are not an artefact of the hook/flagellum/bead response due to hook/flagellum rewinding, but in fact reflect the speed of conformational spread around the FliG/FliM ring.

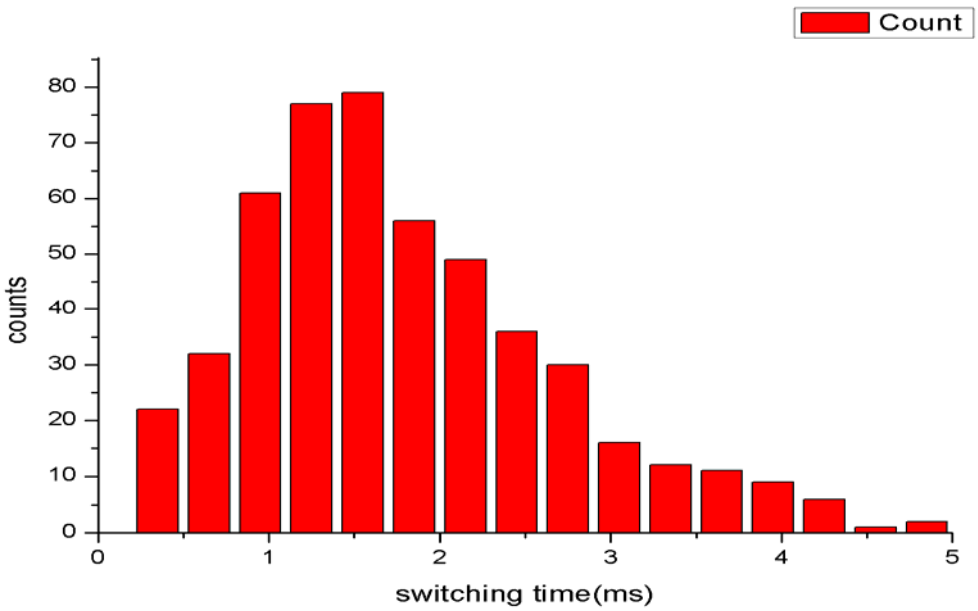

Figure 5.3.10 Simulated switching time of a 0.5 μm bead due to the hook/flagellum/bead response.

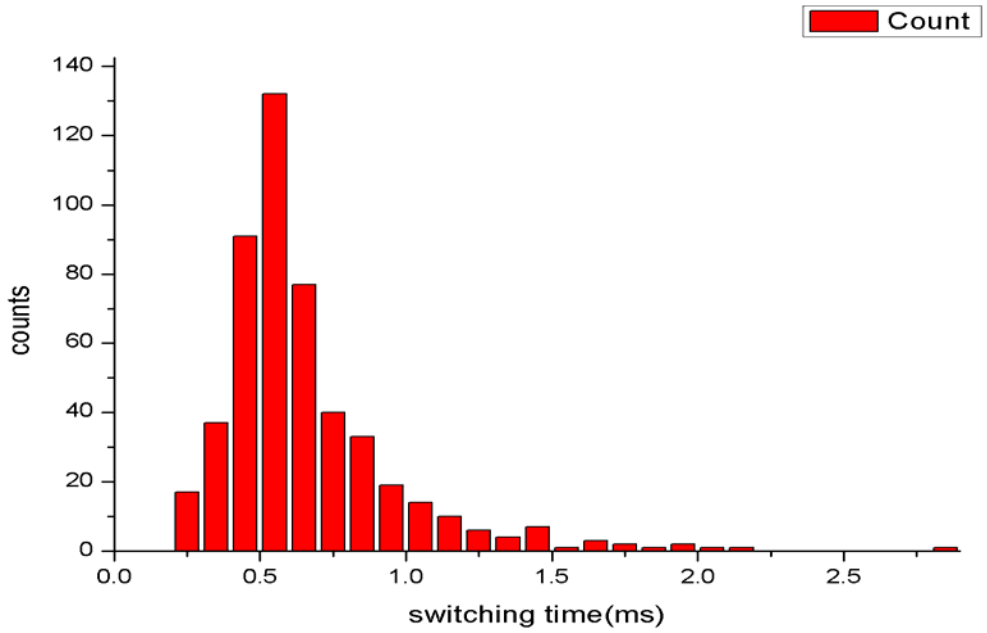

Figure 5.3.11 Simulated switching time of a 0.35 μm bead due to the hook/flagellum/bead response.

2) With our experimental data, we ensured that the switching times we measured were those of switches in which the bead stayed tightly on the circular orbits. Therefore we make the assumption that the experimentally measured switching time is the sum of the hook/flagellum/bead response and the actual time required for conformational spread on the ring. The distribution of times due to conformational spread on the ring, which is our chief interest, can be obtained by taking a deconvolution (Figure 5.3.12) of the hook/flagellum/bead response distribution from the experimental distribution.

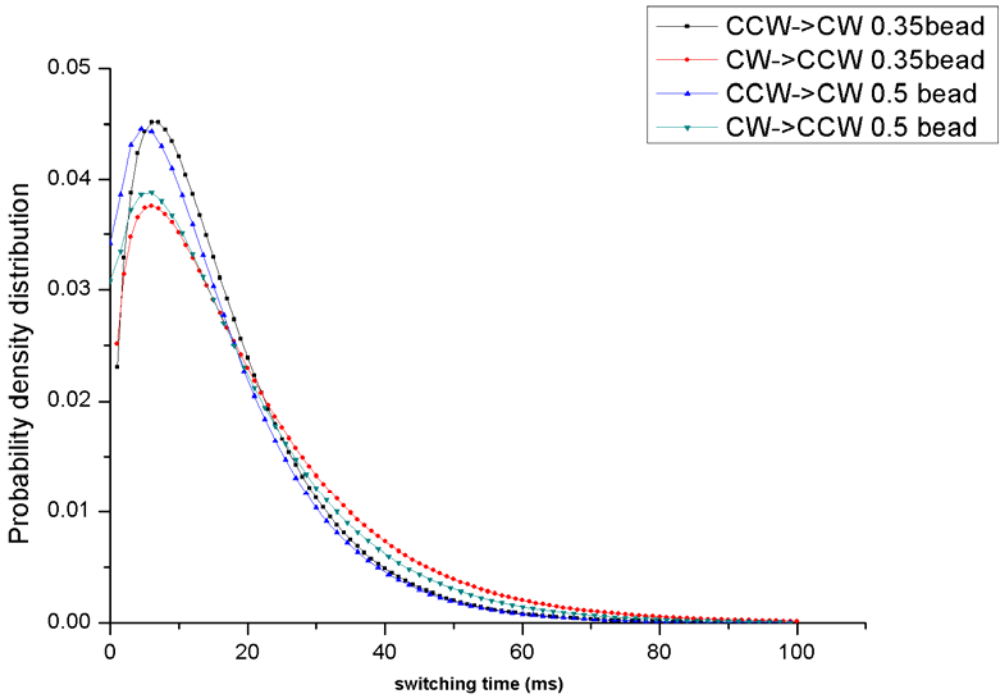

Figure 5.3.12 Deconvolution of the switching time on the rotor from the overall switching time with hook/flagellum/bead response.

In Figure 5.3.12 we perform a deconvolution between gamma fitted experimental data (from the bias bin 0.7-1.0) and the gamma fitted hook/flagellum/bead response distribution, for both the 0.5 μm and 0.35 μm bead datasets. The bias bin 0.7-1.0 was chosen because this provides the largest data set and gamma fitting was carried out with the maximum likelihood method. A peak is well retained in the deconvoluted distribution and the position of the peak does not differ between switching directions or bead sizes. This argues again our experiment has resolved the switching time due to conformational spread on the ring and is independent of the hook/flagellum/bead system.

Based on the two points above, it is reasonable to conclude that the switching time distribution we measured in our experiments reflect the time needed for a conformational spread on the ring and confirms the third prediction of the Ising Allosteric model.

5.4 COMPARISON TO THE MODEL

The three experimental results presented in section 5.3 confirm the three predictions of the Ising Allosteric model. Transient events are representative of the rapid, incomplete growth and shrinkage of domains of opposite conformation. Typically, the growth of a single domain is responsible for encompassing the ring, as opposed to two or more domains in concert. The nucleation of these domains is a Poisson process. Conformational spread in the switch complex is required to convert all subunits from one state to the other, and this spread is necessarily finite in duration. The duration is broadly distributed in magnitude due to stochasticity in the spread.

In order to reproduce the experimental results, we did a thorough search in the model's parameter space. For a certain parameter set, we ran the Langevin simulation introduced in section 5.2.2 to translate the ring activity predicted by the Ising Allosteric model to simulated speed vs. time and angle vs. time records. Later the same analysis method we used to analyze experimental data was applied to the simulated data to find out the switching interval distribution and switching time distribution. Finally, we determined a parameter set of the Ising Allosteric model that can quantitatively reproduce the results from our experiments (Figure 5.4.1, Figure 5.4.2, Figure 5.4.3).

$E_A = 1 k_B T$

$E_J = 4.2 k_B T$

Flipping rate of each FliM/FliG subunit $k = 1.0 \times 10^5 / s$

the binding rate of CheY-P k_{on} = 30 Hz (k_{off} is used as a controlling parameter to produce datasets with different CCW bias)

A more rigorous parameter optimization is now underway and we will present the final results in our formal publication.

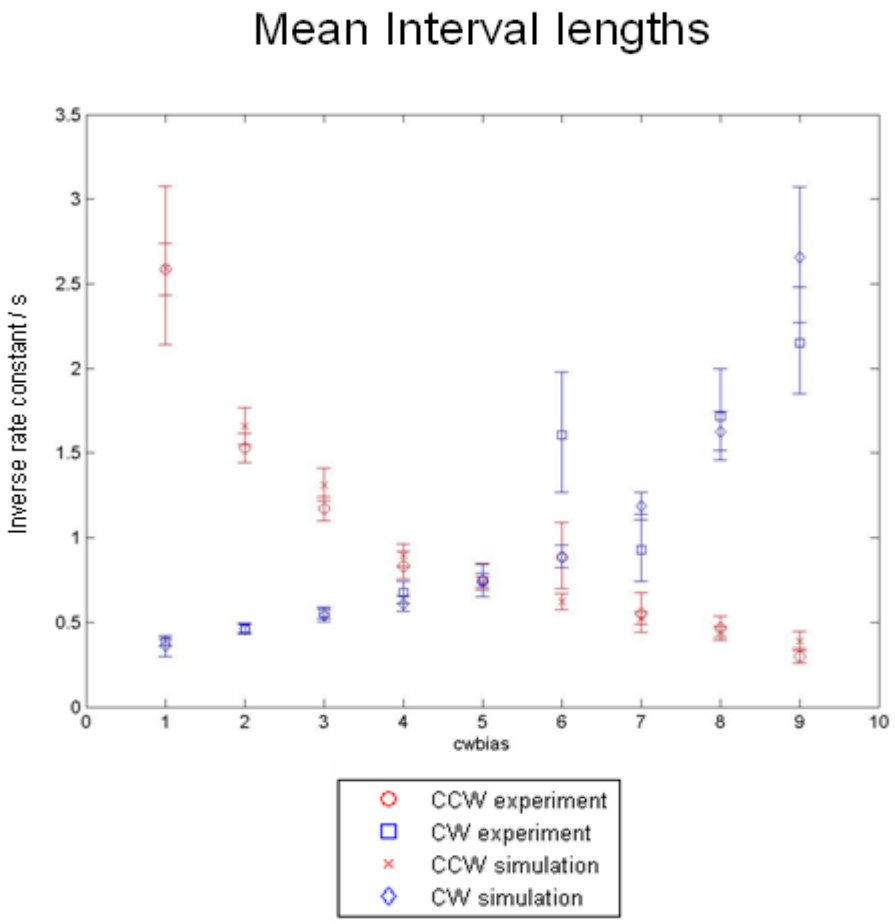

Figure 5.4.1 The Ising Allosteric model can reproduce both the exponential distribution and rate constants for the switching interval distributions.

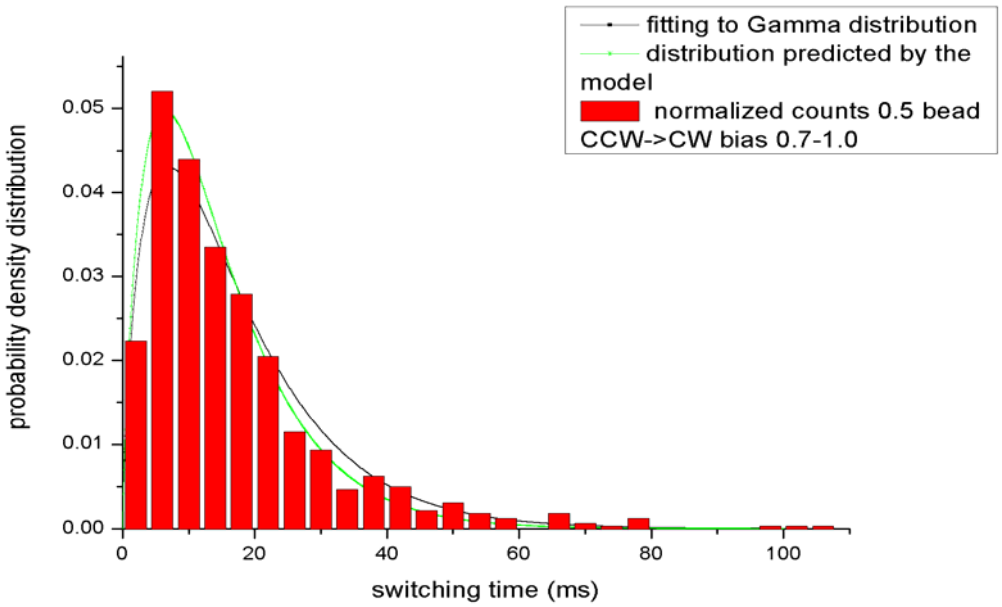

Figure 5.4.2 The Ising Allosteric model can reproduce both the characteristic switching time and the broad distribution of the switching time distribution (CCW-CW CCWbias 0.7-1.0). Gamma parameter a=1.6903 Gamma parameter b=8.6451 peak position=5.97 mean value=14.61 standard deviation=12.47

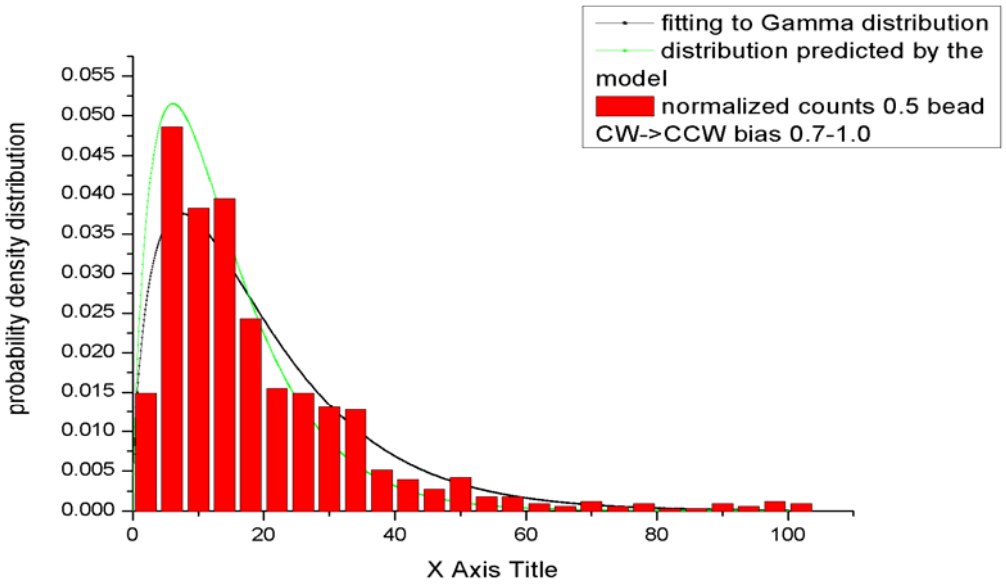

Figure 5.4.3 The Ising Allosteric model can reproduce both the characteristic switching time and the broad distribution of the switching time distribution (CW-CCW CCWbias 0.7-1.0). Gamma parameter a=1.4172 Gamma parameter b=12.0923 peak position=5.04 mean value=17.14 standard deviation=15.57

5.5 CONCLUSION

In this chapter, the Ising Allosteric model, which is a general approach to protein allostery, was reviewed and modified to explain the switching ultrasensitivity of the BFM. The model predicts three phenomena in the dynamics of bacterial switching. They are all confirmed by our experiments.

This work has completed the chemotactic amplification pathway and more importantly, the BFM has been used as a test-bed for a general model for protein-protein cooperative interaction. This has great importance from a systems biology perspective. The Ising Allosteric model (especially the idea of conformational spread) sheds light on information propagation in large protein complexes. In addition to the canonical MWC and KNF models, it provides a new approach to allostery.

CHAPTER 6

Stoichiometry and Turnover in Single, Functioning Membrane Protein Complexes: A Mathematical Simulation

Many essential cellular processes are carried out by complex biological machines located in the cell membrane. The bacterial flagellar motor is a large membrane-spanning protein complex. Within the motor, MotB is a part of the stator that couples ion flow to torque generation and anchors the stator to the cell wall. Mark Leake *et al*. measured the number and dynamics of MotB molecules labelled with green fluorescent protein (GFP–MotB) in the motor by total internal reflection fluorescence microscopy. Counting fluorophores by the stepwise photobleaching of single GFP molecules showed that each motor contains ~22 copies of GFP–MotB, consistent with ~11 stators each containing two MotB molecules. They also observed a membrane pool of ~200 GFP–MotB molecules diffusing at ~0.008 $\mu m^2 s^{-1}$. Fluorescence recovery after photobleaching and fluorescence loss in photobleaching showed turnover of GFP–MotB between the membrane pool and motor with a rate constant of the order of 0.04 s^{-1}: the dwell time of a given stator in the motor is only ~ 0.5 min.

In this chapter, my contribution to this work, a mathematical simulation of the system which determines several key parameters, is presented. More details of the experiments can be found in our publication [104]:

Leake MC, Chandler JH, Wadhams GH, Bai F, Berry RM and Armitage JP. *Nature* 443, 355-358 (2006).

Here I acknowledge the contributions from Mark Leake, Jennifer Chandler, George Wadhams, Richard Berry and Judy Armitage.

6.1 BRIEF INTRODUCTION TO THE EXPERIMENTS AND RESULTS

TIRFM (Total Internal Reflection Fluorescence Microscopy) is a standard technique that is widely used for *in vivo* imaging. Total internal reflection is a well known optical phenomenon which occurs when light travels from a dense medium to a less dense medium (lower refractive index). The critical angle is defined as:

$$\theta_c = \sin^{-1}\left(\frac{n_1}{n_2}\right) \qquad n_1, n_2 \text{ the refractive indices of the two mediums} \qquad \text{formula (6.1)}$$

If the angle of incidence is above the critical angle, all of the light is reflected. However, some of the energy of the beam still propagates to the less dense medium in the form of an evanescent wave. The strength of the wave decays exponentially with the distance into the medium, which normally survives a few hundred nanometres. Within this distance, a fluorophore molecule can absorb photons and be excited. Therefore this provides a good way of achieving fluorescence with a very low background of excitation light. In Leake *et al.*'s experiment, TIRFM is implemented to investigate the stoichiometry and turnover of the GFP labelled MotB complex in the membrane. A schematic plot of the experimental setup is presented in Figure 6.1.1

(a) and in Figure 6.1.1 (b) key structural components of the bacterial flagellar motor are shown.

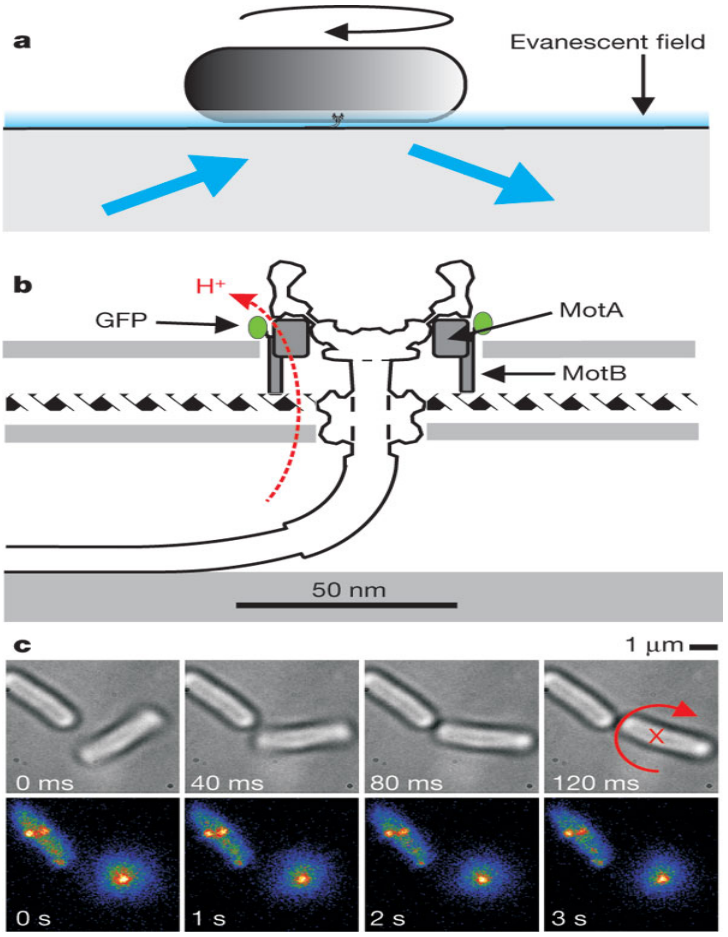

Figure 6.1.1 TIRF microscopy of live GFP–MotB cells.
(a) Antibody-tethered cell rotation assay. (b) Expansion of the motor structure (c) Consecutive brightfield (top) and TIRF (bottom) images showing a rotating tethered GFP–MotB cell and a nearby stuck cell. Two motor spots are visible in the stuck cell, whereas one is visible at the centre of rotation in the tethered cell.

Under TIRF illumination, a bright spot can be observed at the base of the flagellum, indicating a ring of GFP-MotB molecules anchored around the periphery of the 50nm diameter rotor. Continuous photobleaching of 400nm square regions of interest (ROI) containing a single motor show steps in intensity at roughly integer multiples of a unitary level, I_{GFP}, consistent with photobleaching of individual GFP molecules (experimental photobleaching traces are shown in Figure 6.1.2 a). The Chung-Kennedy filter (a robust step finder) was applied to these traces (Figure 6.1.2 b), making the steps easier to track. The pairwise-distance distribution function (PDDF) was constructed from these filtered traces and its power spectrum was

calculated (Figure 6.1.2 c, d). The peak in the power spectrum indicates a unitary step size of $I_{GFP} \approx$ 5370 counts.

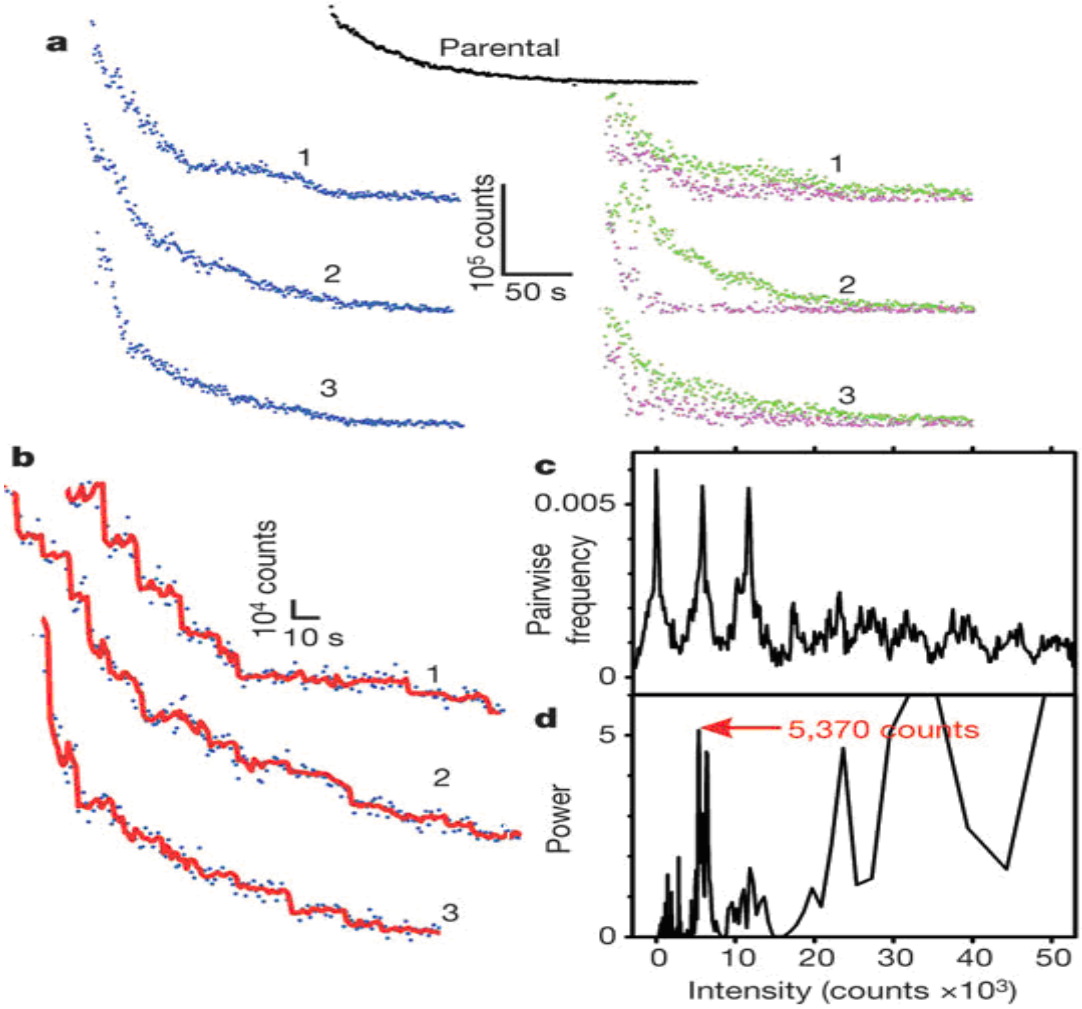

Figure 6.1.2 TIRF photobleaching. (a) Three photobleaches for regions centred on motors, showing total (blue), motor (magenta) and background (green) intensities, and average autofluorescence (black) from 32 parental cells lacking GFP. (b) Expansions from traces in (a) with Chung–Kennedy filtered traces overlaid (red). PDDF (c) and power spectrum of the PDDF (d) for filtered intensity curve 3 in (a); the unitary peak is indicated (arrow).

We can estimate the total number of GFP–MotB molecules per motor by dividing the initial motor intensities I_0^m by I_{GFP} for each trace from different cells. This gives 22 ± 6 GFP-MotB per motor. Separation of the total intensity into motor and background components gives us the initial membrane value. Dividing this initial membrane intensity by I_{GFP} gives an average of 0.052 ± 0.022 molecules per pixel.

The cell-surface area is estimated as 3,700 ± 500 pixels; thus, the total number of non-motor GFP–MotB molecules per cell is around 190 ± 80.

Fluorescence Recovery after photobleaching (FRAP) and Fluorescence Loss in photobleaching (FLIP) methods were used to determine the protein turnover rate between membrane and motor components. In these experiments, 0.5 s focused laser exposure photobleaches all fluorophores in width of ~1 mm regions. Figure 6.1.3 a shows TIRF images of a cell before and after bleaching of a region containing a motor. Fluorescence recovery (FRAP) of both motor and background components in the bleached region is visible, as is fluorescence loss ('one-shot' FLIP) at the other end of the cell. FRAP and FLIP (Figure 6.1.3 b) of motor and membrane components respectively, averaged over 13–38 cells, are shown in Figure 6.1.3 c and d.

The FRAP and FLIP data reveals that free GFP-MotB molecules are diffusing on the membrane and rapidly exchanging with the anchored functioning GFP-MotB in the motor. The main purpose of the following mathematical modeling is to derive the diffusing coefficient of GFP-MotB and rate constant of this dynamic exchange.

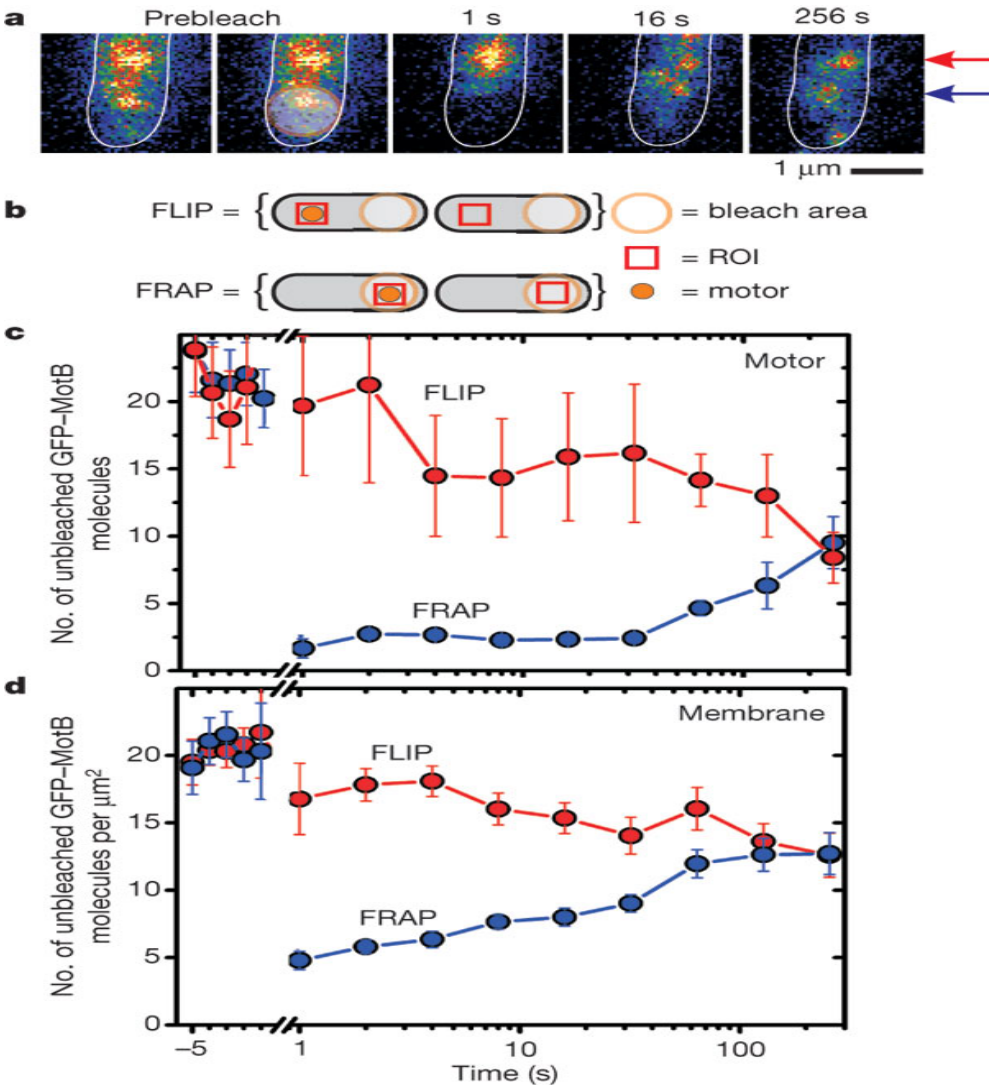

Figure 6.1.3 Focused laser FRAP and 'one-shot' FLIP. (a) Successive TIRF images of a GFP–MotB cell before and after bleaching. The prebleach images are identical; the laser focus is indicated (circle, right panel). Arrows indicate positions of two motors, showing FLIP (red) and FRAP (blue); the cell is outlined (white). (b) Representation of FLIP and FRAP using ROIs with and without motors. Mean numbers of unbleached GFP–MotB molecules in motor (c) and membrane (d) components versus time. Data points were an average of 13 (motor, FLIP), 30 (motor, FRAP) and 38 (membrane) ROIs. Error bars indicate 1 s.d.

6.2 ESTIMATING THE DIFFUSION COEFFICIENT: COMPARISON WITH SIMULATIONS

We constructed a custom MATLAB program to simulate the two-dimensional diffusion of GFP-MotB molecules over the cell surface, modeling the cell as a

cylinder of length 2 μm and diameter 1 μm capped with hemispherical ends. We assumed each cell contained ~200 GFP-MotB molecules in total (as per our experimental estimation), initially randomly distributed over the total surface area. A region for the focused laser bleach was assigned on the long-axis of the cell, either in the middle or displaced 0.5-1.0 μm from the middle towards one of the poles. The photobleach probability in this region was modelled as a normalized symmetrical two-dimensional radial Gaussian function of width ~1 μm, and each molecule was polled to determine whether it was photobleached or not. In each subsequent small time interval Δt (100ms) after the bleach we assumed each molecule to move a small distance $(4D\Delta t)^{1/2}$ in a random direction in the membrane, where D was a trial two-dimensional diffusion coefficient. We tracked the positions of all molecules during time intervals over a range of 1 to 256 s to match experimental data.

To calculate the predicted TIRF image intensity from the positions of fluorescent molecules in the membrane we performed the following procedure:

1. We assigned a brightness to each unbleached molecule equal to the TIRF evanescent field weighting function of exp(-z/d), where z was the relevant height of each molecule at a given time point and d was the characteristic 1/e field depth, 100 nm.

2. We approximated the intensity profile of each unbleached molecule by a symmetric two-dimensional Gaussian of width 240 nm. This ignores the effect of de-focusing on the point-spread-function, which in practice will be very small as all visible molecules are close to the focal plane defined by the coverslip and TIRF illumination field.

3. We then binned the final intensity patterns into a two-dimensional pixel grid (50x50 nm per pixel), with the contribution from each molecule given by the weighted intensity (from steps 1 and 2 above) at the centre of the pixel.

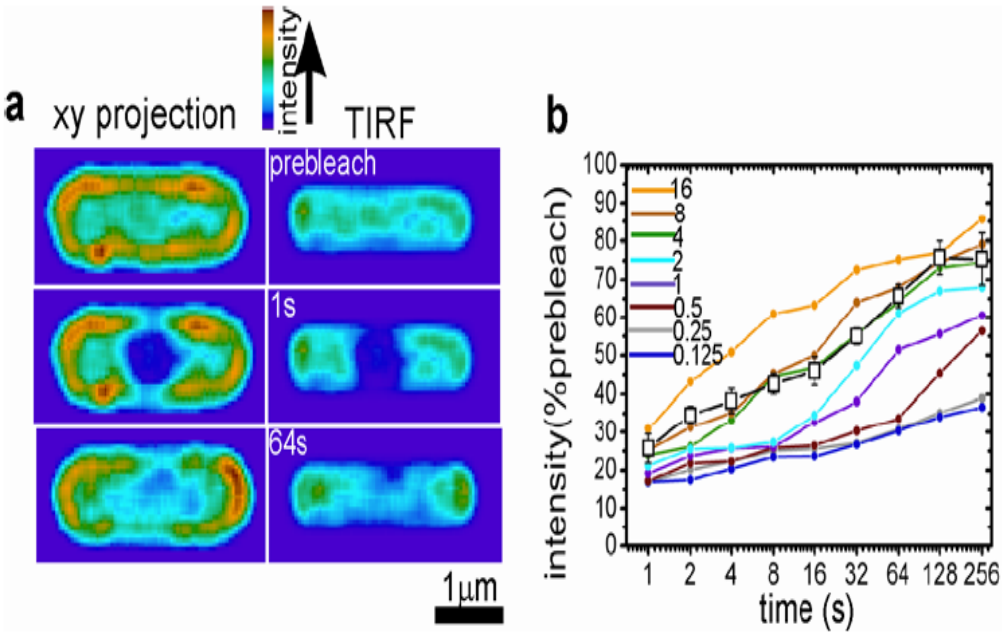

Figure 6.2.1 Estimating the diffusion coefficient in the membrane by comparison with simulation. (a**)** x-y projections and TIRF images (averages of 10 simulations) before and after focussed bleaching of the centre of the cell, D=1×10^{-3} μm^{2} s^{-1}. (b**)** Intensity in ROI centred on laser focus *vs.* time postbleach. Simulated traces (coloured) for values of D in range (0.125 to 16)×10^{-3} μm^{2} s^{-1} and experimental data (black squares) from FRAP data of membrane in non-motor regions (averaged from 8 GFP-MotB cells, error bars one s.d.)

We simulated a series of D values in the range 0.125 to 16 × 10^{-3} μm^{2} s^{-1}, calculating the average TIRF intensity patterns from 10 cells for each. We then analysed the averaged image for each value of D using the same method as for experimental focused laser FRAP and FLIP data, to assess the predicted recovery or loss of fluorescence intensity following photobleaching. By comparing these predictions with the membrane background component in experimental FRAP data for ROIs which contained no putative motor, we obtained an estimate for D at each time point by linear interpolation, and took the average of these estimates as the final estimate of D, 0.0075 ± 0.0013 μm^{2} s^{-1} (mean ± s.d.). This value is smaller than that of the free diffusion fluorophores on cell membrane [105], but in the same order as the diffusion coefficients of larger protein complexes [106-108].

6.3 A GLOBAL MODEL FOR INTENSITY CHANGES IN THE MOTOR AND MEMBRANE

We extended the above diffusion model to include stator GFP-MotB photobleaching and stator exchange between free GFP-MotB and the motor. This allows us to estimate the rate of exchange with the motor and to verify our interpretations of the TIRF photobleach traces (Figure 6.1.2) and FRAP and FLIP data (Figure 6.1.3). The model was implemented in MATLAB as follows:

1. Diffusion of stator units, each containing 2 MotB molecules was simulated as before, assuming a total of ~200 GFP-MotB molecules randomly dispersed in the cell membrane and a diffusion coefficient D = 0.0075 μm^2 s^{-1} (values based on experimental estimates).

2. A motor was located centrally on the 'lower' surface of the cylinder (defined as that closest to the TIRF excitation field) as was typical of the experimental assays, initially containing 11 stator units (based on experimental estimate).

3. The exchange process was modelled by the standard diffusion-capture method. In every time interval Δt each stator unit attached to the motor either disassociated from the motor or remained bound according to a predefined rate k_d (a free parameter in the program later optimized to actual experimental data): if the unbinding probability, $k_d \Delta t$, was greater than a pseudo-random number in the range 0-1, the unit dissociated, otherwise it remained bound. A small circular region of radius 100 nm centred on the motor was defined as the motor capture zone i.e. a radius ~4 times larger than that of the motor itself (~25 nm). Any free membrane stator units found in this area were polled as above against either binding to the motor or remaining free, according to a predefined rate k_a. We defined $k_a = k_d \exp(f(11-Ns))$, where Ns is the number of stators in the motor at the moment of polling and f a number (we used f = 5) tuning

the strength of the exponential factor. This formula ensures that $k_a = k_d$ when Ns = 11, and leads to a stable equilibrium number of stators per motor close to the experimentally estimated number. The underlying physical meaning is that the binding rate is reduced as available binding sites on the motor are occupied and enhanced when there are plenty of empty sites on the motor. We monitor the position of each stator at each time point as well as the bleach state of its GFP molecules and whether it is free or motor-bound.

4. On top of the main code two sub-routines were added, one responsible for bleaching the GFP-MotB in a pre-defined area and the other for predicting, as before, the observed fluorescence intensity within a 0.4x0.4 μm^2 region of interest centred on the motor. For simulations of FLIP and FRAP the bleaching areas were tried in the range 1-2 μm^2 to reflect the size of the focused laser spot (the largest area tried bleaching ~50% of the total membrane GFP-MotB content in the cell), centred either on the motor (FRAP) or displaced ~1 μm from the motor (FLIP). We assumed that the initial focused laser spot irreversibly photobleaches a similar quantity of GFP molecules in this area as per the first experimental post-bleach timepoint, on both the lower and upper membranes. For simulations of continuous TIRF bleaching two different bleaching areas were tried; either ~0.6x3.0 μm^2 centred on the motor (the "TIRF bleach-zone", close to that expected for an excitation field of depth ~100 nm) or the entire lower half of the cell surface (the "extended bleach-zone", modeling possible scattering of the illuminating light beyond the TIRF field). In each time-step, each un-bleached molecule in the bleach-zone was deemed to have bleached if the probability, $\Delta t/t_0$ (where t_0 = 40 s, the experimentally estimated bleach time), was greater than a pseudo-random number in the range 0-1; otherwise it remained un-bleached.

6.4 ESTIMATING DISSOCIATION RATES BY REPRODUCING FRAP AND FLIP EXPERIMENTS

The extended model was simulated with values of k_d equal to 0.01, 0.02, 0.03, 0.04, 0.05, 0.06, 0.07 and 0.09 s^{-1} in bleach-zones corresponding to FRAP and FLIP experiments. For each value of k_d, mean FRAP and FLIP traces for motor and membrane components were obtained by averaging 500 simulations each lasting 300 s (Figure 6.4.1 colour traces). These simulated data-sets were compared to the experimental data-set.

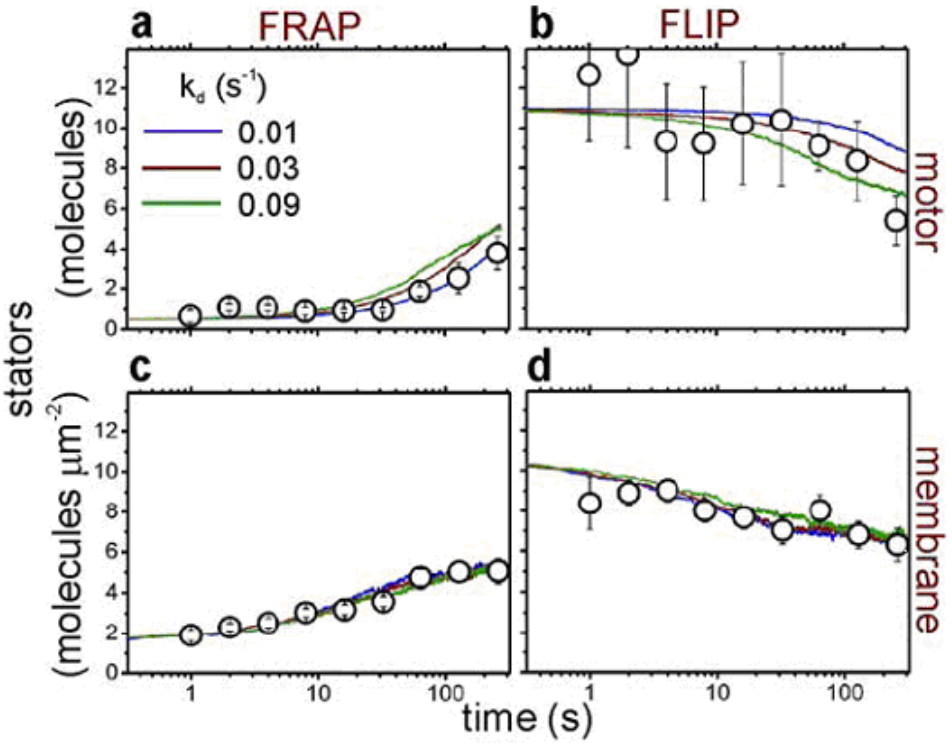

Figure 6.4.1 Simulations for FRAP and FLIP. Predictions for the FRAP experiment on the motor and membrane components (a,c), and similarly for FLIP (b,d) at different k_d (showing only three values for clarity). The experimental data, scaled by the re-normalization coefficients gave the best fit for $k_d = 0.04\ s^{-1}$, are overlaid (white circles, s.d error bars).

An error function indicating the goodness of fitting is formed (see reference [93] for details). The minimized value of this error function is found for approximately $k_d = 0.04 \pm 0.02\ s^{-1}$.

We also investigated the effects of having more than one motor in the cell. Placing three motors randomly within the original bleach spot resulted in no net change in the steady-state value for number of unbleached stators bound to the motor under observation, but did reduce the net total binding rate for unbleached stators at equivalent time points compared to the single-motor system by ~5%; adding more bleached motors into the system marginally increases the effective mixing time for bleached and unbleached stators in the membrane.

6.5 Conclusion

In this chapter, we have developed a mathematical model to mimic the diffusion and dynamic exchange of GFP labelled MotB molecules on the cell membrane. With comparison to the experimental data, this model identifies several key parameters and highlights valuable insights into the BFM system. Again, it demonstrates the intimate collaboration between theory and experiment.

APPENDIX

The Langevin simulation code we used to generate results in Chapter 3 and Chapter 4.

```
      Program main
c a Langevin simulation code for BFM
c The coordinates are in the order: stator, rotor, load
c time delay added
      implicit none
      integer debug
      parameter (debug=0)
      real*8 kBT, onepi,dt,t,kBT0
c temperature * Boltzman's constant
      parameter(kBT = 4.0807d0)
      parameter (kBT0 = 4.1d0)
      parameter(onepi = 3.1415926d0)
      integer nstep, nsamp, nequil,istep,neq0
      integer nfree,maxnts,nstator
c number of stators
      parameter(nstator = 8)
c       parameter(ndof=nstator+1)
c number of degrees of freedom
      parameter(nfree = nstator+2)
c the maximum number of chemical transitions per stator
      parameter(maxnts = 1)
c the chemical rates
      real*8 C_P, C_C,pKa,kprefactor
      real*8 krate(maxnts*nstator),R(maxnts+2),sumrate,
     &      krate12,krate21,maxkrate
      real*8 Dcnst(nfree),sqDt(nfree),DTt(nfree)
c       integer ns(nfree)
c the spring constants
      real*8 kappa(2)
c the equilibrium stator positions
      real*8 thetaS0(nstator),thetaS00(nstator),
     &     dF(nfree),V1,V2,dv1,dv2,dV,
     &     torLR,thetaS,deltheta,deltheta2

c time step
```

```
      parameter(dt = 1.0d-10)
c total number of steps
      parameter(nstep =  1000000000)
c sampling the trajectory per nsamp steps
      parameter(nsamp =  500000000)
c the number of steps to equilibrate the system before sampling
      parameter(nequil = 1000000000)
      real*8 ran1,randnum,randnum1,randnum2
      integer idum,i,j,icount,icount2
c positioN
      real*8 xi,ti,xold,xsamp
      real*8 xt(nfree,nstep/nsamp+1),x(nfree),tsave(nstep/nsamp+1)
      integer sct(nstator,nstep/nsamp+1),sc(nstator)
      real*8 k12p,k12c, k21,kfac1,kfac2
      real*8 ax0,xmin,xmax,Kscalef
      real*8 xleft,height,Lleft,Lright,PMF,vbump,lbump
      real*8 xr2,xr3,xr4
      real*8 tdelay(nstator),taudelay
CCCCCCCCCCCCCCCCCCCCCCCCCCCCCCCCCCCCCCCCCCCCCCCCCCCCCCCCCCCCCCCCCCCCCCCCCCCC
CCCCCCCCCCCCCCCCCCCCCCCCCCCCCCCC
c number of trajectories
      integer ntraj,itraj,ipoint,npoint
      parameter(ntraj=10,npoint=6)
      real*8 omega(ntraj,npoint)
      real*8 aveomega(2,npoint)
      real*8 torque(npoint)
      real*8 Dbead(npoint),pmf_s
c       data Dbead/4.d0,
c     &         5.d0/
c,10.d0,30.d0,50.d0,
c     &         100.d0/
           data Dbead/0.1d0,0.5d0,3.d0,
     &         5.d0,7.d0,100.d0/
C       data Dbead/10.d0,30.d0/
c       data pmf_s/60.d0,80.d0,105.d0,125.d0,150.d0/
        data pmf_s/120.d0/
c       data thetaS0/0.5d0/
      data thetaS00/0.4620d0, 0.2258d0, 0.6749d0,
     &    0.3663d0, 0.1955d0, 0.0683d0, 0.8295d0, 0.0405d0/
CCCCCCCCCCCCCCCCCCCCCCCCCCCCCCCCCCCCCCCCCCCCCCCCCCCCCCCCCCCCCCCCCCCCCCCCCCCC
CCCCCCCCCCCCCCCCCCCCCCCCCCCCCCCC
      idum = -10
      ax0 = 2.d0*onepi/26.d0
      do i = 1, nstator
        thetaS0(i) = thetaS00(i)*ax0
      enddo
c potential parameters
      xmin = 0.d0*ax0
      xmax = 1.d0*ax0
      Lleft = 0.1d0*ax0
```

```
      Lright = 0.9d0*ax0
      xleft = 0.1d0*ax0
      height = 10.d0*kBT0
      vbump = 15.d0*kBT0
      lbump = 0.1d0*ax0
c windows for chemical reaction
C Keffect function (rectangcle)
      xr2 = 0.1d0*ax0
      xr3 = 0.34d0*ax0
      xr4 = 0.58d0*ax0
      kfac1 = 0.d0
      kfac2 = 1.0d0
c chemical rates 1:occupied 2: empty
      C_P = 1.0d-7
      C_C = 10.0**(-7.6)
      pKa = 10.0**(-14.6)
      kprefactor = 0.4d20
      k12p = C_P*C_P*kprefactor  !proton hops from periplasm
      k12c = C_C*C_C*kprefactor
      k21 =  pKa*kprefactor
      TAUDELAY = 0.0D-6
c spring constants
      kappa(1) = 800.d0*kBT0 ! stator
      kappa(2) = 500.d0 ! rotor-load
c equilibrium stator positions
c       Do i = 1,nstator
c         thetaS0(i) = 2.d0*onepi*(i-1)/nstator
c         thetaS0(i) = ax0*(i-1)/nstator
c       Enddo
c       thetaS0(1) = 0.d0
c       thetaS0(2) = 2.d0*onepi*(2-1)/8.d0
c       thetaS0(3) = 2.d0*onepi*(6-1)/8.d0
      open(unit=1,file='BFMts1c.dat',status='unknown')
      open(unit=2,file='BFMts1b.dat',status='unknown')
      open(unit=10,file='BFM1.dat',status='unknown')
      open(unit=11,file='BFM2.dat',status='unknown')
Ccccccccccccccccccccccccccccccccccccccccccccccccccccccccc
      Do 300 ipoint=1,npoint
        pmf = pmf_s*1.0d-3*160.2d0
c initial position
          Do i = 1,nstator
            x(i) = thetaS0(i)
          Enddo
          x(nstator+1) = -0.d0*ax0
          x(nstator+2) = -0.d0*ax0
c initial chemical states
          Do i = 1,nstator
            sc(i) = 1
          Enddo
c diffusion constant
```

```
      do i = 1,nstator
        Dcnst(i) = 500.d0*kBT/kBT0
      enddo
      Dcnst(nstator+1) = kBT/2.0d-4
      Dcnst(nstator+2) = Dbead(ipoint)
      Do i = 1,nfree
        sqDt(i) = dsqrt(2.d0*Dcnst(i)*dt)
        DTt(i) = Dcnst(i)/kBT*dt
      Enddo
      t=0.d0
      Do 200 itraj = 1,ntraj
        if(itraj.eq.1)then
          neq0 = nequil
        else
          neq0 = 500000
        endif
        do i = 1,nstator
          tdelay(i) = 0.d0
        enddo
        icount = 1
        icount2 = 1
c now starts the trajectory propagation
      xsamp = 0.5d0*onepi
      do 100 istep = 1,nstep+neq0
        if(debug.eq.1)then
          x(nstator+1) = (istep-1)*ax0/1000.d0
          do i=1,nstator
            sc(i) = 1
          enddo
        endif
ccccccccccccccccccccccccccccccccccccccccccccc
c calculate the potential and gradient
ccccccccccccccccccccccccccccccccccccccccccccc
        Do j = 1,nfree
          dF(j) = 0.d0
        Enddo
c in the case of no stator spring
        Do i = 1,nstator
          x(i) = thetaS0(i)
        Enddo
        Do j = 1,nstator
          thetaS = x(j) !the stator position
          deltheta = x(nstator+1) - x(j)
          deltheta = deltheta - int(deltheta/ax0)*ax0
          if(deltheta.gt.ax0)then !scale back to [0,1]*ax0
            deltheta = deltheta-ax0
          elseif(deltheta.lt.0*ax0)then
            deltheta = deltheta + ax0
          endif
ccccccccccccccccccccccccccccccccccccccccccccccccccccccccccccccccccccc
```

```
c here the potentials are calculated
ccccccCccccccccccccccccccccccccccccccccccccccccccccccccccccc
           if(deltheta.lt.xleft)then
              V1 =  height/Lleft * (deltheta-xmin)
              dV1 = height/Lleft
           else
              V1 = height - height/Lright * (deltheta - xleft)
              dV1 = -height/Lright
           endif
          if(deltheta.gt.(xleft-lbump) .and. deltheta.le.xleft)then
              V1 = V1 + vbump/lbump *(deltheta-xleft+lbump)
              dV1 = dV1 + vbump/lbump
          elseif(deltheta.gt.xleft .and.
     &         deltheta.le.(xleft+lbump))then
              V1 = V1 + vbump/lbump* (xleft-deltheta) + vbump
              dV1 = dV1 - vbump/lbump
          endif
          deltheta2 = deltheta + 0.5d0*ax0 ! we shift the coordinate
                        !so treating window 1(3) and state 1 is much easier
          if(deltheta2.gt.ax0)then !scale back to [0,1]*ax0
              deltheta2 = deltheta2 - ax0
          elseif(deltheta2.lt.xmin)then
               deltheta2 = deltheta2 + ax0
          endif
c           write(6,*) deltheta/ax0, deltheta2/ax0
c           pause
          if(deltheta2.lt.xleft)then
              V2 = height/Lleft * (deltheta2-xmin)
              dV2 =height/Lleft
          else
              V2 = height - height/Lright * (deltheta2 - xleft )
              dV2 = -height/Lright
          endif
          if(deltheta2.gt.(xleft-lbump) .and.
     &         deltheta2.le.xleft)then
              V2 = V2 + vbump/lbump *(deltheta2-xleft+lbump)
              dV2 = dV2 + vbump/lbump
          elseif(deltheta2.gt.xleft .and.
     &         deltheta2.le.(xleft+lbump)) then
              V2 = V2 + vbump/lbump * (xleft-deltheta2) + vbump
              dV2 = dV2 - vbump/lbump
          endif
ccccccccccccccccccccccccccccccc
c here the rate constants are calculated
ccccccccccccccccccccccccccccccccccccccccccc
              krate12 = 0.d0
              if(deltheta2.ge.xr3 .and. deltheta2.lt.xr4)
     &          then
                Kscalef=kfac2 - (kfac2-kfac1)/(xr4-xr3)
     &              * (deltheta2-xr3)
```

```
c                 Kscalef = 1.d0
                  krate12 = k12p *Kscalef
     &                 * dexp(0.5*(V1-V2+pmf)/kBT)
                elseif(deltheta2.ge.xr2 .and. deltheta2.lt.xr3)
     &            then
                  Kscalef=kfac1 + (kfac2-kfac1)/(xr3-xr2)
     &                 * (deltheta2-xr2)
c                  %Kscalef=1.d0
                  krate12 = k12p *Kscalef
     &                 * dexp(0.5*(V1-V2+pmf)/kBT)
                elseif(deltheta.ge.xr3 .and. deltheta.lt.xr4)
     &            then
                  Kscalef=kfac2-(kfac2-kfac1)/(xr4-xr3)
     &                 * (deltheta-xr3)
c                  %Kscalef = 1.d0
                  krate12 = k12c *Kscalef
     &                 * dexp(0.5*(V1-V2-pmf)/kBT)
                elseif(deltheta.ge.xr2 .and. deltheta.lt.xr3)
     &            then
                  Kscalef= kfac1 + (kfac2-kfac1)/(xr3-xr2)
     &                 * (deltheta-xr2)
c                  %Kscalef = 1.d0
                  krate12 = k12c *Kscalef
     &                 * dexp(0.5*(V1-V2-pmf)/kBT)
                endif
c
                krate21 = 0.d0
                if(deltheta2.ge.xr3 .and. deltheta2.lt.xr4)
     &            then
                   Kscalef=kfac2 - (kfac2-kfac1)/(xr4-xr3)
     &                  *(deltheta2-xr3)
c                   Kscalef = 1.d0
                  krate21 = k21 *Kscalef
     &                 * dexp(-0.5*(V1-V2+pmf)/kBT)
                elseif(deltheta2.ge.xr2 .and. deltheta2.lt.xr3)
     &            then
                  Kscalef= kfac1 + (kfac2-kfac1)/(xr3-xr2)
     &                 * (deltheta2-xr2)
c                   Kscalef = 1.d0
                  krate21 = k21 *Kscalef
     &                 * dexp(-0.5*(V1-V2+pmf)/kBT)
                elseif(deltheta.ge.xr3 .and.
     &              deltheta.lt.xr4) then
                   Kscalef=kfac2-(kfac2-kfac1)/(xr4-xr3)
     &                 * (deltheta-xr3)
c                   Kscalef = 1.d0
                  krate21 = k21 *Kscalef
     &                 * dexp(-0.5*(V1-V2-pmf)/kBT)
                elseif(deltheta.ge.xr2 .and.
     &              deltheta.lt.xr3) then
```

```
                Kscalef= kfac1 + (kfac2-kfac1)/(xr3-xr2)
     &                  * (deltheta-xr2)
c                 Kscalef = 1.d0
                krate21 = k21 *Kscalef
     &                  * dexp(-0.5*(V1-V2-pmf)/kBT)
              endif
CCCCCCC
          maxkrate = max(krate12,krate21)
          if(maxkrate.gt.5.0e5)then
            krate12 = krate12*5.0e5/maxkrate
            krate21 = krate21*5.0e5/maxkrate
          endif
          if(sc(j).eq.1)then !currently empty
              dV = dv1
              krate(j) = krate12
          else  !currently occupied
              dv = dv2
              krate(j) = krate21
          endif
ccccccccccccccccccccccccccccccccccccccccccccccccccccccccC
          dF(j) = dF(j) - kappa(1)*(thetaS-thetaS0(j)) + dV
          dF(nstator+1) = dF(nstator+1) - dV
        Enddo
        torLR = kappa(2)*(x(nstator+1)-x(nstator+2))
        dF(nstator+1) = dF(nstator+1) - torLR
        dF(nstator+2) = dF(nstator+2) + torLR
ccccccccccccccccccccccccccccccccccccccccccccccc
        if(debug .eq.1)then
          write(10,*)x(nstator+1)/ax0, V1,V2
          write(11,*)x(nstator+1)/ax0,krate(1),pmf
        endif
c%%%%%%%%%%%%%%%%%%%%%%%%%%%
c update chemical states
        Do j=1,nstator
          sumrate = 0.d0
          R(1) = 0.d0
          randnum = ran1(idum)
          do i = 1,maxnts
            sumrate = sumrate + dt*krate((j-1)*maxnts+i)
            R(i+1) = sumrate
c             if(R(i+1).gt.1) then
c               write(*,*)'too big dt'
c               stop
c             endif
            if(randnum.gt.R(i) .and. randnum .le.R(i+1)) then
              sc(j) = mod(sc(j),2)+1
              tdelay(j) = t
              goto 99
            endif
          enddo
```

```
 99       enddo
c  update trajectories
         t = t + dt
         xold = x(nstator+2)
         do i=1+nstator,2+nstator
c first generate a random number from a normal gaussian distribution
           randnum1 = ran1(idum)
           randnum2 = ran1(idum)
           randnum = dsqrt(-2.d0*dlog(randnum1))
     &           *dcos(2.d0*onepi*randnum2)
           x(i) = x(i) + DTt(i) * dF(i) + sqDt(i) * randnum
         enddo
         if(istep.eq.neq0)then
           xi = x(nstator+2)
           ti = t
         endif
         if(istep.gt.neq0 .and. (xold-xi).lt.xsamp .and.
     &          (x(nstator+2)-xi).ge.xsamp)then
           write(11,55)t-ti,x(nstator+2)-xi
           xsamp = xsamp + 0.5*onepi
         endif
 55       format(2x,4e15.7)
         if(mod(istep-neq0,nsamp).eq.0 .and. istep.gt.neq0)then
           Do i = 1,nfree
             xt(i,icount) = x(i)
           Enddo
           Do i = 1,nstator
             sct(i,icount) = sc(i)
           Enddo
           tsave(icount) = t
           write(2,900)tsave(icount),xt(1,icount),
     &           xt(nstator+1,icount),xt(nstator+2,icount)
c           write(2,*)istep,icount,nstep/nsamp
           icount = icount + 1
          Endif
c          if(ipoint .eq.1 .and. itraj .eq.1 .and.istep.gt.neq0
c     &        .and.istep.lt.1e7  .and. mod(istep-neq0,100).eq.0 )then
c            write(10,900)t,x(1),x(nstator+1),x(nstator+2)
c          endif
 100   continue
 900   format(2x,4e15.6)
       write(2,*)
       write(11,*)
c      call flush(2)
       if(debug.eq.1)then
         stop
       endif
ccccccccccccccccc
       omega(itraj,ipoint) =
     &     (xt(nstator+1,nstep/nsamp)
```

```
    &      -xt(nstator+1,1))/(tsave(nstep/nsamp)
    &      -tsave(1))/2.d0/onepi
      write(1,*)omega(itraj,ipoint)
c       write(1,*)xt(3,nstep/nsamp),xt(3,1)
c        close(10)
c       close(11)
 200   continue
      write(1,*)
      write(11,*)
      aveomega(1,ipoint) = 0.d0
      do itraj=1,ntraj
         aveomega(1,ipoint) = aveomega(1,ipoint)
    &          + omega(itraj,ipoint)
      enddo
      aveomega(1,ipoint) = aveomega(1,ipoint)/ntraj
      aveomega(2,ipoint) = 0.d0
      do itraj=1,ntraj
         aveomega(2,ipoint) = aveomega(2,ipoint)
    &       + (omega(itraj,ipoint)-aveomega(1,ipoint))**2
      enddo
      aveomega(2,ipoint) = dsqrt(aveomega(2,ipoint)/(ntraj-1.d0))
      torque(ipoint) = aveomega(1,ipoint) * 2.d0*onepi
    &         *(1.d0/Dcnst(nstator+2)+1.d0/Dcnst(nstator+1))*kBT
 300   continue
      write(1,*)
      Do i = 1,npoint
         write(1,*)aveomega(1,i),aveomega(2,i),torque(i)
      enddo
      close(1)
      close(2)
      close(11)
c      elapsedtime = etime(telaps)
C       WRITE(*,*) elapsedtime
      end
c%%%%%%%%%%%%%%%%%%%%%%%%%%%%%%%%%%%%%%%%%
%%%%%%%%%%%%%%%%%%%%%%%%%%%%%%%%%%%%%%%%%
%%%%
c%%%%%%%%%%%%%%%%%%%%%%%%%%%%%%%%%%%%%%%%%
%%%%%%%%%%%%%%%%%%%%%%%%%%%%%%%%%%%%%%%%%
%%%%%
c---------------------------------------------------------*
c
c Random number generator from Numerical Recipes (p. 197).
c ran1 is used due to its simplicity and speed; however,
c its ability is to be checked.
c
     FUNCTION ran1(idum)
     INTEGER idum,IA,IM,IQ,IR,NTAB,NDIV
     REAL ran1,AM,EPS,RNMX
     PARAMETER (IA=16807,IM=2147483647,AM=1./IM,IQ=127773,IR=2836,
```

```
     & NTAB=32,NDIV=1+(IM-1)/NTAB,EPS=1.2e-7,RNMX=1.-EPS)
      INTEGER j,k,iv(NTAB),iy
      SAVE iv,iy
      DATA iv /NTAB*0/, iy /0/
      if (idum.le.0.or.iy.eq.0) then
        idum=max(-idum,1)
        do 11 j=NTAB+8,1,-1
          k=idum/IQ
          idum=IA*(idum-k*IQ)-IR*k
          if (idum.lt.0) idum=idum+IM
          if (j.le.NTAB) iv(j)=idum
11      continue
        iy=iv(1)
      endif
      k=idum/IQ
      idum=IA*(idum-k*IQ)-IR*k
      if (idum.lt.0) idum=idum+IM
      j=1+iy/NDIV
      iy=iv(j)
      iv(j)=idum
      ran1=min(AM*iy,RNMX)
      return
      END
c-----------------------------------------------------------------*
```

REFERENCES

[1] Oster, G. Darwin's motors. *Nature* 417, 25 (2002).

[2] Mogilner, A., Elston, T., Wang, H. and Oster, G. Molecular motors: theory. In *Computational Cell Biology*, C. Fall, E. Marland, J. Tyson, and J. Wagner, Eds. (Springer, NY, 2002).

Mogilner, A., Elston, T., Wang, H. and Oster, G. Molecular motors: examples. In *Computational Cell Biology*, C. Fall, E. Marland, J. Tyson and J. Wagner, Eds. (Springer, NY, 2002).

[3] Howard, J. Mechanics of Motor Proteins and the Cytoskeleton. (Sinauer Associates, Sunderland, MA, 2001)

[4] Rayment, I. *et al.* Three-dimensional structure of myosin subfragment-1: a molecular motor. *Science* 261, 50–58 (1993).

[5] Dominguez, R., Freyzon, Y., Trybus, K. M. and Cohen, C. Crystal structure of a vertebrate smooth muscle myosin motor domain and its complex with the essential light chain: visualisation of the pre-power stroke state. *Cell* 94, 559–571 (1998).

[6] Huxley, H. E., Stewart, A., Sosa, H. and Irving, T. X-ray diffraction measurements of the extensibility of actin and myosin filaments in contracting muscle. *Biophys. J.* 67, 2411–2421 (1994).

[7] Mehta, A.D., Rock, R.S., Rief, M., Spudich, J.A., Mooseker, M.S. and Cheney, R.E. Myosin-V is a processive actin-based motor. *Nature* 400, 590-593 (1999).

[8] Wells, A.L. *et al.* Myosin VI is an actin-based motor that moves backwards. *Nature* 401, 505-508 (1999).

[9] Alberts, B. *et al.* Essential cell biology. (Garland Sciences, Taylor & Francis Group, 2nd edition, 2003).

[10] Finer, J. T., Simmons, R. M. and Spudich, J. A. Single myosin molecule mechanics: piconewton forces and nanometre steps. *Nature* 368, 113–119 (1994).

[11] Molloy, J. E. *et al.* Movement and force produced by a singlemyosin head. *Nature* 378, 209–212 (1995).

[12] Kitamura, K., Tokunaga, M., Iwane, A. H. and Yanagida, T. A single myosin head moves along an actin filament with regular steps of 5.3 nanometres. *Nature* 397, 129–134 (1999).

[13] Piazzesi, G. *et al.* Mechanism of force generation by myosin heads in skeletal muscle. *Nature* 415, 659–662 (2002).

[14] Howard, J. Molecular motors: structural adaptations to cellular functions. *Nature* 389, 561-567 (1997).

[15] Svoboda, K., Schmidt, C. F., Schnapp, B. J. and Block, S. M. Direct observation of kinesin stepping by optical trapping interferometry. *Nature* 365, 721-727 (1993).

[16] Schnitzer, M. J. and Block, S. M. Kinesin hydrolyses one ATP per 8-nm step. *Nature* 388, 386-390 (1997).

[17] Visscher, K., Schnitzer, M.J. and Block, S.M. Single kinesin molecules studied with a molecular force clamp. *Nature* 400, 184-189 (1999).

[18] Yildiz, A. Tomishige, M., Vale, D.R. and Selvin, P.R. Kinesin walks hand-over-hand. *Science* 303, 676-678 (2004).

[19] Van den heuvel, M.G.L. and Dekker, C. Motor proteins at work for

nanotechnology. *Science* 317, 333-336 (2007).

[20] Gibbons, I.R. Cilia and flagella of eukaryotes. *J. Cell. Biol* 91, 107-124 (1981).

[21] Di Bella, L.M. and King, S.M. Dynein motors of the *Chlamydomonas* flagellum. *Int. Rev. Cytol.* 210, 227-268 (2001).

[22] Hirokawa, N. Kinesin and dynein superfamily proteins and the mechanism of organelle transport. *Science* 279, 519-526 (1998).

[23] Vale, R.D. The molecular motor toolbox for intracellular transport. *Cell* 112, 467-480 (2003).

[24] King, S. M. The dynein microtubule motor. *Biochim. Biophys. Acta* 1496, 60–75 (2000).

[25] Goodenough, U.W. and Heuser, J. Structural comparison of purified dynein proteins with *in situ* dynein arms. *J. Mol. Biol.* 180, 1083–1118 (1984).

[26] Asai, D. J. and Koonce, M. P. The dynein heavy chain: structure, mechanics and evolution. *Trends. Cell. Biol.* 11, 196–202 (2001).

[27] Burgess, S.A., Walker, M.L., Sakakibara, H., Knight, P.J. and Oiwa, K. Dynein structure and power stroke. *Nature* 421, 715-718 (2003).

[28] Oiwa, K. and Sakakibara, H. Recent progress in dynein structure and mechanism. *Curr. Opin. Cell. Biol.* 17, 98-103 (2005).

[29] Yasuda, R., Noji, H., Kinosita, K. Jr. and Yoshida, M. F_1-ATPase is a highly efficient molecular motor that rotates with discrete 120° steps. *Cell* 93, 1117-1124 (1998).

[30] Yasuda, R., Noji, H., Yoshida, M., Kinosita, K.Jr. and Itoh, H. Resolution of distinct rotational substeps by submillisecond kinetic analysis of F_1-ATPase. *Nature* 410, 898-904 (2001).

[31] Elston, T., Wang, H. and Oster, G. Energy transduction in ATP synthase.

Nature 391, 510-514 (1998).

[32] Wang, H. and Oster, G. Energy transduction in the F_1 motor of ATP synthase. *Nature* 396, 279-282 (1998).

[33] Xing, J., Liao, J. and Oster, G. Making ATP. *Proc. Natl. Acad. Sci. USA* 102, 16539-16546 (2005).

[34] Soong, R.K. *et al.* Powering an inorganic nanodevice with a biomolecular motor. *Science* 290, 1555-1558 (2000).

[35] Pedersen, P., Ko, Y.H. and Hong, S. ATP synthases in the year 2000: defining the different levels of mechanism and getting a grip on each. *J. Bioenerg. Biomembr.* 32, 325-332 (2000).

[36] Boyer, P.D. ATP synthase—past and future. *Biochim. Biophys. Acta* 1365, 3-9 (1998).

[37] Boyer, P.D. A research journey with ATP synthase. *J. Biol. Chem.* 277, 39045-39061 (2002).

[38] Francis, N.R., Sosinsky, G.E., Thomas, D.R. and DeRosier, D. J. Isolation, characterization and structure of bacterial flagellar motors containing the switch complex. *J. Mol. Biol.* 235, 1261-1270 (1994).

[39] Thomas, D.R., Morgan, D.G. and DeRosier, D.J. Rotational symmetry of the C ring and a mechanism for the flagellar rotary motor. *Proc. Natl. Acad. Sci. USA* 96, 10134-10139 (1999).

[40] Berg, H.C. The rotary motor of bacterial flagella. *Annu. Rev. Biochem.* 72, 19-54 (2003).

[41] Berg, H.C. Constraints on models for the flagellar rotary motor. *Phil.Trans.R.Soc.Lond. B* 355, 491-501 (2000).

[42] Blair, D.F. Flagellar movement driven by proton translocation. *FEBS. Letters.*

545, 86-95 (2003).

[43] Samatey, F. A. *et al.* Structure of the bacterial flagellar protofilament and implications for a switch for supercoiling. *Nature* 410, 331–337 (2001).

[44] Samatey, F.A. *et al.* Structure of the bacterial flagellar hook and implication for the molecular universal joint mechanism. *Nature* 431, 1062-1068 (2004).

[45] Khan, S., Dapice, M. and Reese, T.S. Effects of mot gene expression on the structure of the flagellar motor. *J. Mol. Biol.* 202, 575–84 (1988).

[46] Braun, T.F., Al-Mawsawi, L.Q., Kojima, S. and Blair, D.F. Arrangement of core membrane segments in the MotA/MotB proton-channel complex of *Escherichia coli*. *Biochemistry* 43, 35-45 (2004).

[47] Zhou, J., Fazzio, R.T. and Blair, D.F. Membrane topology of the MotA protein of *Escherichia coli*. *J.Mol. Biol.* 251, 237–42 (1995).

[48] Zhou, J., Lloyd, S.A. and Blair, D.F. Electrostatic interactions between rotor and stator in the bacterial flagellar motor. *Proc. Natl. Acad. Sci. USA.* 95, 6436-6441 (1998).

[49] Lo, C., Leake, M.C., Pilizota, T. and Berry, R.M. Nonequivalence of membrane voltage and ion gradient as driving forces for the bacterial flagellar motor at low load. *Biophys. J.* 93, 294–302 (2007).

[50] Ryu, W.S., Berry, R.M. and Berg, H.C. Torque-generating units of the flagellar motor of *Escherichia coli* have a high duty ratio. *Nature* 403, 444–447 (2000).

[51] Berry, R.M. and Berg, H.C. Torque generated by the flagellar motor of *Escherichia coli* while driven backward. *Biophys. J.* 76, 580–587 (1999).

[52] Chen, X. and Berg, H.C. Torque-speed relationship of the flagellar rotary motor of *Escherichia coli*. *Biophys. J.* 78, 1036–1041 (2000).

[53] Sowa, Y., Hotta, H., Homma, M. and Ishijima, A. Torque-speed relationship of the Na^+- driven flagellar motor of *Vibrio alginolyticus*. *J. Mol. Biol.* 327, 1043-1051 (2003).

[54] Gabel, C.V. and Berg, H.C. The speed of the flagellar rotary motor of *Escherichia coli* varies linearly with proton-motive force. *Proc. Natl. Acad. Sci. USA.* 100, 8748-8751 (2003).

[55] Samuel, A.D.T. and Berg, H.C. Fluctuation analysis of rotational speeds of the bacterial flagellar motor. *Proc. Natl. Acad. Sci. USA.* 92, 3502-3506 (1995).

[56] Samuel, A.D.T. and Berg, H.C. Torque generating units of the bacterial flagellar motor step independently. *Biophys. J.* 71, 918-923 (1996).

[57] Reid, S., Leake, M.C., Chandler, J.H., Lo, C. Armitage, J.P. and Berry, R.M. The maximum number of torque-generating units in the flagellar motor of *Escherichia coli* is at least 11. *Proc. Natl. Acad. Sci. USA.* 103, 8066-8071 (2006).

[58] Sowa, Y., Rowe, A.D., Leake, M.C., Yakushi, T., Homma, M., Ishijima, A. and Berry, R.M. Direct observation of steps in rotation of the bacterial flagellar motor. *Nature* 437, 916-919 (2005).

[59] Ashkin, A. History of optical trapping and manipulation of small-neutral particles, atoms, and molecules. *IEEE J. Sel. Top. Quantum Electron.* 6, 841-856 (2000).

[60] Chu, S., Bjorkholm, J.E., Ashikin, A. and Calbe, A. Experimental observation of optically trapped atoms. *Phys. Rev. Lett.* 57, 314-317 (1986).

[61] Ashkin, A. and Dziedzic, J.M. Optical trapping and manipulation of viruses and bacteria. *Science* 235, 1517-1520 (1987).

[62] Svoboda, K. and Block, S.M. Biological applications of optical forces. *Annu. Rev. Biophys. Biomol. Struct*. 23, 247-285 (1994).

[63] Pilizota, T., Bilyard, T., Bai, F., Futai, M., Hosokawa, H. and Berry, R.M. A programmable optical angle clamp for rotary molecular motors. *Biophys. J.* 93, 264-275 (2007).

[64] Bustamante, C., Keller, D. and Oster, G. The physics of molecular motors. *Acc. Chem. Res.* 34, 412-420 (2001).

[65] Xing, J., Wang, H. and Oster, G. From continuum Fokker-Planck models to discrete kinetic models. *Biophys. J.* 89, 1551-1563 (2005).

[66] Karplus, M. and McCammon, J. Molecular dynamics simulations of biomolecules. *Nat. Struct. Biol.* 9, 646-652 (2002).

[67] Bockmann, R. Nanoseconds molecular dynamics simulation of primary mechanical energy transfer steps in F_1-ATP synthatse. *Nat. Struct. Biol.* 9, 198-202 (2002).

[68] Aksimentiev, A., Balabin, I.A., Fillingame, R.H. and Schulten, K. Insights into the molecular mechanism of rotation in the F_0 sector of ATP synthase. *Biophys. J.* 86, 1332-1344 (2004).

[69] Truhlar, D.G. and Garrett, B.C. Variational transition-state theory. *Annu. Rev. Phys. Chem.* 35, 159-189 (1984).

[70] Jülicher, F. Ajdari, A. and Prost, J. Modeling molecular motors. *Rev. Mod. Phys.* 69, 1269-1282 (1997).

[71] Risken, H. in *The Fooker-Planck equation: methods of solutions and applications*. (Springer, New York, 1996).

[72] Elston, T.C. Models of post-translational protein translocation. *Biophys. J.* 79, 2235-2251 (2000).

[73] Elston, T. C. A macroscopic description of biomolecular transport. *J. Math. Biol.* 41, 189-206 (2000).

[74] Xing, J. Nonequilibrium dynamic mechanism for allosteric effect. *Phys. Rev. Lett.* 99, 168103 (2007).

[75] Fung, D.C. and Berg, H.C. Powering the flagellar motor of *Escherichia coli* with an external voltage source. *Nature* 375, 809-812 (1995).

[76] Berry, R.M. Theories of rotary motors. *Philos. Trans. R. Soc. Lond. B. Biol. Sci.* 355, 503-509 (2000).

[77] Block, S.M., Blair, D.F. and Berg, H.C. Compliance of bacterial flagella measured with optical tweezers. *Nature* 338, 514-518. (1989).

[78] Meister, M. Lowe, G. and Berg, H.C. The proton flux through the bacterial flagellar motor. *Cell* 49, 643-650 (1987).

[79] Blair, D.F. and Berg, H.C. Restoration of torque in defective flagellar motors. *Science* 242, 1678-1681 (1988).

[80] Lloyd, S.A., Whitby, F.G., Blair, D.F. and Hill, C.P. Structure of the c-terminal domain of flig, a component of the rotor in the bacterial flagellar motor. *Nature* 400, 472-475 (1999).

[81] Brown, P.N., Hill, C.P. and Blair, D.F. Crystal structure of the middle and c-terminal domains of the flagellar rotor protein flig. *EMBO J.* 21, 3225-3234 (2002).

[82] Kojima, S. and Bliar, D.F. Conformational change in the stator of the bacterial flagellar motor. *Biochemistry* 40, 13041-13050 (2001).

[83] Elston, T., You, D. and Peskin, C. Protein flexibility and the correlation ratchet. *SIAM J. Appl. Math.* 61**,** 776–791 (2000).

[84] Elston, T. and Peskin, C. The role of protein flexibility in molecular motor function: coupled diffusion in a tilted periodic potential. *SIAM J. Appl. Math.* 60**,** 842–867 (2000).

[85] Noji, H., Yasuda, R., Yoshida, M. and Kinosita, K. Direct observation of the

rotation of F_1-ATPase. *Nature* 386**,** 299–302 (1997).

[86] Miyata, M., Ryu, W.S. and Berg, H.C. Force and velocity of mycoplasma mobile gliding. *J. Bacteriol.* 184**,** 1827–1831 (2002).

[87] Inoue, Y. *et al.* Torque-speed relationship of Na^+ driven chimeric flagellar motors in *Escherichia coli*. *J. Mol. Biol.* 376, 1251-1259 (2008).

[88] Kerssemakers, J. W. J., Munteanu, E. L., Laan, L., Noetzel, T.L., Janson, M.E. and Dogterom, M. Assembly dynamics of microtubules at molecular resolution. *Nature* 442, 709-712 (2006).

[89] Berg, H.C. in *E. coli in Motion* (eds Greenbaum E.) 77-87, 97-102 (Springer-Verlag Press, New York, 2003).

[90] Sourjik, V. and Berg, H.C. Functional interactions between receptors in bacterial chemotaxis. *Nature* 428, 437-441 (2004).

[91] Cluzel, P., Surette, M. and Leibler, S. An ultrasensitive bacterial motor revealed by monitoring signalling proteins in single cells. *Science* 287, 1652-1655 (2000).

[92] Sourjik, V. and Berg, H.C. Binding of the *Escherichia coli* response regulator CheY to its target measured in vivo by fluorescence resonance energy transfer. *Proc.Natl. Acad. Sci. USA* 99, 12669-12674 (2002).

[93] Sagi, Y., Khan, S. and Eisenbach, M. Binding of the chemotaxis response regulator CheY to the isolated, intact switch complex of the bacterial flagellar motor: Lake of cooperativity. *J.Biol.Chem.* 278, 25867-25871 (2003).

[94] Duke, T.A.J., Le Novère, N. and Bray, D. Conformational spread in a ring of proteins: A stochastic approach to allostery. *J. Mol.Biol.* 308, 541-553 (2001).

[95] Bren,A. and Eisnebach, M. The N terminus of the flagellar switch protein, FliM, is the binding domain for the chemotactic response regulator, CheY. *J.Mol.Biol.* 278,507-514 (1998).

[96] Toker, A.S. and Macnab, R.M. Distinct regions of bacterial flagellar switch protein FliM interact with FliG, FliN and CheY. *J. Mol.Biol.* 273, 623-634 (1997).

[97] Garza, A.G., Biran, R. Wohlschlegel, J.A. and Manson, M.D. Mutations in *motB* suppressible by changes in stator or rotor components of the bacterial flagellar motor. *J. Mol.Biol.* 258,270-285 (1996).

[98] Van Way, S.M., Millas, S.G., Lee, A.H. and Manson, M.D. Rusty, jammed, and well-oiled hinges: mutations affecting the interdomain region of FliG, a rotor element of the *Escherichia coli Flagellar* Motor. *J. Bacteriol.* 186, 3173-3181 (2004).

[99] Xing, J., Bai, F., Berry, R.M. and Oster, G. Torque-speed relationship of the bacterial flagellar motor. *Proc.Natl.Acad.Sci.USA.* 103, 1260-1265 (2006).

[100] Korobkova, E., Emonet, T., Vilar, J.M., Shimizu, T.S. and Cluzel, P. From molecular noise to behavioural variability in a single bacterium. *Nature* 428, 574-578 (2004).

[101] Lapidus, I.R., Welch, M. and Eisenbach, M. Pausing of flagellar rotation is a component of bacterial motility and chemotaxis. *J. Bacteriol.* 170, 3627-3632 (1988).

[102] Eisenbach, M. *et al.* Pausing, switching and speed fluctuation of the bacterial flagellar motor and their relation to motility and chemotaxis. *J.Mol.Biol*. 211, 551-563 (1990).

[103] Kudo, S., Magariyama, Y. and Aizawa, S.I. Abrupt changes in flagellar rotation observed by laser dark-field microscopy. *Nature* 346, 677-680 (1990).

[104] Leake, M.C., Chandler, J.H., Wadhams, G.H., Bai, F., Berry, R.M. and Armitage, J.P. Stoichiometry and turnover in single, functioning membrane protein complexes. *Nature* 443, 355-358 (2006).

[105] Stefanie, Y. *et al.* Diffusion of lipid-like single-molecule fluorophores in the cell membrane. *J. Phys. Chem.B* 110, 8151-8157 (2006).

[106] Saxton, M.J. Single-particle tracking: the distribution of diffusion coefficients. *Biophys. J.* 72, 1744-1753 (1997).

[107] Mullineaux, C.W., Nenninger, A., Ray, N. and Robinson, C. Diffusion of green fluorescent protein in three cell environments in *Escherichia coli*. *J. Bacteriol.* 188, 3442-3448 (2006).

[108] Jin, S., Haggie, P.M. and Verkman, A.S. Single-particle tracking of membrane protein diffusion in a potential: simulation, detection, and application to confined diffusion of CFTR $C1^-$ channels. *Biophys. J.* 93, 1079-1088 (2007).